CWP-464
October 2003

Migration velocity analysis in factorized VTI media

Debashish Sarkar

— Doctoral Thesis —
Geophysics

Defended October, 2003

Committee Chair:	Prof. Robert Siegrist
Advisor:	Prof. Ilya Tsvankin
Committee members:	Prof. Max Peeters
	Prof. Junping Wang
	Prof. Ken Larner

Center for Wave Phenomena
Colorado School of Mines
Golden, Colorado 80401
(1) 303 273-3557

This thesis is dedicated to my parents
Dr. Bijit K. Sarkar and Mitali Sarkar

Abstract

To obtain a good image and accurate depth positioning of reflectors in the subsurface, it is essential to account for heterogeneity and velocity anisotropy. Existing anisotropic velocity-analysis algorithms often approximate the subsurface with homogeneous or vertically heterogeneous anisotropic layers or blocks, which is suitable in time imaging. For depth imaging purposes, however, lateral heterogeneity should also be accounted for. So the main challenge is in describing lateral and vertical heterogeneity and anisotropy simultaneously.

The simplest realistic heterogeneous anisotropic model is the factorized VTI (transversely isotropic with a vertical symmetry axis) medium with constant vertical and lateral gradients in vertical velocity. I determine what parameters can be estimated uniquely in such media from surface seismic data, and use this information to develop a robust parameter estimation algorithm. By approximating the subsurface with piecewise factorized VTI blocks or layers I build a spatially varying anisotropic velocity field for depth imaging.

The parameter estimation algorithm is implemented in the post-migrated domain as a two-step iterative procedure that includes prestack depth migration (imaging step) followed by an update of the medium parameters (velocity-analysis step). The residual moveout of the migrated events, which is minimized during the parameter updates, is described by a nonhyperbolic equation whose coefficients are determined by 2-D semblance scanning.

For piecewise-factorized VTI media without significant dips in the overburden, the residual moveout of P-wave events in image gathers is governed by four effective quantities in each block: (1) the normal-moveout (NMO) velocity $V_{\rm nmo}$ at a certain point within the block, (2) the vertical velocity gradient k_z, (3) the combination $\hat{k}_x = k_x\sqrt{1+2\delta}$ of the lateral velocity gradient k_x and the anisotropic parameter δ, and (4) the anellipticity parameter η. I show that all four parameters can be estimated from the residual moveout for at least two reflectors within a block sufficiently separated in depth. Although the vertical velocity gradient is uniquely constrained by the moveout of events, the lateral gradient is always coupled to the anisotropic parameter δ. To decouple the lateral gradient from the anisotropy and build an accurate model in depth, *a priori* information (e.g., the vertical velocity at a single point) is required.

Application of my algorithm to two field lines from West Africa confirms the presence of anisotropy and lateral heterogeneity in the subsurface and results in much better images than those previously obtained with time domain techniques. Most events in image gathers after prestack depth migration are flat, and the estimated time-depth curve closely matches the one obtained from borehole data. This implies that the piecewise factorized model is a suitable choice for imaging and velocity analysis in heterogeneous anisotropic media.

Acknowledgments

It has been a privilege to have done my PhD dissertation under the guidance of Prof. Ilya Tsvankin. Throughout the last two years he has encouraged me to pursue my ideas, corrected me when I strayed too far, been a storehouse of wisdom, and perhaps most importantly, he instilled in me the confidence that is so essential in doing independent research.

I have always believed that without the support of Ken Larner I may never have come to the Colorado School of Mines. Although my working relationship with him was confined only to a brief couple of months during my first year at Mines, I have learned much from the interactions I have had with him over the last four years and have benefited greatly from his advice.

Through the years I have had the good fortune of working closely with extremely knowledgeable people in academia and in the industry. John Castagna, as my MS adviser, influenced me greatly during my early days in graduate school; Andrey Bakulin provided me with the opportunity to work on physical modeling experiments and Bob Kranz made me aware of the different nuances of the experimental side of Geophysics while working on my second comprehensive project; at Conoco, Bob Baumel gave me the freedom to continue working on my MS thesis research, which made it possible to finish my first comprehensive project in time; from Bill Lamb I learned that mathematics is essential in understanding geophysical problems and simplicity is the key to its effective use; Mike Howard taught me prestack depth migration and migration velocity analysis, experience that was so valuable while working on this dissertation; and Phil Anno and Bob Corbin were wonderful and patient mentors during my first attempts at working with seismic data.

Many thanks to Andreas Rueger for encouraging me to pursue this research. I am grateful to Greg Ball for sharing with me time-depth curves for the offshore Africa data. My immense gratitude to Max Peeters, Junping Wang, and Robert Siegrist for serving on my committee. Financial support was provided by the consortium members of CWP, and the Chemical Sciences, Geosciences and Biosciences Division, Office of Basic Energy Sciences, U.S. Department of Energy. I am also grateful to Terry and Nadine Young for making my wife and me feel at home in a foreign land.

Graduate studies at the Colorado School of Mines would not have been enjoyable if I had not had such good friends and officemates like Matt Haney, XiaoXia Xu, Vinicio Sanchez, Rodrigo Fuck, David Stillman, Chris Robinson, Andrés Pech, Jyoti Behura, and Kurang Mehta. Barbara, Michelle, and Lela were always helpful, and without John Stockwell's help with all things computational, this thesis would never have been completed.

Finally, I am indebted to my wife Roshni, sister Debamitra, brother-in-law Rathin, and nephew Ramit for their unwavering support. When things went wrong, they cheered me on.

Table of Contents

Chapter 1

Introduction

1.1 Heterogeneity and anisotropy

Since the early days of the seismic method geophysicists have recognized that the subsurface is highly heterogeneous. Heterogeneity in rocks causes velocity of waves to depend on the spatial position, and is so prevalent that even the same rock type can exhibit a wide variation in velocity depending on the conditions under which the rock was formed, its depth of burial, mineral composition, porosity, and age (Birch, 1942, 1961). A simple visual inspection of well logs or core samples is sufficient to recognize the widespread presence of heterogeneity in the subsurface. To image and characterize the subsurface correctly, it is important to estimate the spatial velocity distribution, and techniques to do so have ranged from simple analytic functions (e.g., Faust, 1951, 1953; Gardner *et al.*, 1974) to sophisticated tomographic schemes (e.g., Stork, 1988; Liu, 1997; Meng, 1999; Chauris and Noble, 2001).

Most of these techniques, however, assume that rocks are isotropic, that is, that the velocity of waves in rocks does not depend on the direction of propagation. Since most rocks are anisotropic, this assumption is more often than not untrue (e.g., Banik, 1984; Thomsen, 1986; Alkhalifah, 1996; Tsvankin, 2001). Alignment of mineral grains, clay platelets, layering, fractures, and *in situ* stress all contribute to the observed anisotropy in the subsurface. Common problems caused by ignoring anisotropy in seismic imaging include mis-ties in time-to-depth conversion, failure to preserve dipping energy during dip-moveout (DMO) correction, and mispositioning of migrated dipping events (e.g., Banik, 1984; Alkhalifah *et al.*, 1996; Tsvankin, 2001). Jaramillo and Larner (1995) studied anisotropy-induced errors in prestack depth migration and showed that isotropic migration algorithms fail to flatten image gathers for a wide range of transversely isotropic (TI) models, which leads to poorly focused images.

Depending on the dominant wavelength of the seismic wave, a medium may appear heterogeneous or anisotropic (Backus, 1970; Helbig, 1984). Anisotropy is typically observed when the scale of the heterogeneity is much smaller than the dominant wavelength. As the dominant frequency increases and the wavelength becomes close to the scale of the heterogeneity, the same medium that appeared anisotropic at lower frequencies behaves as heterogeneous rather than anisotropic. For the purposes of this thesis it will be sufficient to attribute the measured anisotropy to the heterogeneity whose scale is much smaller than the seismic wavelength (e.g., that caused by the preferential orientation of mineral grains or clay platelets, and fine layering). Similarly, the measured heterogeneity may be attributed to heterogeneity whose scale is much larger than the seismic wavelength (e.g., that caused

by lithology variation, compaction, unconformities, and coarse layering).

Most existing velocity-analysis methods for anisotropic media approximate the subsurface with homogeneous layers or blocks (e.g., Alkhalifah and Tsvankin, 1995; Le Stunff and Jeannot, 1998; Tsvankin, 2001; Grechka *et al.*, 2002). Anisotropic layers, however, are often characterized by non-negligible velocity gradients that may distort the shape of underlying reflectors and cause errors in the estimates of the anisotropic parameters. Since lateral homogeneity is an inherent assumption in time imaging, whether isotropic or anisotropic, it is justified to ignore lateral gradients in the time-domain velocity analysis of P-waves in VTI media (e.g., Alkhalifah, 1997; Han *et al.*, 2000). In contrast, anisotropic *depth* imaging has to account properly for both vertical and lateral variations of the velocity field. An analytic correction of normal-moveout (NMO) ellipses for lateral velocity variation in anisotropic media was developed by Grechka and Tsvankin (1999). Their method, however, is limited to horizontal layers, small lateral velocity gradients, and the hyperbolic portion of reflection moveout. Also, for purposes of depth imaging, we are not interested in just removing the influence of lateral velocity variation on anisotropic inversion; rather, we need to estimate the lateral velocity variation accurately. As illustrated by Figure 1.1, a good image of this West Africa dataset can be obtained only if both heterogeneity and anisotropy are correctly accounted for in the imaging process.

The main problem in reconstructing a spatially varying anisotropic velocity field is caused by trade-offs between the velocity gradients, anisotropic parameters, and the shapes of the reflecting interfaces, which introduce nonuniqueness in velocity analysis of surface seismic data. Trade-offs between anisotropy and heterogeneity may cause heterogeneity to masquerade as anisotropy, and vice versa, which makes it extremely difficult to distinguish heterogeneity from anisotropy. For example, reflection traveltimes from a diffractor at a fixed spatial location in a vertically heterogeneous isotropic medium can be completely equivalent to the traveltimes from a diffractor placed in a homogeneous transversely isotropic medium with a vertical axis of symmetry (VTI). To resolve such ambiguities, *a priori* information may often be necessary. Trade-offs between the velocity field and reflector shapes also sometimes cannot be resolved without *a priori* information, even for isotropic media. A practical way to incorporate vertical and lateral velocity variations into anisotropic velocity analysis without excessively compromising the uniqueness of the solution is to adopt the so-called *factorized anisotropic model* in which the ratios of the stiffness coefficients (and, therefore, the anisotropic parameters) are constant.

By representing the subsurface with piecewise factorized blocks, where each block is bounded by plane or irregular interfaces, I attempt to estimate the anisotropy, heterogeneity (vertical and lateral), and reflector shapes simultaneously from surface seismic data. In doing so I outline a practical method to build anisotropic heterogeneous velocity models in depth. The estimated velocity field makes it possible to obtain high-quality depth-migrated images such as the one in Figure 1.1b.

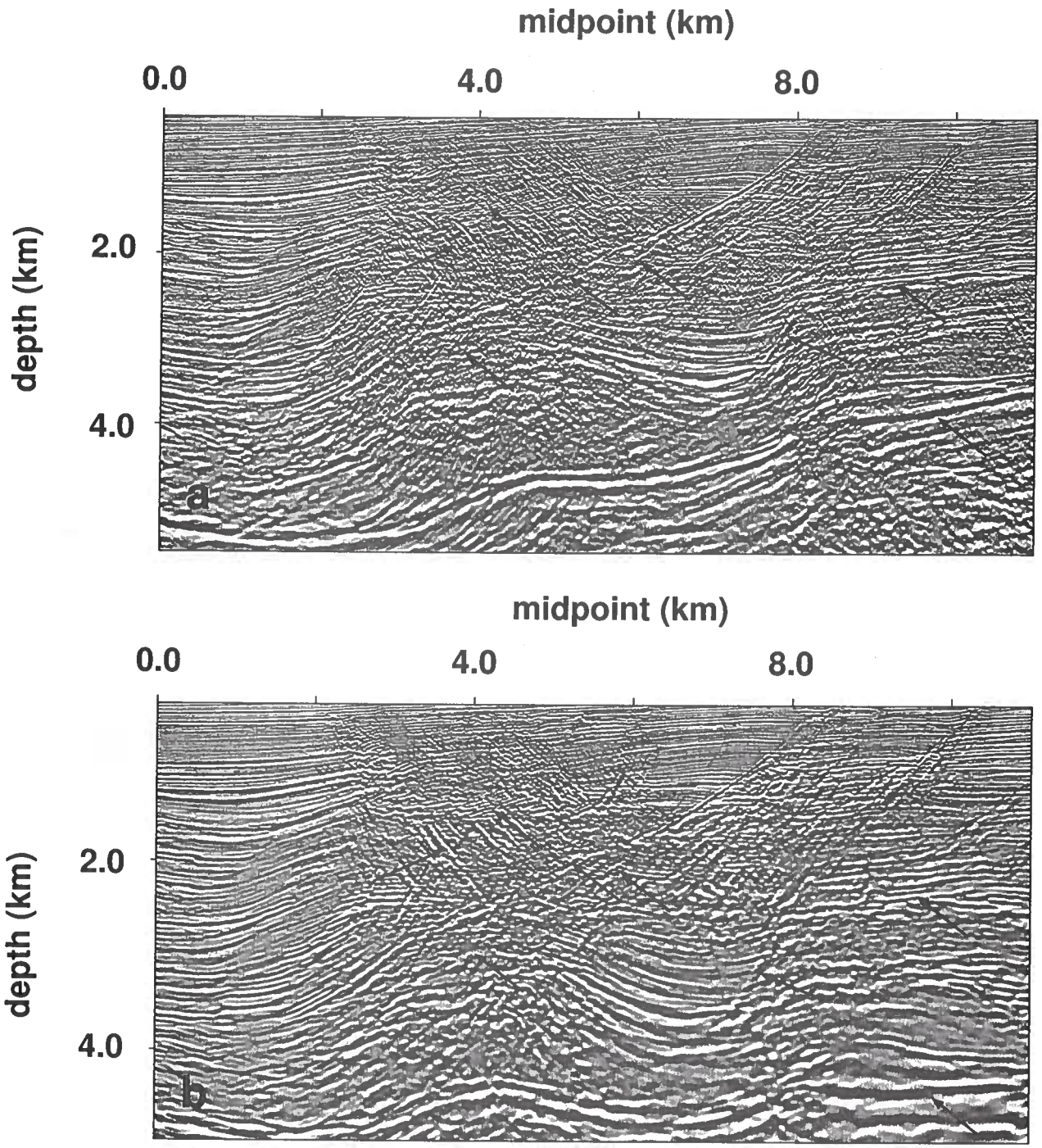

Figure 1.1. Stacked section of a West Africa dataset obtained after anisotropic (a) time migration (after Alkhalifah, 1996) and (b) prestack depth migration. Lateral variation in vertical velocity and anisotropic parameters were ignored in time migration, but were estimated and accounted for in prestack depth migration using the algorithm proposed in this thesis. The arrows mark few improvements that result after prestack depth migration.

1.2 Factorized VTI medium

The simplest and likely most common anisotropic symmetry for sedimentary rocks is transverse isotropy with a vertical symmetry axis (VTI). Transverse isotropy caused by horizontal alignment of mineral grains and clay platelets is typical for shales (Sayers, 1994). In clastic sequences, VTI may be caused by aligned horizontal microcracks and thin layering when the thickness of the layers is much smaller than the predominant seismic wavelength (Backus, 1970). Because of its widespread occurrence in sedimentary rocks, I shall study only the VTI medium in this thesis. The methodology discussed here, however, is also applicable to symmetry planes of media with lower symmetries.

A VTI medium is characterized by an *isotropy plane* and a *symmetry axis*, which coincide with the bedding plane and depth (vertical) axis, respectively. In such media, velocity of waves depends on just the angle with the symmetry axis. Here, I analyze P-wave data for VTI media. In contrast to the single scalar velocity responsible for isotropic P-wave traveltimes, the kinematic signatures of P-waves in VTI media are governed by three parameters: the vertical velocity V_{P0} and Thomsen's (1986) anisotropic coefficients ϵ and δ (Tsvankin and Thomsen, 1994; Tsvankin, 2001) defined as

$$V_{P0} \equiv \sqrt{\frac{C_{33}}{\rho}}, \tag{1.1}$$

$$\epsilon \equiv \frac{C_{11} - C_{33}}{2\,C_{33}}, \tag{1.2}$$

$$\delta \equiv \frac{(C_{13} + C_{55})^2 - (C_{33} - C_{55})^2}{2\,C_{33}\,(C_{33} - C_{55})}. \tag{1.3}$$

C_{ij} are elements of the 6x6 stiffness matrix that relates the stress tensor τ_{ij} to the strain tensor e_{ij}. ϵ, which is also the fractional difference between the horizontal and vertical velocities, governs wave propagation close to the isotropy plane, while δ, which is also the second derivative of the phase velocity evaluated at the symmetry axis, governs wave propagation close to the symmetry axis.

A medium is called factorized if all ratios of the stiffness elements C_{ij} are constant in space, which implies that the anisotropic coefficients and the ratio of the vertical velocities of P- and S-waves have to be constant as well (Červený, 1989). Despite its limitations, the factorized VTI model offers the simplest way to account for both heterogeneity and anisotropy in subsurface formations. For P-waves, heterogeneity in factorized media is described by the spatially varying vertical velocity V_{P0}, while anisotropy is controlled by the constant values of ϵ and δ. Although V_{P0}, ϵ, and δ in the subsurface may actually vary independently of each other, ϵ and δ are typically estimated with a relatively low spatial resolution and are believed to have slower spatial variation than does velocity. Therefore, a good approximation for realistic VTI velocity fields can often be achieved by dividing the model into factorized VTI blocks, with piecewise linear functions of V_{P0} and piecewise constant functions of ϵ and δ. I use this subset of factorized VTI models to build velocity fields in depth.

In factorized media the ratio of the vertical P- and S-wave velocities (V_{P0}/V_{S0}) is constant, and spatial variations of V_{S0} are directly tied to those of V_{P0}. Since P- and S-wave velocity gradients often differ in subsurface formations, the factorized model may seem to be too simplistic for practical applications. This issue, however, does not arise in the P-wave velocity analysis discussed here because P-wave kinematics is virtually independent of V_{S0} (Tsvankin and Thomsen, 1994; Alkhalifah, 2000; Tsvankin, 2001).

1.3 Image gathers and velocity analysis

Image gathers are offset-versus-depth gathers generated after prestack depth migration of seismic data. The moveout of events in image gathers describes how the migrated depth at a fixed midpoint location varies with the source-receiver offset. Migration with the correct velocity model causes the migrated depth to become independent of offset and the migrated events in image gathers are flat. If events are not flat, they are said to exhibit residual moveout, which can be a good diagnostic of errors in the velocity field. In isotropic media, if too high a velocity is used for migration, the events are undercorrected, while too low a velocity causes overcorrection. Because of their high sensitivity to the velocity field, the moveout of events in image gathers is often used to perform residual velocity analysis in isotropic media.

Since my goal is to estimate the relevant VTI parameters and carry out depth imaging for models with significant lateral and vertical velocity variation and considerable structural complexity, velocity model building is conveniently implemented in the prestack depth-migrated domain (e.g., Stork, 1992; Liu, 1997). Prestack depth-migrated data are also preferred for velocity analysis because of their higher signal-to-noise ratio compared with that of unmigrated data. To use the moveout of events in image gathers for parameter estimation in anisotropic media, it is first important to understand how different model parameters influence residual moveout in image gathers. A large part of this thesis is devoted to understanding this issue.

For 2-D wave propagation in the $[x, z]$ plane, the function $z(h)$ that defines the migrated depth of an event in an image gather is obtained by solving the following set of equations:

$$\begin{aligned} \tau_s(x_s, x, z) + \tau_r(x, z, x_r) &= t(y, h)\,, \\ \frac{\partial \tau_s}{\partial y} + \frac{\partial \tau_r}{\partial y} &= \frac{\partial t}{\partial y}\,, \end{aligned} \tag{1.4}$$

where y is the common midpoint, τ_s is the traveltime from the source at x_s to the diffraction point (x, z), τ_r is the traveltime from the receiver at x_r to the point (x, z), and $t(y, h)$ is the observed total traveltime, which depends on the true positions of the diffractor, the source, and the receiver for midpoint y and half-offset h. Generally, equation (1.4) does not lend itself to closed-form expressions, even for isotropic media (Liu, 1997). Moreover, analytic treatment of image gathers is much more involved in anisotropic media because of the velocity variation with propagation angle and the increased number of medium parameters.

Hence, most analytic solutions in this thesis are based on the weak-anisotropy approximation linearized with respect to the parameters ϵ and δ. The linearized equations,

which reveal the influence of the VTI parameters on events in image gathers, are verified by performing numerical tests for a representative set of VTI models.

1.4 Overview of each chapter

In **Chapter 2**, I analyze P-wave image gathers for transversely isotropic media with a vertical symmetry axis (VTI media). I study the residual moveout of events in image gathers in homogeneous and factorized $v(z)$ media caused by errors in the medium parameters, and establish the conditions needed to flatten and correctly position events in depth. Kinematic signatures of P-waves in factorized $v(z)$ media are defined by the vertical velocity V_{P0} at a point in the medium [taken at the surface ($z = 0$) here], the vertical-velocity gradient k_z, and the parameters ϵ and δ. A key result of this section is that the vertical gradient k_z can be uniquely estimated from surface seismic data alone.

In **Chapter 3**, I extend the study of the residual moveout of events in image gathers to factorized $v(x,z)$ media and establish the conditions needed to flatten and correctly position events in depth. Kinematics of P-waves in factorized $v(x,z)$ media are defined by the vertical velocity V_{P0} at a point on the surface (e.g., $x = 0, z = 0$), k_z, ϵ, δ, and the lateral-velocity gradient k_x. As in the factorized $v(z)$ medium, surface seismic data can be used to uniquely constrain the vertical gradient k_z, even in the presence of lateral heterogeneity. The lateral gradient k_x, however, cannot be separated from the anisotropic parameter δ without *apriori* information.

I develop a migration velocity analysis (MVA) algorithm for factorized VTI media in **Chapter 4**, and using synthetic tests for a single factorized layer, I assess the accuracy of the algorithm and its robustness in the presence of random noise.

In **Chapter 5**, I apply the MVA algorithm to more complicated multilayered models. I also study the influence of reflector structure and errors in vertical velocity on the estimated parameters.

As a final test of the algorithm, in **Chapter 6** I process two field lines from a 3-D survey acquired in offshore West Africa. The lines were recorded in a region that was shaped by major tectonic activity. The lithology in the shallow part of the section is represented by regressive sequences, shaly clastics, high pressure shales and turbidites. The deeper part of the section consists of transgressive sequences, marine clastics, and non-marine red beds. The major source of anisotropy in the area is the abundant shales in the shallower part of the section (Alkhalifah *et al.*, 1996; Tsvankin, 2001). Both heterogeneity and anisotropy have to be taken into account to image the progradational off-lap patterns, some of the weak reflections, the large number of faults, and also position reflectors correctly in depth.

Chapter 2

Analysis of image gathers in homogeneous and factorized $v(z)$ VTI media

2.1 Algorithms for modeling and prestack depth migration

The algorithms described below are used in all applications in this thesis. The first step in the numerical analysis of image gathers is to generate 2-D synthetic seismograms of P-wave reflections in homogeneous and factorized VTI media using the SU (Seismic Unix) code *susynlvfti* Alkhalifah (1995a). To build the 2-D traveltime tables for prestack depth migration, I employ the anisotropic ray-tracing algorithm of Alkhalifah (1995b). The traveltimes τ computed along each ray are then extrapolated to adjacent grid points using the paraxial approximation described by Gajewski and Pšenčík (1987):

$$\tau(\mathbf{x}) = \tau(\bar{\mathbf{x}}) + p_k(\bar{\mathbf{x}})(x_k - \bar{x}_k) + \frac{1}{2} N_{ik}(\bar{\mathbf{x}})(x_i - \bar{x}_i)(x_k - \bar{x}_k)\,, \tag{2.1}$$

where $\mathbf{x}$ corresponds to the point to which I seek to find the traveltime, $\bar{\mathbf{x}}$ defines the coordinate of the point on the central ray from which the traveltime is extrapolated, $\mathbf{p}$ is the slowness vector $p_k(\bar{\mathbf{x}}) = \frac{\partial \tau}{\partial x_k}\Big|_{\bar{\mathbf{x}}}$, and $N_{ik}(\bar{\mathbf{x}}) = \frac{\partial^2 \tau}{\partial x_k \partial x_i}\Big|_{\bar{\mathbf{x}}}$. Following Gajewski and Pšenčík (1987), the matrix of the second traveltime derivatives N_{ik} can be written as

$$N_{ik} = \frac{\partial p_i}{\partial x_k} = \frac{\partial p_i}{\partial \gamma_j} \left(\frac{\partial x_k}{\partial \gamma_j} \right)^{-1}, \tag{2.2}$$

where i,k take values 1,2, γ_1 is the takeoff angle at the source (usually denoted by ψ) and $\gamma_2 = \tau$. The slownesses $p_k(\bar{\mathbf{x}})$ and the derivatives $\frac{\partial p_i}{\partial \tau}$ and $\frac{\partial x_k}{\partial \tau}$ can be computed while tracing the central ray.

The derivatives $\frac{\partial p_i}{\partial \psi}$ and $\frac{\partial x_k}{\partial \psi}$, however, are evaluated with respect to takeoff angle along the wavefront [for a constant τ], which requires tracing at least one additional (auxiliary) ray. If $\psi + \Delta\psi$ is the takeoff angle of an auxiliary ray, then the derivatives with respect to ψ can be found by linear interpolation for a fixed traveltime τ:

$$\begin{aligned} \frac{\partial p_i}{\partial \psi} &\approx \frac{p_i(\psi + \Delta\psi) - p_i(\psi)}{\Delta\psi}\,, \\ \frac{\partial x_i}{\partial \psi} &\approx \frac{x_i(\psi + \Delta\psi) - x_i(\psi)}{\Delta\psi}\,. \end{aligned} \tag{2.3}$$

After using equations (2.3) to compute N_{ik} [equation (2.2)], I calculate the extrapolated traveltimes $\tau(\mathbf{x})$ from equation (2.1). The traveltime tables are used in a Kirchhoff prestack depth-migration code *sukdmig2d* originally designed for isotropic models (Liu, 1997) to generate image gathers in VTI media. Codes *rayt2dan* and *sukdmig2d* are used in all traveltime computations and prestack depth-migration examples in this thesis.

2.2 Homogeneous VTI medium

To study the trajectory $z(h)$ of a migrated event in an image gather [equation (1.4)], I applied the weak-anisotropy approximation (Appendix A). For a horizontal reflector embedded in a homogeneous VTI medium, linearization in the parameters ϵ and δ yields

$$z_M^2(h) = \gamma^2 z_T^2 + h^2\, V_{P0,M}^2 \left(\frac{1}{V_{\text{nmo},T}^2} - \frac{1}{V_{\text{nmo},M}^2} \right) + \frac{2h^4}{h^2 + z_T^2} \left(\eta_M \frac{V_{\text{nmo},T}^2}{V_{\text{nmo},M}^2} - \eta_T \frac{V_{\text{nmo},M}^2}{V_{\text{nmo},T}^2} \right), \quad (2.4)$$

where the subscript T refers to the true model and M to the model used for migration, $z_M(h)$ is the migrated depth for the half-offset h, z_T is the true depth of the zero-offset reflection point, $\gamma \equiv V_{P0,M}/V_{P0,T}$ is the ratio of the migration to true vertical velocity, $V_{\text{nmo}} = V_{P0}\sqrt{1+2\delta}$ is the zero-dip normal-moveout (NMO) velocity, and $\eta \equiv (\epsilon - \delta)/(1+2\delta)$ is the anellipticity parameter of Alkhalifah and Tsvankin (1995), which is responsible for time processing of P-wave data in VTI media with a laterally homogeneous overburden.

Equation (2.4) shows that the moveout of horizontal events on an image gather is fully controlled by the parameters V_{nmo} and η, with V_{nmo} responsible for the near-offset moveout and the influence of η becoming substantial only at large offsets. Only if the migration and true values of these two parameters are identical ($V_{\text{nmo},M} = V_{\text{nmo},T}$ and $\eta_M = \eta_T$), will the migrated depth $z_M(h)$ [equation (2.4)] be independent of the offset h, and the event in the image gather is flat.

Although equation (2.4) was derived for a horizontal reflector, the correct values of V_{nmo} and η are sufficient for removing residual moveout on image gathers of dipping events as well (see the numerical examples below). This conclusion follows from the general result of Alkhalifah and Tsvankin (1995), who proved that P-wave reflection traveltime moveout in VTI media with a laterally homogeneous overburden depends only on the zero-offset traveltime, V_{nmo} and η. Positioning an image gather at the true depth, however, requires using the correct vertical velocity ($V_{P0,M} = V_{P0,T}$, which makes $\gamma = 1$).

Figure 2.1a displays an image gather for two horizontal reflectors embedded in a homogeneous VTI medium at depths of 1000 m and 2000 m. The gather was computed for a model with the true parameters $V_{\text{nmo},M} = V_{\text{nmo},T}$ and $\eta_M = \eta_T$, but intentionally inaccurate values of the vertical velocity V_{P0} and the coefficients ϵ and δ. Consistent with the conclusions of Alkhalifah and Tsvankin (1995), setting V_{nmo} and η to the correct values ensures that both events in the image gather are flat. The same conditions ($V_{\text{nmo},M} = V_{\text{nmo},T}$ and $\eta_M = \eta_T$) are sufficient to flatten events from dipping reflectors in Figure 2.1b.

Since the migration was performed with the wrong value of V_{P0}, however, the migrated depths are scaled by the factor $\gamma \approx 0.90$. In agreement with equation (2.4), the depth of

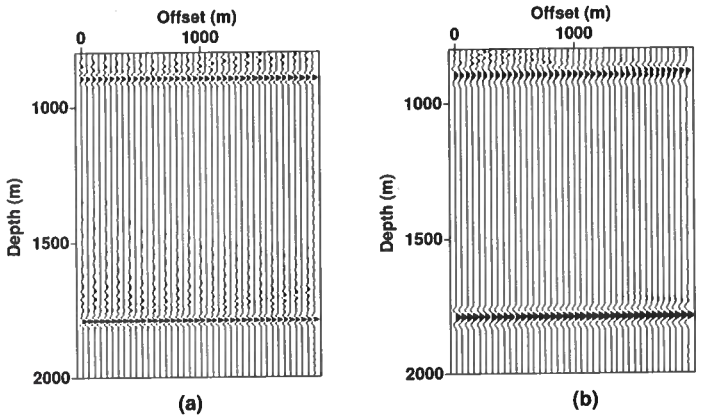

Figure 2.1. Image gathers for (a) two horizontal reflectors and (b) two reflectors dipping at 30° embedded in a homogeneous VTI medium. The true model parameters in Figures 2.1–2.3 are $V_{P0,T} = 2000$ m/s, $\epsilon_T = 0.1$, and $\delta_T = -0.1$. Prestack depth migration was performed for a model with different values of V_{P0}, δ, and ϵ, but with the correct $V_{\mathrm{nmo},M} = V_{\mathrm{nmo},T} = 1789$ m/s and $\eta_M = \eta_T = 0.25$ ($\epsilon_M = 0.25$, $\delta_M = 0$). For this and subsequent figures, the maximum offset-to-depth ratio $x_{\max}/z = 2h_{\max}/z$ is equal to two for the shallow reflector (in the true model) and one for the deep reflector.

the shallow event is close to 900 m instead of 1000 m, and the deep one is located at 1800 m instead of 2000 m.

For horizontal events, the parameter η contributes only to the far-offset moveout term [equation (2.4)], which is also true for the P-wave nonhyperbolic reflection moveout equation (Alkhalifah and Tsvankin, 1995; Tsvankin, 2001). Therefore, the influence of η becomes substantial for only relatively large offset-to-depth ratios, e.g., those exceeding unity (Figure 2.2a). If the reflector is dipping, η contributes to small-offset traveltimes as well because it governs the dip dependence of NMO velocity (Alkhalifah and Tsvankin, 1995; Tsvankin, 2001). Figures 2.2b and 2.2c confirm that for dipping events (the dips are 30° and 45°) the residual moveout caused by errors in η is not confined to long offsets. The depth error at the largest offset increases from 30 m for the horizontal reflector (Figure 2.2a) to 50 m for the reflector dipping at 30° (Figure 2.2b), but then decreases to 35 m for a dip of 45° (Figure 2.2c); this behavior of residual moveout agrees with the prediction of Jaramillo and Larner (1995). Although the contribution of η to the NMO velocity becomes more significant with dip, the magnitude of reflection moveout decreases for steeper reflectors, which explains this dependence of residual moveout on errors in η.

The NMO velocity in equation (2.4) not only controls the quadratic term h^2 that dominates the moveout for offsets used in our examples, but also influences the far-offset moveout term. Hence, an inaccurate value of V_{nmo} leads to significant residual moveout for the whole offset range.

For the example in Figure 2.3, the depth error at the largest offset reaches 80 m for

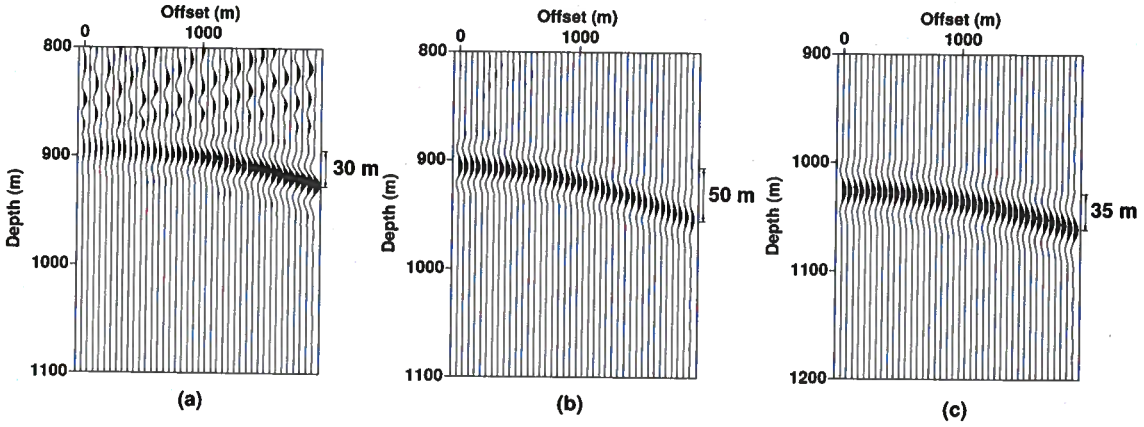

Figure 2.2. Image gathers for reflectors dipping at (a) 0°, (b) 30°, and (c) 45° computed for an overstated value of η ($\eta_M = 0.4$, while $\eta_T = 0.25$). Migration was done with the correct V_{nmo} and distorted $\epsilon_M = 0.4$ and $\delta_M = 0$.

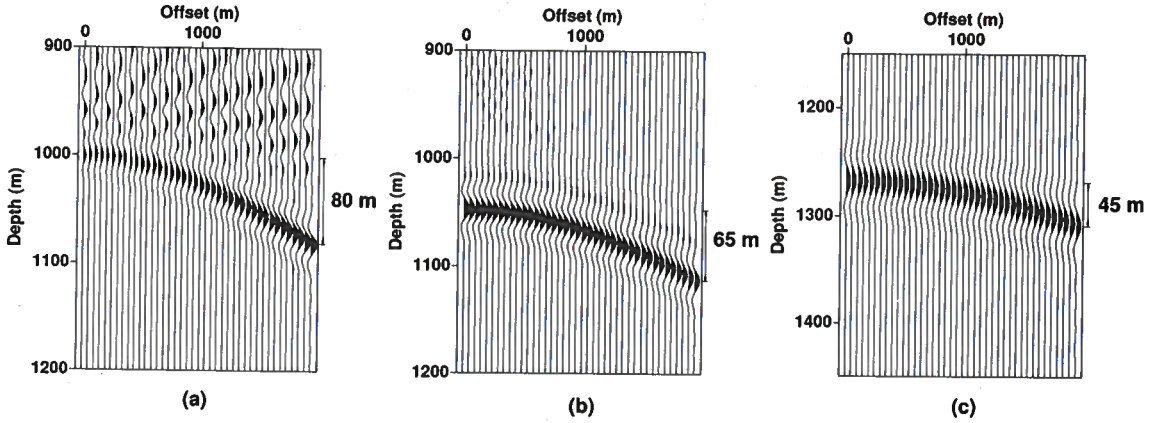

Figure 2.3. Image gathers for reflectors dipping at (a) 0°, (b) 30° and (c) 45° computed for an overstated value of V_{nmo} ($V_{\text{nmo},M} = 2000$ m/s, while $V_{\text{nmo},T} = 1789$ m/s). Migration was done with the correct η and distorted $\epsilon_M = 0.25$ and $\delta_M = 0$.

the horizontal reflector and decreases to 65 m for the 30° reflector, and to 45 m for a dip of 45°. This steady decrease in residual moveout with dip for a fixed error in $V_{\rm nmo}$ is caused by the smaller magnitude of reflection moveout and its lower sensitivity to $V_{\rm nmo}$ for larger dips. Liu (1997) noticed this phenomenon for isotropic media, and his analysis remains qualitatively valid in the presence of anisotropy.

2.3 Factorized $v(z)$ VTI medium

Factorized $v(z)$ VTI media with linear velocity variation can be described by four independent parameters: the vertical velocity $V_{P0} = V_{P0}(0)$ defined at zero depth $z = 0$, the velocity gradient k_z responsible for the linear variation of V_{P0} in the z–direction, and Thomsen parameters ϵ and δ (for P-waves). As follows from the results of Appendix B, events in an image gather at zero-offset time t_0 can be flattened by using the correct values for NMO velocity ($v_{\rm nmo}$) and the effective parameter $\hat{\eta}$ given by

$$v_{\rm nmo}^2(t_0) = \frac{V_{P0}^2(1+2\delta)}{t_0\, k_z}\left[e^{k_z\, t_0} - 1\right], \tag{2.5}$$

$$\hat{\eta}(t_0) = \frac{1}{8}\left\{\frac{(1+8\eta)\,(e^{2k_z\, t_0} - 1)\, k_z\, t_0}{2(e^{k_z t_0} - 1)^2} - 1\right\}, \tag{2.6}$$

where t_0 is the zero-offset traveltime. Note that both the NMO velocity and $\hat{\eta}$ are dependent on the vertical gradient k_z. The difference between $\hat{\eta}$ and η, and between $v_{\rm nmo}(t_0)$ and $v_{\rm nmo}(t_0 = 0) = V_{P0}\sqrt{1+2\delta} \equiv V_{\rm nmo}$ increases with the absolute value of k_z.

However, since the vertical velocity in a factorized $v(z)$ medium changes with depth, flattening an event for a certain depth z_T does not ensure that the same velocity model will flatten events for any other depth. To illustrate this point, consider two horizontal reflectors at the depths 1000 m and 2000 m embedded in a factorized $v(z)$ medium (Figure 2.4). To migrate data acquired over such a model, I use a homogeneous VTI medium with the parameters chosen such that $V_{\rm nmo}$ and η for the homogeneous model are equal to their effective values for the shallow reflector. As expected, the shallow event in the image gather is flat, but the deeper event exhibits substantial residual moveout because the NMO velocity and η used in migration are too low for a depth of 2000 m.

To ensure that events are flat for the whole depth range of the reflectors, the effective NMO velocity and the parameter $\hat{\eta}$ for both the migration and true models should be equal at all zero-offset times t_0. Therefore, both the exponential term in equation (2.5) and the coefficient in front of it should be preserved in the migration model, which means that migration should be done with the correct values of both the NMO velocity at the surface and the vertical gradient: $V_{{\rm nmo},M} = V_{P0,M}\sqrt{1+2\delta_M} = V_{P0,T}\sqrt{1+2\delta_T} = V_{{\rm nmo},T}$, and $k_{z,M} = k_{z,T}$. Taking into account that $k_{z,M}$ has to be equal to $k_{z,T}$, the condition $\hat{\eta}_M = \hat{\eta}_T$ can be satisfied at all t_0 only if $\eta_M = \eta_T$ [see equation (2.6)].

I conclude that to flatten all horizontal events in image gathers for a factorized $v(z)$ medium, three conditions need to be satisfied: (1) $V_{{\rm nmo},M} = V_{{\rm nmo},T}$, (2) $k_{z,M} = k_{z,T}$, and (3) $\eta_M = \eta_T$. Although in principle all three conditions follow from the general result

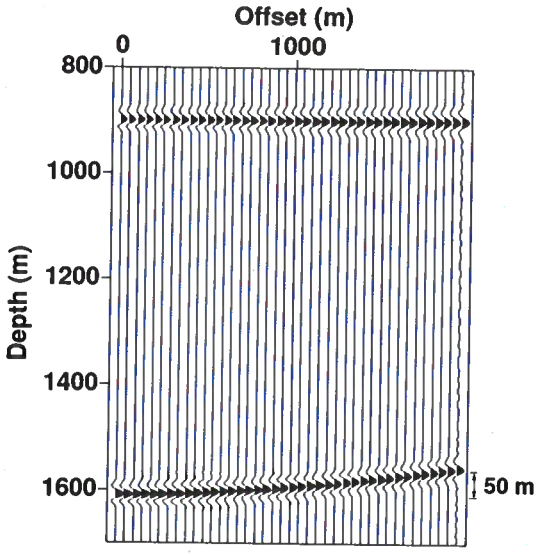

Figure 2.4. An image gather for two horizontal reflectors in a factorized $v(z)$ VTI medium obtained using a homogeneous migration model with the NMO velocity and η equal to their effective values for the shallow reflector. In Figures 2.4–2.6 the true parameters are $V_{P0,T} = 2000$ m/s, $k_{z,T} = 0.6$ s^{-1}, $\epsilon_T = 0.1$, and $\delta_T = -0.1$; the parameters used here for the migration are $V_{P0,M} = 2054$ m/s, $\epsilon_M = 0.26$ and $\delta_M = 0$.

of Alkhalifah and Tsvankin (1995), the results given here for factorized VTI media have not been obtained before. In particular, I have shown that flattening events for a range of zero-offset times requires using the correct vertical velocity gradient k_z. This implies that velocity analysis on image gathers in VTI media may be used to constrain not just the parameters $V_{\rm nmo}$ and η (as expected), but also k_z.

Figure 2.5a confirms that if the parameters $V_{\rm nmo}$, k_z, and η are the same for the migration and true models (although the Thomsen parameters of those models may widely differ), horizontal events in image gathers are flat. Moreover, these three conditions are also sufficient to flatten dipping events (Figure 2.5b).

The depths in an image gather for a horizontal reflector embedded in a factorized $v(z)$ VTI medium can be described by the following equation (Appendix B):

$$\begin{aligned} z_M^2(h) \;\approx\; & z_M^2(0) + h^2\,\hat{V}_{P0,M}^2 \left\{ \frac{1}{v_{\rm nmo,T}^2(z_T)} - \frac{1}{v_{\rm nmo,M}^2[z_M(0)]} \right\} \\ & + \frac{2h^4}{h^2 + z_T^2} \left\{ \hat{\eta}_M[z_M(0)] \frac{v_{\rm nmo,T}^2(z_T)}{v_{\rm nmo,M}^2[z_M(0)]} - \hat{\eta}_T(z_T) \frac{v_{\rm nmo,M}^2[z_M(0)]}{v_{\rm nmo,T}^2(z_T)} \right\}. \end{aligned} \tag{2.7}$$

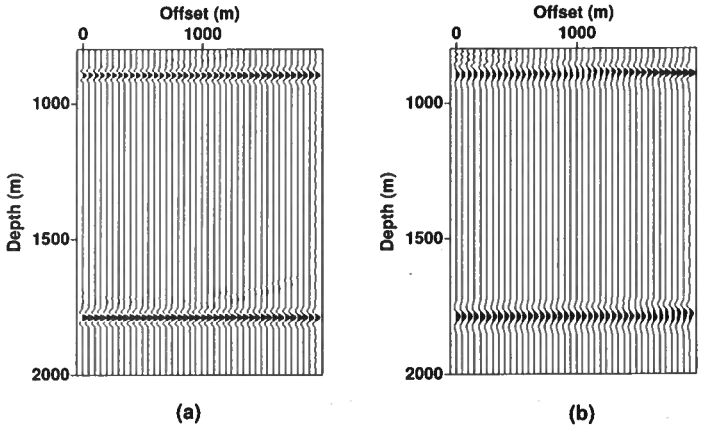

Figure 2.5. Image gathers for (a) two horizontal reflectors and (b) two reflectors dipping at 30° embedded in a factorized $v(z)$ VTI medium. Prestack depth migration was performed for a model with distorted Thomsen parameters, but one that has the correct $V_{\mathrm{nmo},M} = V_{\mathrm{nmo},T} = 1789$ m/s, $k_{z,M} = k_{z,T} = 0.6$ s^{-1}, and $\eta_M = \eta_T = 0.25$ ($\epsilon_M = 0.25$, $\delta_M = 0$, $\epsilon_T = 0.1$, $\delta_T = -0.1$).

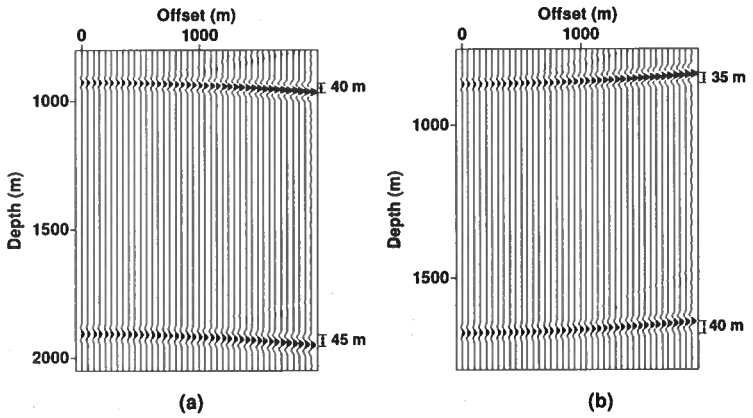

Figure 2.6. Image gathers for two horizontal reflectors computed for inaccurate values of the vertical velocity gradient. Migration was done with the correct V_{nmo} and η, but distorted values of $k_{z,M}$. (a) $k_{z,M} - k_{z,T} = 0.15$ s^{-1}; (b) $k_{z,M} - k_{z,T} = -0.15$ s^{-1}.

Here, $z_M(0) = \gamma z_T$, $\gamma \equiv \hat{V}_{P0,M}/\hat{V}_{P0,T}$, and $\hat{V}_{P0}$ is the average vertical velocity above the reflector. Equation (2.7), obtained for moderate offsets and under the assumption that the migration model is close to the true model, has the same form as the corresponding expression (2.4) for homogeneous media. Note that the reflector depth is scaled by the factor γ, which in heterogeneous media depends on the ratio of the average vertical velocities in the migration and true models ($\gamma \approx 0.9$ in Figure 2.5).

Because of the similarity between equations (2.4) and (2.7), the influence of errors in $V_{\rm nmo}$ or η on image gathers in factorized $v(z)$ media resembles that for homogeneous media. Therefore, here I focus on the sensitivity of image gathers in the $v(z)$ model to the gradient k_z. Figure 2.6 illustrates the distortions of image gathers of horizontal events resulting from errors in k_z. Too large a value of k_z leads to an erroneously high NMO velocity, and an event in the image gather is undercorrected (Figure 2.6a), while choosing $k_{z,M} < k_{z,T}$ is equivalent to understating the NMO velocity (Figure 2.6b). Since an erroneous k_z causes the corresponding error in the NMO velocity to increase with depth, the residual moveout in Figure 2.6 is more substantial for the deep event.

The dip dependence of residual moveout for a fixed error in k_z is similar to that observed in a homogeneous medium for an error in $V_{\rm nmo}$. If for the model in Figure 2.6 k_z is overstated by 0.15 s^{-1}, the residual moveout decreases from 40 m for the shallow horizontal reflector to 35 m for a dip of 30°, and to 30 m for a dip of 45°. Since the variation in the residual moveout for a range of dips is small, it implies that the influence of an error in k_z on the moveout is almost independent of the dip.

2.4 Possible distortions of stacked images

If the value of $V_{\rm nmo}$, k_z, or η is wrong, events in image gathers exhibit residual moveout, and reflectors are poorly focused. Examples of poorly focused images are shown in Figures 2.7-2.9. Because inaccuracies in η do not influence the vertical velocity variation, reflectors in Figure 2.7, although poorly focused, are positioned at the correct depth. An error in k_z, however, results in an error in $V_{P0}(z)$ and causes reflectors in Figure 2.8 to not only be poorly focused, but also be imaged at the wrong depths. Figure 2.9b also shows poorly focused reflectors at the wrong depth because the imaging was done with the wrong values of both V_{P0} and $V_{\rm nmo}$.

If $V_{\rm nmo}$, k_z, and η are correct, then both horizontal and dipping reflectors are well focused (Figures 2.10 and 2.11). But, if V_{P0} is chosen too low, then reflectors are imaged at too shallow a depth (Figure 2.10), and if V_{P0} is too high, then reflectors are imaged too deep (Figure 2.11). Figures 2.10 and 2.11 also show that choosing too small a value for V_{P0} cause dipping reflectors to be imaged with smaller than the correct dips, while too large a value of V_{P0} increases the imaged dips. Figure 2.10, generated for implausibly large anisotropic coefficients ϵ and δ, demonstrates that the conditions that need to be satisfied to flatten events in factorized $v(z)$ media are independent of the strength of anisotropy.

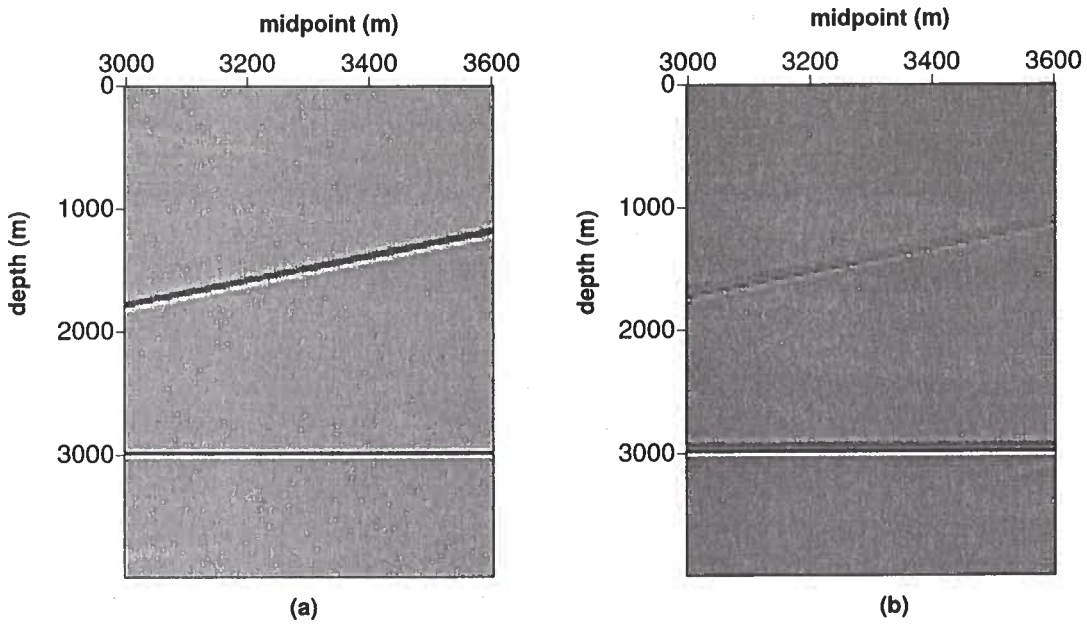

Figure 2.7. Comparison of stacked images of horizontal and dipping (45°) reflectors: (a) for the correct medium parameters ($V_{P0} = 2000$ m/s, $k_z = 0.6$/s, $\epsilon = 0.3$ and $\delta = 0.1$) and (b) for an incorrect value of $\eta = 0.08$ instead of $\eta = 0.17$ ($V_{P0} = 2000$ m/s, $k_z = 0.6$/s, $\epsilon = 0.2$, and $\delta = 0.1$).

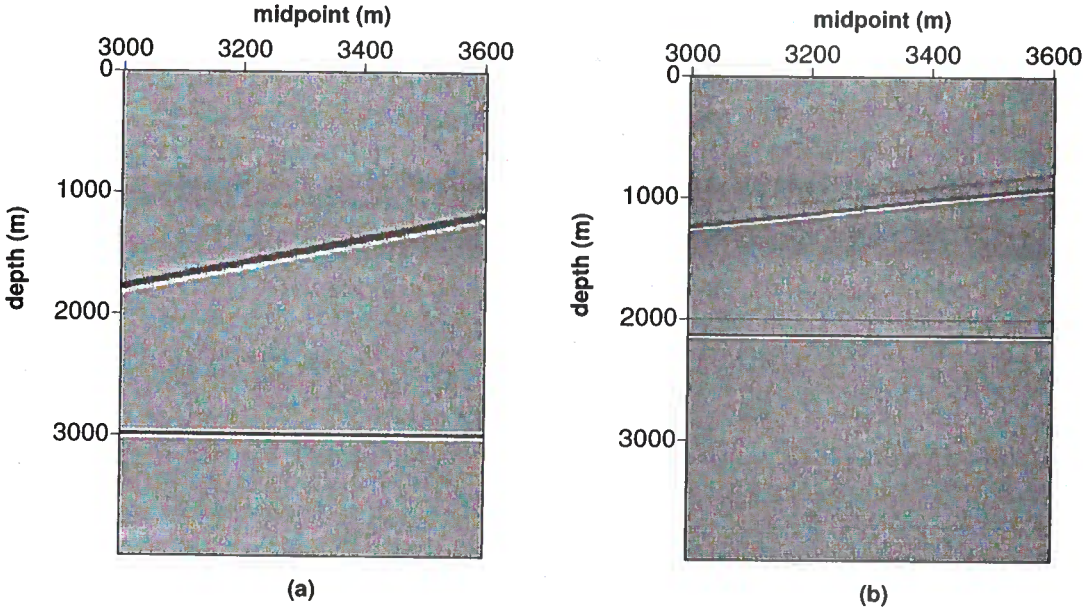

Figure 2.8. Same as Figure 2.7, but section (b) was obtained for an incorrect value of k_z ($V_{P0} = 2000$ m/s, $k_z = 0.0$/s, $\epsilon = 0.3$, and $\delta = 0.1$).

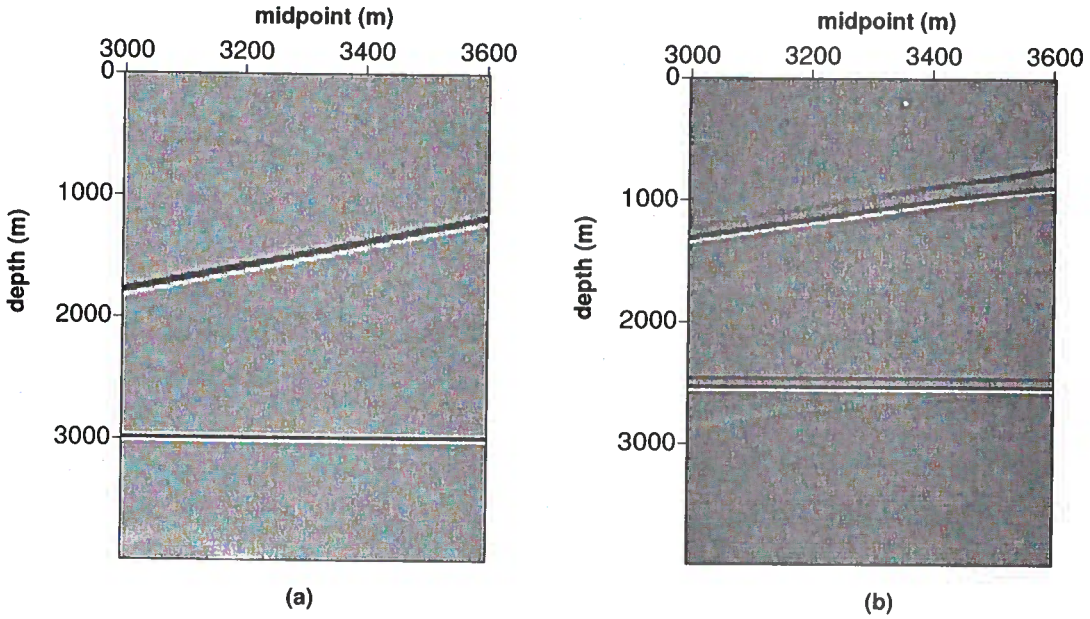

Figure 2.9. Same as Figure 2.7, but section (b) was obtained for an incorrect value of V_{nmo} ($V_{P0} = 1700$ m/s, $k_z = 0.6$/s, $\epsilon = 0.3$, and $\delta = 0.1$).

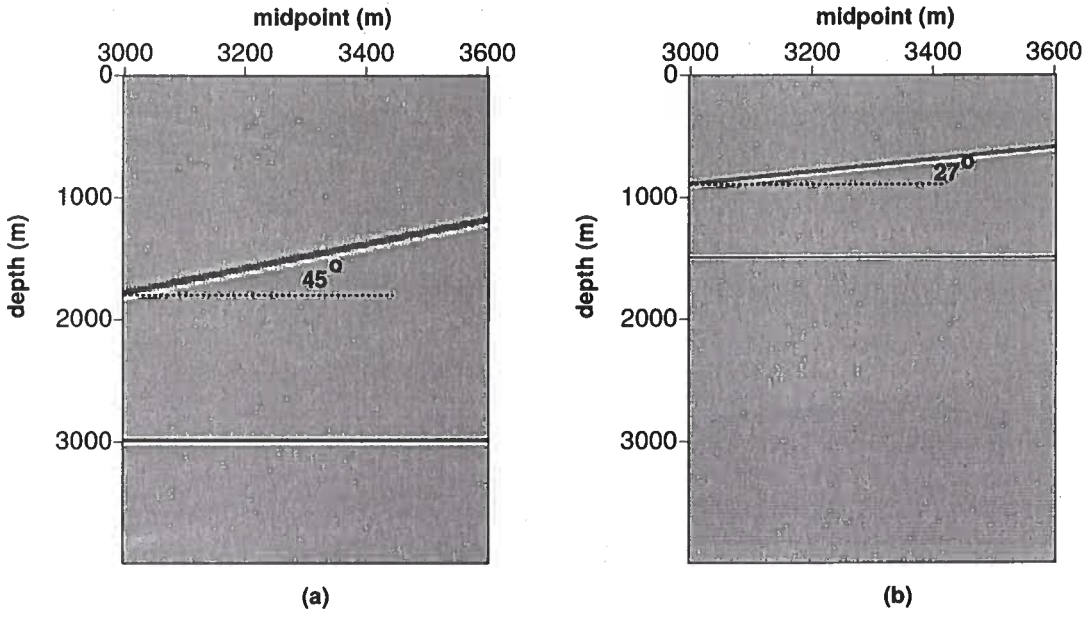

Figure 2.10. Same as Figure 2.7, but section (b) was obtained for the correct V_{nmo}, k_z and η, and $V_{P0,M} = \frac{1}{2}V_{P0,T}$ ($V_{P0} = 1000$ m/s, $k_z = 0.6$/s, $\epsilon = 2.7$, and $\delta = 1.9$). Abnormally high values of ϵ and δ were intentionally chosen to show that the conditions outlined in the text are valid for any strengths of anisotropy. Because V_{nmo}, k_z and η are correct, and $V_{P0,M} < V_{P0,T}$, the reflectors in Figure 2.10b are well focused, but imaged at smaller depths.

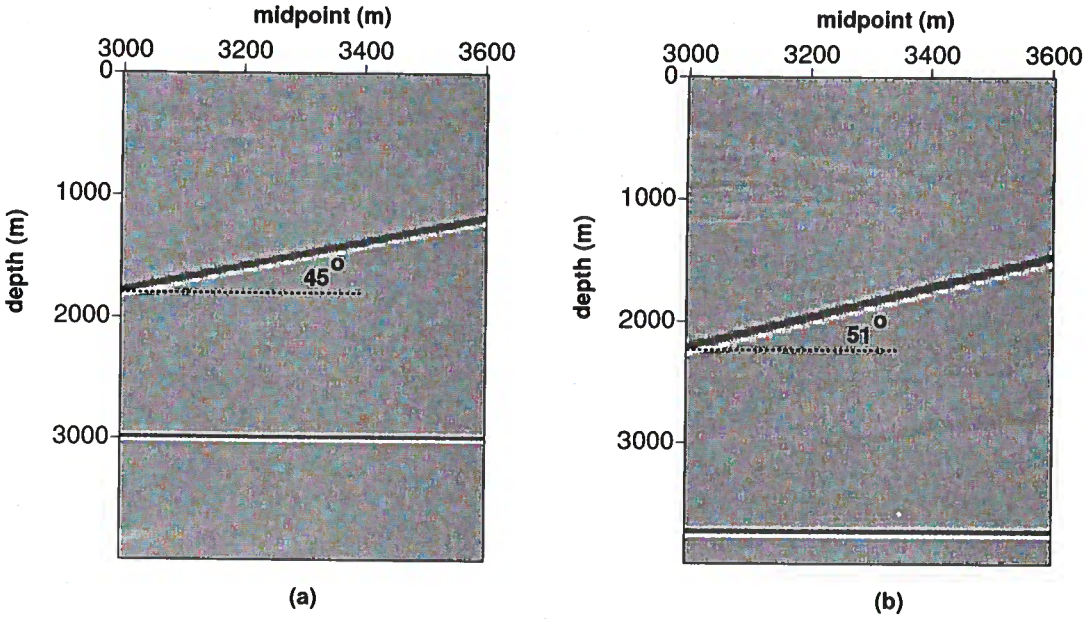

Figure 2.11. Same as Figure 2.10, but section (b) was obtained for $V_{P0,M} > V_{P0,T}$. (V_{P0} = 2500 m/s, $k_z = 0.6$/s, $\epsilon = 0.01$, and $\delta = -0.12$). Because $V_{\rm nmo}$, k_z and η are correct, and $V_{P0,M} > V_{P0,T}$, the reflectors in Figure 2.11b are well focused, but imaged at larger depths.

Chapter 3

Analysis of image gathers in factorized $v(x, z)$ media

3.1 Factorized $v(x, z)$ VTI medium

Factorized $v(x, z)$ VTI media with linear velocity variation can be described by five independent parameters: the vertical velocity $V_{P0} = V_{P0}(0, 0)$ defined at zero depth $z = 0$ and lateral location $x = 0$, the velocity gradients k_x and k_z responsible for the linear variation of V_{P0} in the x– and z–directions, respectively, and Thomsen parameters ϵ and δ (for P-waves).

To analyze the effect of k_x on the residual moveout of events, consider image gathers (Figure 3.1) from two horizontal reflectors embedded in factorized $v(x)$ media ($k_{z,T} = 0.0$). Migration was done with the correct $V_{\rm nmo}$ for the selected midpoint location in the correct background homogeneous medium and η. Figures 3.1a-c show that the residual moveout caused by ignoring k_x is negligible for small values of k_x ($k_x \leq 0.2$ s^{-1}), which implies that for weak lateral gradients the moveout of events is dependent only on the background NMO velocity at that midpoint location and the parameter η. The influence of k_x tends to increase with k_x, and for a relatively large value ($k_x = 0.3$) its influence can be significant (Figure 3.1d). The effect of k_x is visible only at far offsets, which suggests that k_x influences η more than $V_{\rm nmo}$ because of the more significant ray-bending that occurs at large offsets.

These conclusions can be readily extended to media with $k_z \neq 0$, where the moveout of events at a midpoint location is governed by the effective quantities $v_{\rm nmo}$ and $\hat{\eta}$, instead of $V_{\rm nmo}$ and η. To derive the conditions necessary to flatten all events in image gathers in a factorized $v(x, z)$ medium, I assume that the lateral heterogeneity is weak enough for the influence of k_x on the moveout to be negligible. Later in this chapter, however, I show that these conditions are applicable to strongly heterogeneous anisotropic media as well.

If we consider the factorized $v(x, z)$ model as being composed of narrow vertical strips of $v(z)$ factorized media, then image gathers in $v(x, z)$ media will be flat if $v_{{\rm nmo},M}(x, t_0) = v_{{\rm nmo},T}(x, t_0)$ and $\hat{\eta}_M(x, t_0) = \hat{\eta}_T(x, t_0)$ not only for all vertical times t_0, but also for all coordinates x. The influence of weak lateral velocity variation on the NMO velocity in horizontally layered anisotropic media was discussed by Grechka and Tsvankin (1999). They showed that in the presence of lateral heterogeneity the NMO ellipse for homogeneous media has to be corrected for lateral velocity variation by including a term dependent on the second derivatives of the vertical velocity with respect to the horizontal coordinates. For the 2-D

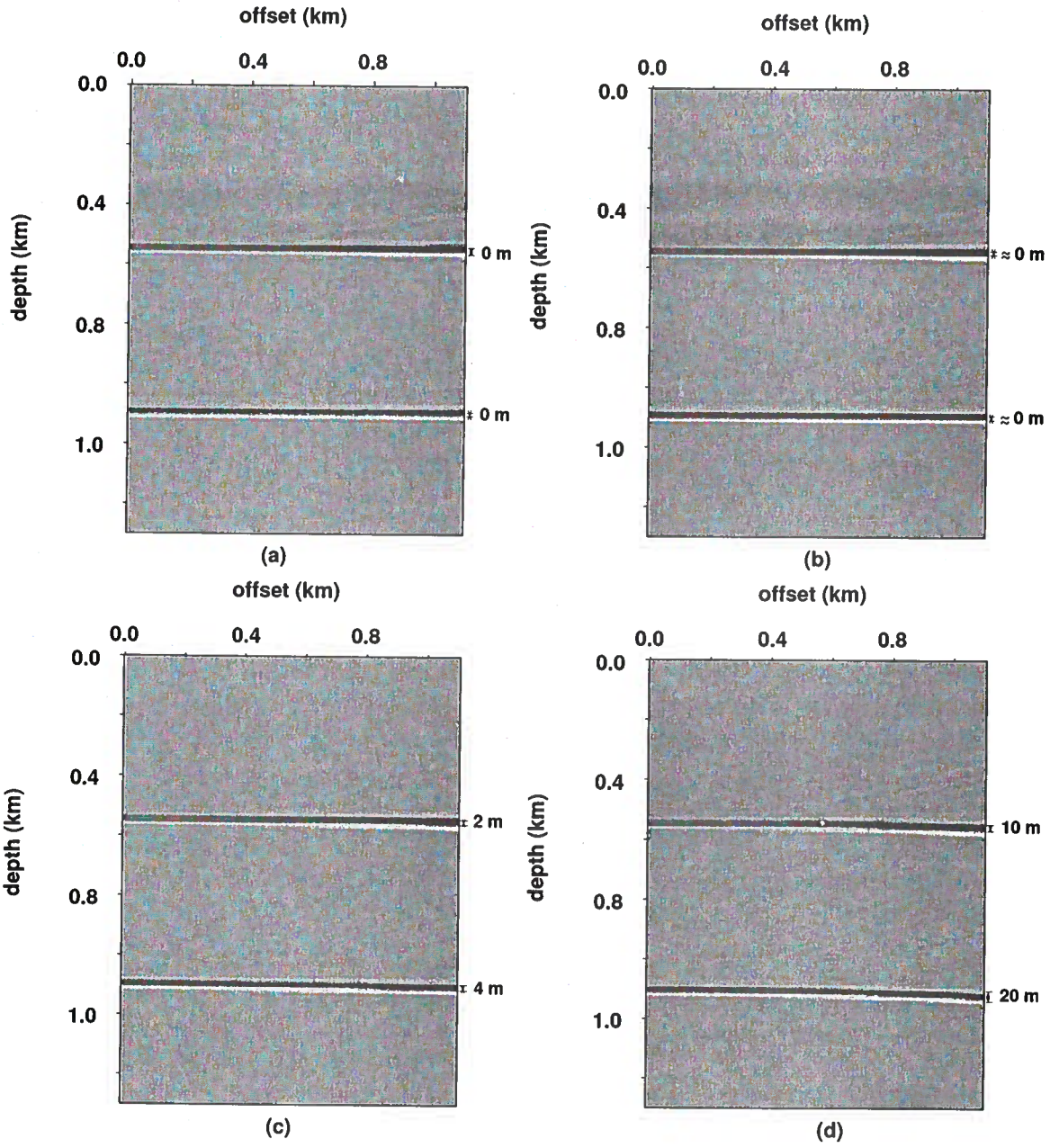

Figure 3.1. Image gathers at the same midpoint location for four different factorized $v(x)$ models: (a) $k_{x,T} = 0$, (b) $k_{x,T} = 0.1$ s^{-1}, (c) $k_{x,T} = 0.2$ s^{-1}, and (d) $k_{x,T} = 0.3$ s^{-1}. For all models $V_{P0,T}$ at the surface for this location is equal to 2000 m/s, $k_{z,T} = 0$, $\epsilon_T = 0.2$, and $\delta_T = 0.1$. Migration was done with the correct background values of $V_{\text{nmo}} = 2190$ m/s and $\eta = 0.083$, but incorrect $k_{x,M} = 0.0$ and $\delta_M = 0.0$. The maximum offset-to-depth ratio is about two for the shallow event and about one for the deeper event. The residual moveout is significant only for $k_x = 0.3$ s^{-1} (Figure 3.1d).

model considered here, the equation of Grechka and Tsvankin (1999) takes the form

$$v_{\rm nmo}^{-2}(x,z) = v_{\rm nmo,hom}^{-2}(x,z) + \frac{\tau_0(x,z)}{3}\,\frac{\partial^2 \tau_0(x,z)}{\partial x^2}\,, \tag{3.1}$$

where $v_{\rm nmo,hom}$ is the NMO velocity in the background laterally homogeneous medium at the coordinate x, z is the reflector depth and $\tau_0(x,z)$ is the one-way zero-offset reflection traveltime. Since in our model $V_{P0}(x,z)$ and, for weak lateral velocity variation, $\tau_0(x,z)$ are linear functions of x, $v_{\rm nmo}(x,z)$ from equation (3.1) is simply equal to the NMO velocity in the background factorized $v(z)$ medium at the lateral location x. Using equation (B.5), the background NMO velocity can be represented as

$$v_{\rm nmo,hom}^2(x,z) = \frac{V_{P0}^2(x)(1+2\delta)}{2\,t_{\rm hom}(x,z)\,k_z}\left[e^{2k_z t_{\rm hom}(x,z)} - 1\right], \tag{3.2}$$

where the vertical P-wave velocity at the surface $V_{P0}(x) = V_{P0} + k_x\,x$, $t_{\rm hom}(x,z) = z/\hat{V}_{P0}(x,z)$, and $\hat{V}_{P0}(x,z)$ is the average vertical velocity above the reflector.

As follows from our results for the $v(z)$ model, $v_{\rm nmo}$ of horizontal events is equal to the true NMO velocity for all vertical times t_0 if the migration is based on the correct values of the vertical velocity gradient k_z and NMO velocity at the surface $[V_{P0}(x)\sqrt{1+2\delta}]$. Hence, $k_{z,M}$ should be equal to $k_{z,T}$, and

$$(V_{P0,M} + k_{x,M}\,x)\sqrt{1+2\delta_M} = (V_{P0,T} + k_{x,T}\,x)\sqrt{1+2\delta_T}\,, \tag{3.3}$$

which implies that $V_{{\rm nmo},M} = V_{P0,M}\sqrt{1+2\delta_M} = V_{P0,T}\sqrt{1+2\delta_T} = V_{{\rm nmo},T}$, and $k_{x,M}\sqrt{1+2\delta_M} = k_{x,T}\sqrt{1+2\delta_T}$. Also, because $k_{z,M} = k_{z,T}$, setting $\hat{\eta}_M(x,t_0) = \hat{\eta}_T(x,t_0)$ [equation (2.6)] for all zero-offset times and lateral positions implies that $\eta_M = \eta_T$.

I conclude that flattening all image gathers of horizontal events in a factorized $v(x,z)$ medium requires satisfying four conditions:

1. $V_{{\rm nmo},M} = V_{{\rm nmo},T}$,
2. $k_{z,M} = k_{z,T}$,
3. $\eta_M = \eta_T$,
4. $\hat{k}_{x,M} = k_{x,M}\sqrt{1+2\delta_M} = k_{x,T}\sqrt{1+2\delta_T} = \hat{k}_{x,T}$.

The first three conditions coincide with those obtained for $v(z)$ media, and (4) is an additional constraint on a combination of the horizontal velocity gradient and the parameter δ. Observe that even in the presence of lateral heterogeneity, moveout on image gathers constrains the vertical gradient k_z. While estimation of k_z is feasible, the individual values of the horizontal gradient k_x and the parameters V_{P0}, ϵ, and δ remain unconstrained and cannot be found using P-wave reflection moveout alone.

As illustrated in Figure 3.2a, the conditions listed above indeed ensure that the horizontal events are flat, even if the migration is done with erroneous model parameters.

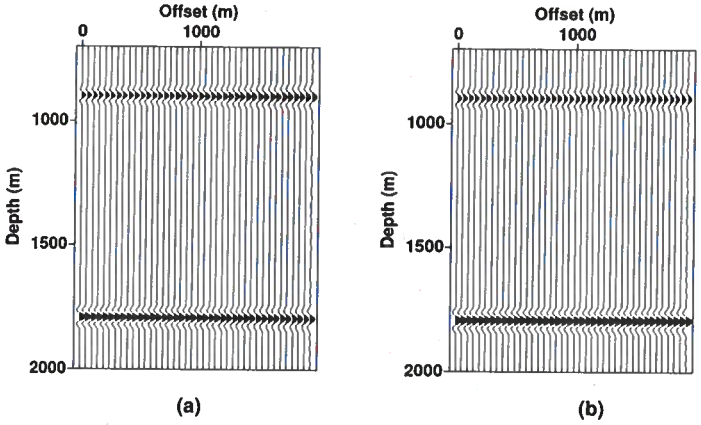

Figure 3.2. Image gathers for (a) two horizontal reflectors and (b) two reflectors dipping at 30° embedded in a factorized $v(x,z)$ VTI medium. In Figures 3.2–3.7 the true model parameters are $V_{P0,T}$=2000 m/s, $k_{z,T}$=0.6 s^{-1}, $k_{x,T}$=0.2 s^{-1}, ϵ_T=0.1, and δ_T=−0.1, and the gathers are centered at lateral coordinate x = 6000 m. Prestack depth migration was performed for a model with distorted parameters, but one that has the correct $V_{\text{nmo},M} = V_{\text{nmo},T}$ = 1789 m/s, $k_{z,M} = k_{z,T}$ = 0.6 s^{-1}, $\hat{k}_{x,M} = \hat{k}_{x,T}$ = 0.18 s^{-1}, and $\eta_M = \eta_T$ = 0.25 (ϵ_M = 0.25, δ_M = 0, $k_{x,M}$ = 0.18 s^{-1}).

Because an incorrect vertical velocity was used, however, the depths are stretched by the factor equal to the ratio of the migration $[\hat{V}_{P0,M}(t_0)]$ to the true $[\hat{V}_{P0,T}(t_0)]$ average vertical velocities evaluated at the lateral coordinate x of the zero-offset reflection point. Although equation (3.2) was derived for horizontal reflectors, the same four conditions proved to be sufficient for flattening dipping events in image gathers (Figure 3.2b).

As was with $v(z)$ media, it is impossible to constrain the vertical velocity gradient using a single event because of the trade-off between k_z and the NMO velocity at the surface. Removing the residual moveout of one event in an image gather does not guarantee that events at other depths or lateral coordiates will be flat unless independent information about the vertical and horizontal gradients is available.

Inaccurate values of V_{nmo}, k_z, or $\hat{k}_x$ cause an error in v_{nmo}, and thus introduce residual moveout on image gathers for the whole offset range. Figures 3.3–3.5 illustrate the influence of errors in V_{nmo} and $\hat{k}_x$, while errors in k_z were analyzed above for $v(z)$ media (Figure 2.6). As in homogeneous media, the residual moveout for a fixed error in V_{nmo}, k_z, or $\hat{k}_x$ decreases with reflector dip (e.g., see Figures 3.4a and 3.5).

It is noteworthy that the magnitude of residual moveout caused by a fixed error in V_{nmo} is smaller in factorized media than in homogeneous media for the same $V_{P0,M}$, $V_{P0,T}$, ϵ_M, ϵ_T, δ_M, and δ_T. For example, if the value of V_{nmo} is overstated by 200 m, the residual moveout for the shallow horizontal reflector in a factorized $v(x,z)$ VTI medium reaches 65 m (Figure 3.3b). If the same reflector is embedded in the reference homogeneous VTI medium, the residual moveout increases to 80 m. Likewise, the residual moveout for a fixed error

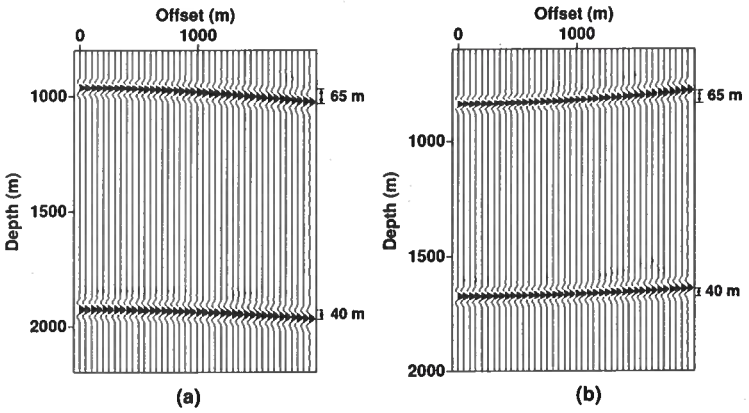

Figure 3.3. Image gathers for two horizontal reflectors computed for inaccurate values of V_{nmo}, but correct k_z, η, and $\hat{k}_x$. (a) $V_{\text{nmo},M} - V_{\text{nmo},T} \approx 200$ m/s ($V_{P0,M} = 2000$ m/s, $\delta_M = 0$); (b) $V_{\text{nmo},M} - V_{\text{nmo},T} \approx -200$ m/s ($V_{P0,M} = 1600$ m/s, $\delta_M = 0$).

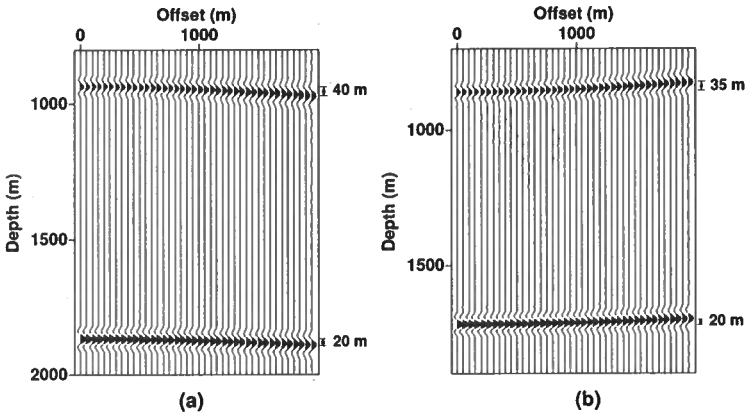

Figure 3.4. Image gathers for two horizontal reflectors computed for inaccurate values of $\hat{k}_x$, but correct V_{nmo}, k_z, and η_M ($\delta_M = 0$). (a) $\hat{k}_{x,M} - \hat{k}_{x,T} = 0.02$ s^{-1}; (b) $\hat{k}_{x,M} - \hat{k}_{x,T} = -0.02$ s^{-1}.

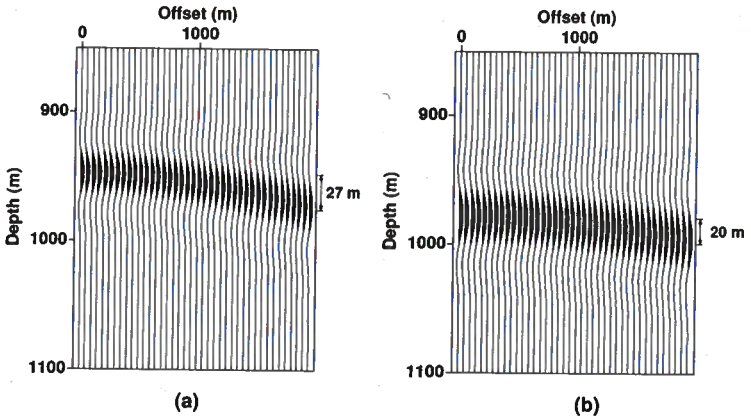

Figure 3.5. Image gathers for reflectors dipping at (a) 30° and (b) 45° computed for a value of $\hat{k}_{x,M}$ overstated by 0.02, but correct V_{nmo}, k_z, and η ($\delta_M = 0$). Note the more detailed view shown in this figure and in Figure 3.7.

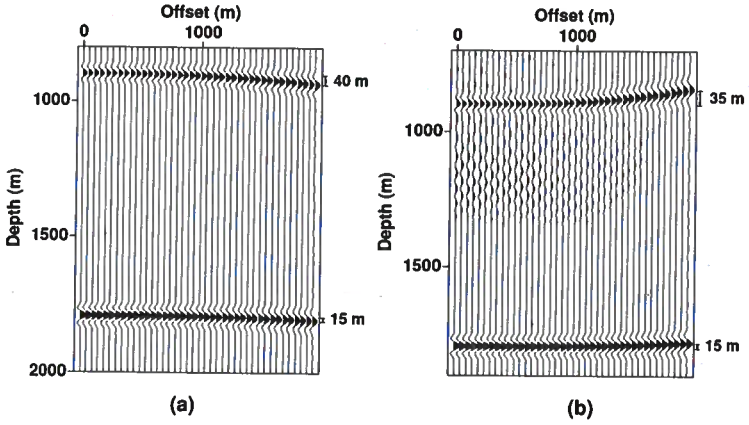

Figure 3.6. Image gathers for two horizontal reflectors computed for inaccurate values of η, but correct V_{nmo}, k_z, and $\hat{k}_x$ (δ_M=0). (a) $\eta_M - \eta_T = 0.15$; (b) $\eta_M - \eta_T = -0.15$.

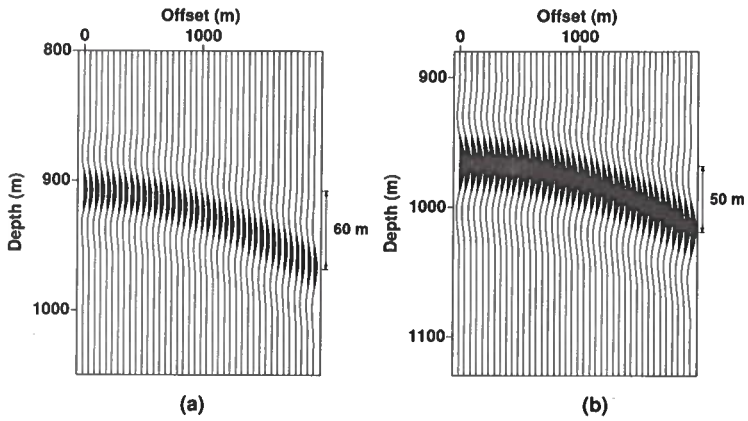

Figure 3.7. Image gathers for reflectors dipping at (a) 30° and (b) 45° computed for a value of η overstated by 0.15, but correct V_{nmo}, k_z, and $\hat{k}_x$ ($\delta_M = 0$).

in k_z is smaller in a $v(x,z)$ medium than in the corresponding laterally homogeneous $v(z)$ model. In contrast, the residual moveout associated with errors in η is larger for factorized $v(x,z)$ media than for the reference homogeneous medium because of the increase in ray bending that occurs in the presence of lateral gradients (compare Figures 2.2a and 3.6a).

The dip dependence of the residual moveout in factorized media for a fixed error in η has the same character as in homogeneous media. For a 0.15 error in η, the residual increases from 40 m for a horizontal reflector (Figure 3.6a) to 60 m for a reflector dipping at 30° (Figure 3.7a), and then decreases to 50 m for a 45° dip (Figure 3.7b).

3.2 Possible distortions of stacked images

Errors in V_{nmo}, k_z, $\hat{k}_x$, or η cause reflectors to be poorly focused in factorized $v(x,z)$ media. The influence of errors in V_{nmo}, k_z, and η is similar to that shown in Figures 2.7-2.9 in Chapter 2, but for $v(x,z)$ media, an error in the velocity model may result in imaging reflectors with erroneous dips, even for horizontal reflectors. As Figure 3.8b shows, an error in $\hat{k}_x$, not only causes misfocussing and depth shifts, but now the horizontal reflector appears dipping. This happens because an error in $\hat{k}_x$ causes a midpoint-dependent error in V_{P0}, which in turn causes a laterally variable depth stretch. In the example shown in Figure 3.8b, this depth stretch increases with the midpoint coordinates, giving rise to the apparent dip in the migrated section.

If the correct values of V_{nmo}, k_z, $\hat{k}_x$, and η are used for migration, the imaged reflectors are well focused, but the depth of the reflectors depend on the value of V_{P0}. Too high a value of V_{P0} causes reflectors to be imaged at greater depths and with greater dips, while too low a value of V_{P0} causes reflectors to be imaged at smaller depths and with smaller dips. Note, however, that as long as the values of V_{nmo}, k_z, and $\hat{k}_x$ are correct, there are no laterally variable depth shifts in the reflectors, even though the value of k_x may be wrong.

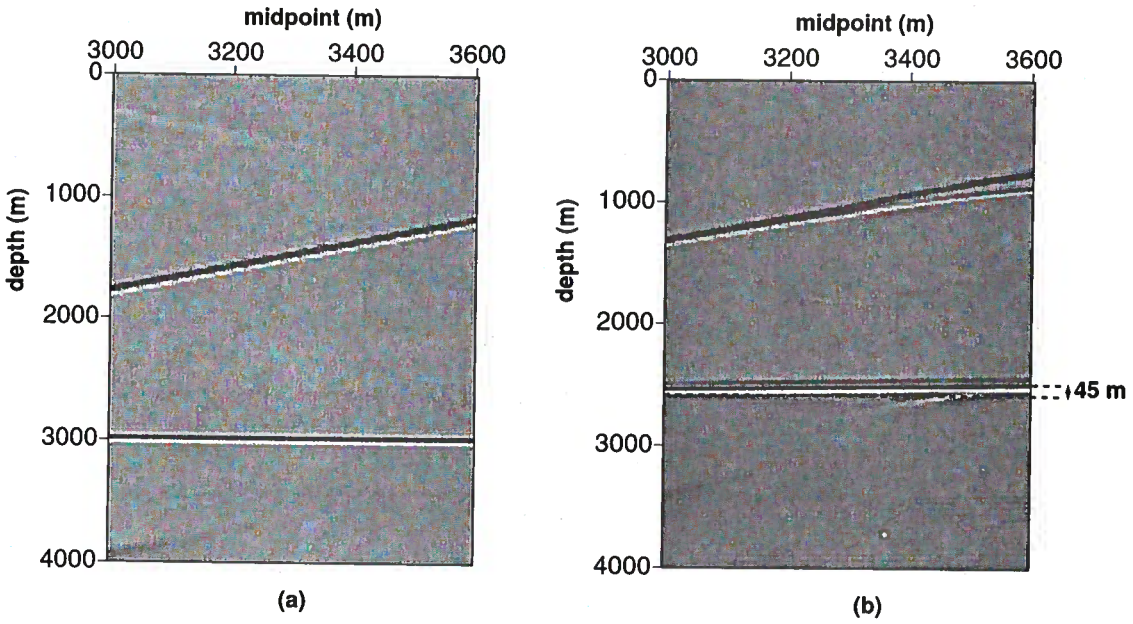

Figure 3.8. Comparison of stacked images of horizontal and dipping (45°) reflectors: (a) for the correct medium parameters ($V_{P0} = 2000$ m/s, $k_z = 0.6$/s, $k_x = 0.2$/s, $\epsilon = 0.3$ and $\delta = 0.1$) and (b) for an incorrect value of $k_x = 0.1$ s^{-1} instead of $k_x = 0.2$ s^{-1} ($V_{P0} = 2000$ m/s, $k_z = 0.6$s^{-1}, $k_x = 0.1$s^{-1}, $\epsilon = 0.0$, and $\delta = 0.1$).

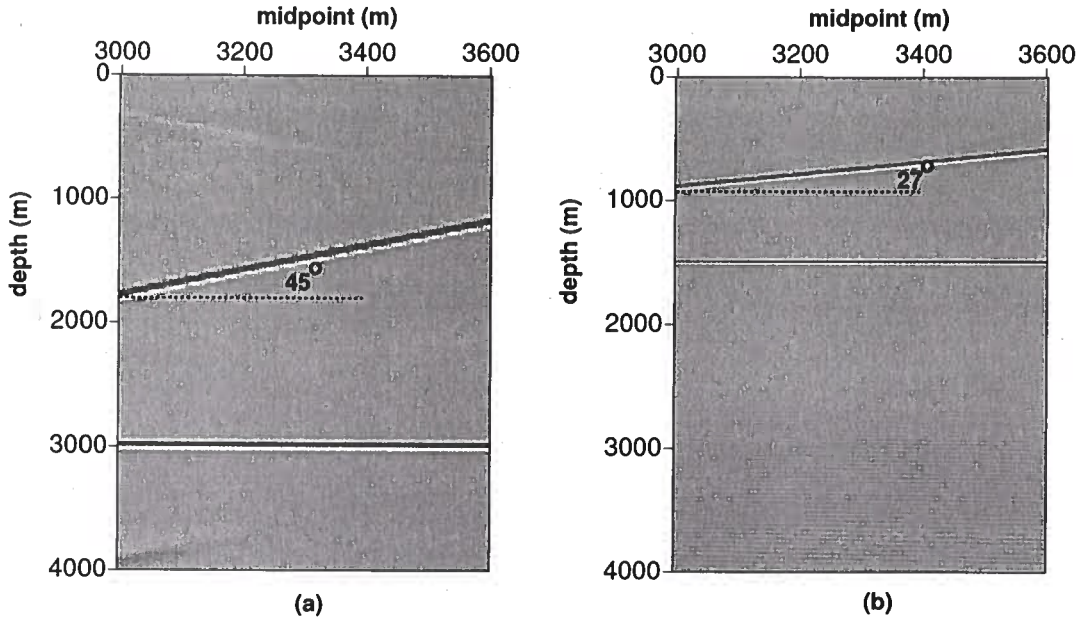

Figure 3.9. Same as Figure 3.8, but section (b) was obtained for the correct $V_{\rm nmo}$, k_z, $\hat{k}_x$ and η, but $V_{P0,M} = \frac{1}{2}V_{P0,T}$ ($V_{P0} = 1000$ m/s, $k_z = 0.6$/s, $k_x = 0.1$/s, $\epsilon = 2.7$, and $\delta = 1.9$). Because $V_{\rm nmo}$, k_z, $\hat{k}_x$ and η are correct, but $V_{P0,M} < V_{P0,T}$, the reflectors in Figure 2.10b are well focused, but imaged at smaller depths. Abnormally large values of ϵ and δ were chosen intentionally to show that the conditions outlined in the text are independent of the strength of anisotropy.

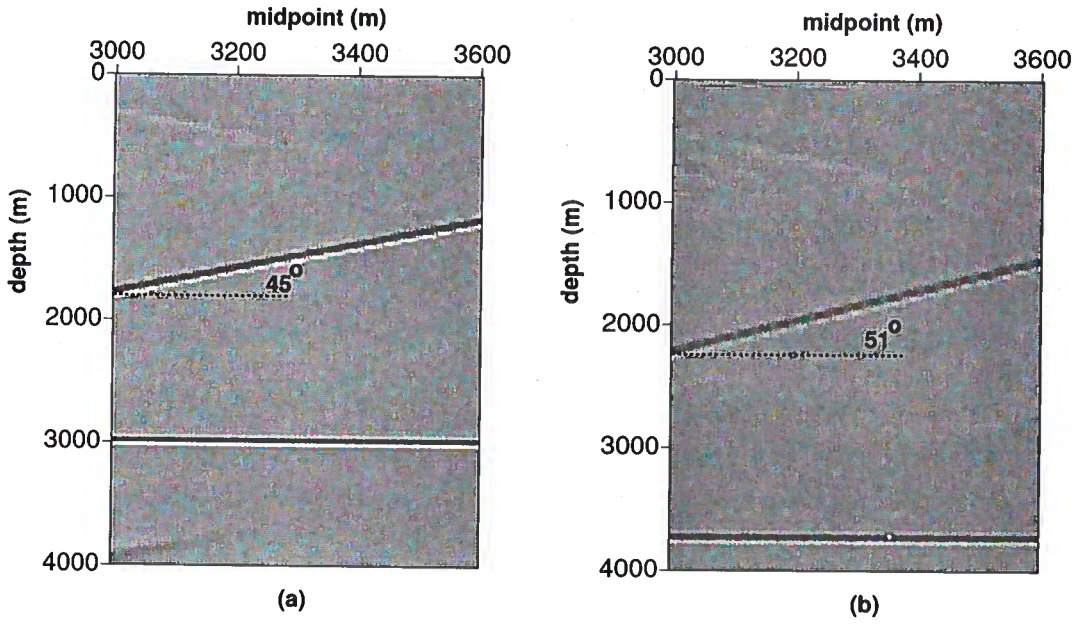

Figure 3.10. Same as Figure 3.9, but section (b) was obtained for $V_{P0,M} > V_{P0,T}$. (V_{P0} = 2500 m/s, $k_z = 0.6$/s, $k_x = 0.25$/s, $\epsilon = 0.01$, and $\delta = -0.12$). Because V_{nmo}, k_z, $\hat{k}_x$ and η are correct, but $V_{P0,M} > V_{P0,T}$, the reflectors in Figure 3.10b are well focused, but imaged at larger depths.

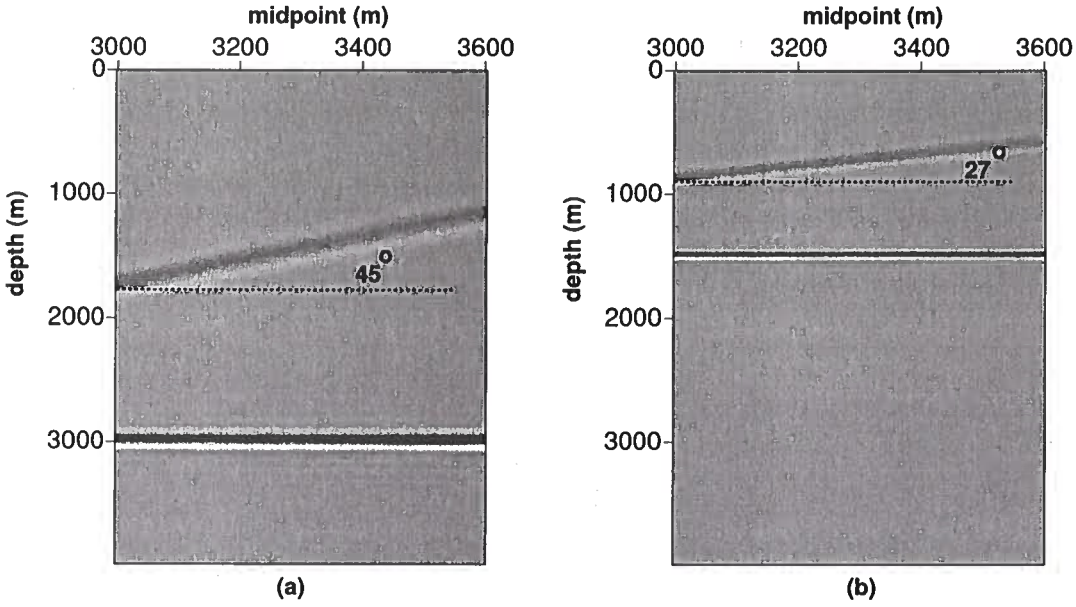

Figure 3.11. Comparison of stacked images of horizontal and dipping (45°) reflectors for large heterogeneity: (a) for the correct medium parameters ($V_{P0} = 2000$ m/s, $k_z = 1.0$/s, $k_x = 1.0$/s, $\epsilon = 0.3$ and $\delta = 0.1$) and (b) for correct V_{nmo}, k_z, $\hat{k}_x$ and η, but $V_{P0,M} = \frac{1}{2}V_{P0,T}$ ($V_{P0,M} = 1000$ m/s, $k_{z,M} = 1.0$/s, $k_{x,M} = 0.5$/s, $\epsilon_M = 2.7$, and $\delta_M = 1.9$). Abnormally large values of ϵ, δ, and k_x were chosen intentionally to show that the conditions are valid even for large anisotropy and heterogeneity.

This happens for two reasons: (1) the value of k_x does not govern the horizontal velocity $[V_{P90}(x,t_0)]$, which is unaffected by an error in V_{P0} when $V_{\rm nmo}(x,t_0)$ and η are correct $[V_{P90}(x,t_0) = V_{\rm nmo}(x,t_0)\sqrt{1+2\eta}]$, and (2) the error in $V_{P0}(x=0,z=0)$ is compensated by the error in k_x, in a way such that the ratio $\frac{V_{P0}(x=0,z=0)}{k_x}$ is not influenced by the value of V_{P0}. Therefore, the error in $V_{P0}(x,z=0)$ becomes independent of the midpoint coordinates, x, and no laterally variable depth shifts are visible. Figures 3.9b and 3.11 also demonstrate that the conditions that need to be satisfied to flatten events in factorized $v(x,z)$ media are independent of the strength of anisotropy and heterogeneity.

3.3 Parameter estimation in a factorized VTI layer

Here, I use the results discussed above to evaluate the feasibility of estimating the parameters of a factorized VTI layer from P-wave reflection data. By replacing the actual factorized $v(x,z)$ model with narrow vertical strips of factorized $v(z)$ media, I demonstrated that the moveout of a single horizontal event in an image gather is governed by the effective values of the NMO velocity and the parameter η:

$$v^2_{\rm nmo}(x,t_0) = V^2(x)(1+2\delta)\,\frac{e^{k_z t_0}-1}{k_z\,t_0}\,, \tag{3.4}$$

$$\hat{\eta}(x,t_0) = \frac{1}{8}\left\{\frac{(1+8\eta)\,(e^{2k_z\,t_0}-1)\,k_z\,t_0}{2(e^{k_z t_0}-1)^2} - 1\right\}; \tag{3.5}$$

$V_{P0}(x) \equiv V_{P0} + k_x\,x$ is the vertical P-wave velocity at the surface, and $t_0 \equiv t_0(x,z)$ is the zero-offset time at location x from a horizontal reflector at depth z.

If long-offset data needed to constrain $\hat{\eta}$ (Grechka and Tsvankin, 1998) have been acquired, moveout analysis of a single event can yield estimates of both $v_{\rm nmo}(x,t_0)$ and $\hat{\eta}(x,t_0)$. Next, suppose that P-wave traveltimes from two horizontal reflectors sufficiently separated in depth are available. Then the ratio of the NMO velocities for these two events ($v_{\rm nmo,1}$ and $v_{\rm nmo,2}$) can be used to find [equation (3.4)]

$$\frac{v^2_{\rm nmo,1}(x,t_{0,1})}{v^2_{\rm nmo,2}(x,t_{0,2})} = \frac{t_{0,2}\,(e^{k_z\,t_{0,1}}-1)}{t_{0,1}\,(e^{k_z\,t_{0,2}}-1)}\,, \tag{3.6}$$

where $t_{0,1}$ and $t_{0,2}$ are the zero-offset times for the two events. According to equation (3.6), conventional hyperbolic moveout analysis of two horizontal events located in the same factorized block can provide an estimate of the vertical gradient k_z. Knowledge of k_z and the zero-offset time t_0 is sufficient for obtaining the anellipticity parameter η from equation (3.5) applied to one or both reflection events. The remaining two key quantities, $V_{\rm nmo} = V_{P0}\sqrt{1+2\delta}$ and $\hat{k}_x = k_x\sqrt{1+2\delta}$, can then be computed from equation (3.4), if the effective NMO velocities are determined at two or more locations x.

I conclude that the moveout of horizontal events at two different depths and two image locations can provide enough information to estimate the parameters $V_{\rm nmo}$, k_z, $\hat{k}_x$, and η. For the special case of a factorized $v(z)$ medium with a constant vertical gradient

k_z, the moveouts of two horizontal events at a single image location can be inverted for the parameters V_{nmo}, k_z, and η.

Reflection moveout of dipping events in factorized $v(x,z)$ VTI media is controlled by the same parameters (V_{nmo}, k_z, $\hat{k}_x$, and η) as that of horizontal events. Most importantly, NMO velocity of events dipping at 25-30° or more is highly sensitive to the parameter η (Alkhalifah and Tsvankin, 1995; Tsvankin, 2001), whereas the inversion of nonhyperbolic moveout from horizontal reflectors for η is less stable (Grechka and Tsvankin, 1998b). Therefore, the inclusion of dipping events in velocity analysis is helpful in obtaining accurate estimates of η; also, dip-dependent reflection moveout provides additional information about the parameters V_{nmo}, k_z, and $\hat{k}_x$.

Still, even if both horizontal and dipping events are available, the parameters V_{P0}, k_x, ϵ, and δ remain unconstrained by P-wave reflection traveltimes. In particular, the vertical velocity V_{P0} is needed to define the depth scale of the VTI model in the migration of P-wave data. Hence, to build an anisotropic model for depth imaging, at least one medium parameter must be specified *a priori*. Unless specified otherwise the velocity V_{P0} in the synthetic data examples discussed in subsequent chapters is assumed known at some location at the top of each factorized layer. Given this information about V_{P0}, we can use velocity analysis of P-wave data to estimate the parameters k_z, k_x, ϵ, and δ.

3.4 3-D data

3-D traveltime signatures for P-waves in homogeneous VTI media (Grechka and Tsvankin, 1998a) are also controlled by V_{nmo} and η. Therefore, the analysis described earlier in this chapter can be readily extended to 3-D.

As before, if we assume that the factorized $v(x,y,z)$ medium, which is the 3-D equivalent of the factorized $v(x,z)$ medium, is composed of narrow vertical columns of factorized $v(z)$ media, then image gathers in $v(x,y,z)$ media will be flat if $v_{\text{nmo},M}(x,y,t_0) = v_{\text{nmo},T}(x,y,t_0)$ and $\hat{\eta}_M(x,y,t_0) = \hat{\eta}_T(x,y,t_0)$ not only for all vertical times t_0, but also for all coordinates x and y. These conditions are satisfied only if $k_{z,M} = k_{z,T}$, $\eta_M = \eta_T$, and $V_{P0,M}(x,y)\sqrt{1+2\delta_M} = V_{P0,T}(x,y)\sqrt{1+2\delta_T}$, where $V_{P0}(x,y) = V_{P0} + k_x x + k_y y$ and k_y is the lateral velocity gradient along the y-direction. Setting $V_{P0,M}(x,y)\sqrt{1+2\delta_M} = V_{P0,T}(x,y)\sqrt{1+2\delta_T}$ for all values of x and y implies $V_{\text{nmo},M} = V_{\text{nmo},T}$, $k_{x,M}\sqrt{1+2\delta_M} = k_{x,T}\sqrt{1+2\delta_T}$, and $k_{y,M}\sqrt{1+2\delta_M} = k_{y,T}\sqrt{1+2\delta_T}$.

Therefore, I expect that the conditions that flatten all image gathers in 3-D factorized $v(x,y,z)$ media are

1. $V_{\text{nmo},M} = V_{\text{nmo},T}$,
2. $k_{z,M} = k_{z,T}$,
3. $\eta_M = \eta_T$,
4. $k_{x,M}\sqrt{1+2\delta_M} = k_{x,T}\sqrt{1+2\delta_T}$,
5. $k_{y,M}\sqrt{1+2\delta_M} = k_{y,T}\sqrt{1+2\delta_T}$,

and, as in the 2-D case, parameters ϵ, δ, k_x, and k_y may be estimated uniquely if the vertical velocity V_{P0} is known at a single point.

Chapter 4

Migration velocity analysis: The algorithm and tests for a single layer

4.1 Algorithm for migration velocity analysis

Inversion of seismic data is a nonlinear problem that can be solved through an iterative application of migration and velocity updating. Migration creates an image of the subsurface for trial values of the medium parameters, and then velocity analysis is used to update the model for the next run of the migration code. This iterative procedure, conventionally called *migration velocity analysis* (MVA), is continued until a certain criterion (e.g., small residual moveout of events in image gathers) is satisfied.

Here, I apply anisotropic prestack depth migration (the migration algorithm is described in detail in chapter 1) and tomographic velocity update to P-wave data acquired over the subsurface composed of factorized $v(x,z)$ VTI blocks. The iterations are stopped when the residual moveout for at least two reflectors in each factorized block is close to zero (i.e., the migrated depth stays the same to within a specified fraction of the wavelength for different offsets). The overall organization of my MVA algorithm is similar to that developed by Liu (1997) for isotropic media, but the VTI model is characterized, for P-waves, by two additional parameters – ϵ and δ.

The tomographic update of the medium parameters is based entirely on the residual moveout of events in image gathers. In chapter 2 I showed that for horizontal reflectors embedded in a weakly anisotropic homogeneous VTI medium the migrated depth z_M in image gathers can be written as [equation (2.4)]:

$$z_M^2(h) \approx z_M^2(0) + h^2 V_{P0,M}^2 \left(\frac{1}{V_{\mathrm{nmo},T}^2} - \frac{1}{V_{\mathrm{nmo},M}^2} \right) + \frac{2h^4}{h^2 + z_T^2} \left(\eta_M \frac{V_{\mathrm{nmo},T}^2}{V_{\mathrm{nmo},M}^2} - \eta_T \frac{V_{\mathrm{nmo},M}^2}{V_{\mathrm{nmo},T}^2} \right), \quad (4.1)$$

where the subscripts T and M denote the true and migration medium parameters, respectively, h is the half-offset, and z_T is the true zero-offset depth of the reflector. Equation (4.1) is nonhyperbolic and governed by two independent parameters – V_{nmo} and η. The NMO velocity V_{nmo} controls the hyperbolic (described by the h^2–term) part of the moveout curve and also contributes to the nonhyperbolic (h^4) term, while η influences nonhyperbolic moveout only. A similar closed-form expression is not available for dipping reflectors, but both

the hyperbolic and nonhyperbolic portions of the residual moveout curve for dipping events also depend on V_{nmo} and η.

As discussed in the previous two chapters, the residual moveout of P-waves in factorized $v(x,z)$ VTI media is a function of the parameters V_{nmo}, k_z, $\hat{k}_x$, and η. Although it is difficult to express the migrated depth z_M in laterally heterogeneous media analytically in terms of these parameters, the residual moveout equation can be cast in a form similar to that in equation (4.1):

$$z_M^2(h) \approx z_M^2(0) + \mathrm{A}\, h^2 + \mathrm{B}\, \frac{2h^4}{h^2 + z_M^2(0)}. \tag{4.2}$$

A and B are dimensionless constants that describe the hyperbolic and nonhyperbolic portions of the moveout curve, respectively. Numerical tests (see below) confirm that the functional form in equation (4.2) with fitted coefficients A and B provides a good approximation for P-wave moveout in long-spread image gathers.

To apply equation (4.2) in velocity analysis, I first pick an approximate value of the zero-offset reflector depth $z_M(0)$ on the migrated stacked section. The parameters A and B are obtained by a 2-D semblance scan on image gathers at each migrated zero-offset depth point. The best-fit combination of A and B that maximizes the semblance value is substituted into equation (4.2) to describe the residual moveout. It should be emphasized that the coefficients A and B in my algorithm are not directly inverted for the parameters V_{nmo}, k_z, $\hat{k}_x$, and η. Rather, the only role of A and B is in providing an adequate functional approximation for the residual moveout.

After estimating the residual moveout in image gathers, I update the N-element parameter vector $\boldsymbol{\lambda}$ using the algorithm described in Appendix C. The update $\boldsymbol{\Delta\lambda}$ of the parameter vector is obtained by solving the system of linear equations,

$$\boldsymbol{A}^T \boldsymbol{A}\, \boldsymbol{\Delta\lambda} = \boldsymbol{A}^T \boldsymbol{b}. \tag{4.3}$$

Here $\boldsymbol{A}$ is a matrix with $M \cdot P$ rows (M is the number of offsets and P is the total number of image gathers used in the velocity analysis) and N columns that includes the derivatives of the migrated depth with respect to the medium parameters. The superscript T denotes the transpose, and $\boldsymbol{b}$ contains the migrated depths that define the residual moveout. The full definitions of the matrix $\boldsymbol{A}$ and vector $\boldsymbol{b}$ are given in Appendix C.

For all examples described below, each iteration of the MVA consists of the following four steps:
(1) prestack depth migration with a given estimate of the medium parameters;
(2) picking along two reflectors in each VTI block to delineate the reflector shapes;
(3) semblance scanning using equation (4.2) to estimate A and B for image points along each reflector;
(4) application of equation (4.3) to update the medium parameters in such a way that the variance of the migrated depths as a function of offset is minimized (see Appendix C for more details about the minimization procedure).

Steps 1–4 are repeated until the magnitude of residual moveout of events in image gathers becomes sufficiently small.

4.2 Example with a single factorized layer

First, I consider two irregular reflectors embedded in a factorized $v(x,z)$ VTI medium with $k_z > k_x > 0$ and a positive value of η typical for shale formations (Figure 4.1). For the first application of prestack depth migration, I choose a homogeneous, isotropic medium ($V_{P0} = 2600$ m/s, $k_z = k_x = \epsilon = \delta = 0$) as the initial velocity model. The migrated stacked image in Figure 4.2a is clearly inferior to the true image in Figure 4.1. I start the velocity-updating process by manually picking along both imaged reflectors to outline their shapes. Then equation (4.2) is used to compute two-parameter semblance scans for each reflector and evaluate the residual moveout in the image gathers.

One such semblance scan computed for the shallow reflector at the surface coordinate 3 km is displayed in Figure 4.2b. The values of A and B that correspond to the maximum semblance coefficient in Figure 4.2b provide an accurate description of residual moveout at this location. Although a certain degree of trade-off exists between A and B, any pair of values inside the innermost semblance contour gives almost the same variance of the migrated depths. Note that the interplay between A and B is similar to that between the NMO velocity and parameter η in the inversion of P-wave nonhyperbolic reflection moveout (Grechka and Tsvankin, 1998b; Tsvankin, 2001).

For purposes of velocity analysis, I use the image gathers at 12 equally spaced surface locations between 3 km and 4.2 km. The maximum offset-to-depth ratio for the selected image gathers at the shallow reflector is close to two, which is marginally suitable for estimating the parameter η. Tighter constraints on η are provided by the NMO velocities of reflections from the dipping segments of the shallow reflector (the dips exceed 30° in the middle of the section).

After the residual moveout has been evaluated, I fix the vertical velocity $V_{P0}(x = 3000\,\text{m}, z = 0) = 2600$ m/s at the correct value and update the parameters k_z, k_x, ϵ, and δ using equation (4.3). The stacked images after four (Figure 4.3a) and eight (Figure 4.3b) iterations illustrate the improvements in the focusing and positioning of both reflectors during the velocity update. The magnitude of the residual moveout for both reflectors decreases as the model parameters converge toward their actual values (Figure 4.4). The velocity-updating procedure is stopped after eight iterations because events in all analyzed image gathers are practically flat.

The inverted model parameters are close to the correct values: $k_z = 0.61 \pm 0.02$ s^{-1}, $k_x = 0.2 \pm 0.0$ s^{-1}, $\epsilon = 0.11 \pm 0.01$, and $\delta = -0.11 \pm 0.01$. The error bars were computed by assuming a standard deviation of ± 5 m in picking migrated depths on the selected image gathers and substituting this picking error into equation (4.3) to find the corresponding deviations of the model parameters near the actual solution.

The accurate results of the above test were obtained with the correct value of the vertical velocity at a given point on the surface of the factorized layer. Next, I apply the MVA method with an erroneous value of $V_{P0}(x = 3\,\text{km}, z = 0) = 2000\,\text{m/s}$, which is 23% smaller than the true velocity (2600 m/s). The stacked images of both reflectors obtained after the velocity analysis (Figure 4.5a) are well focused, which indicates that the image gathers have been flattened. Indeed, although the estimated medium parameters listed in

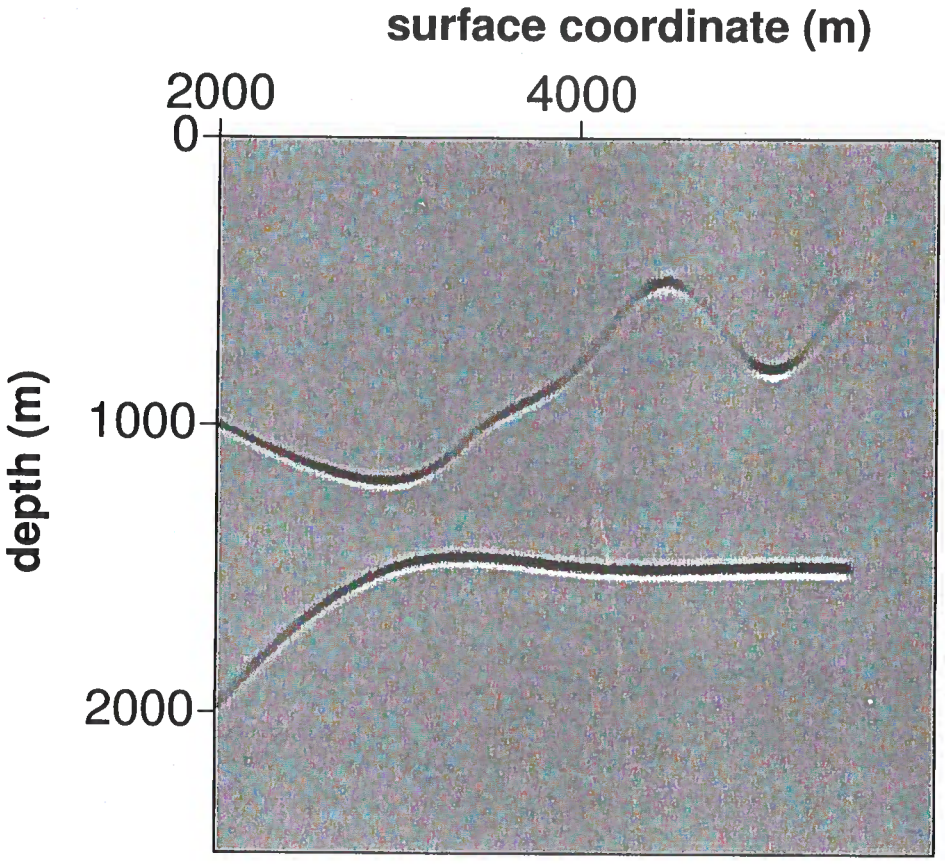

Figure 4.1. True image of two reflectors embedded in a factorized $v(x,z)$ VTI medium with the parameters $V_{P0}(x = 3\,\text{km}, z = 0) = 2600$ m/s, $k_z = 0.6$ s^{-1}, $k_x = 0.2$ s^{-1}, $\epsilon = 0.1$, and $\delta = -0.1$. The corresponding effective parameters are $V_{\text{nmo}}(x = 3\,\text{km}, z = 0) = 2326$ m/s, $k_z = 0.6$ s^{-1}, $\hat{k}_x = 0.18$ s^{-1}, and $\eta = 0.25$.

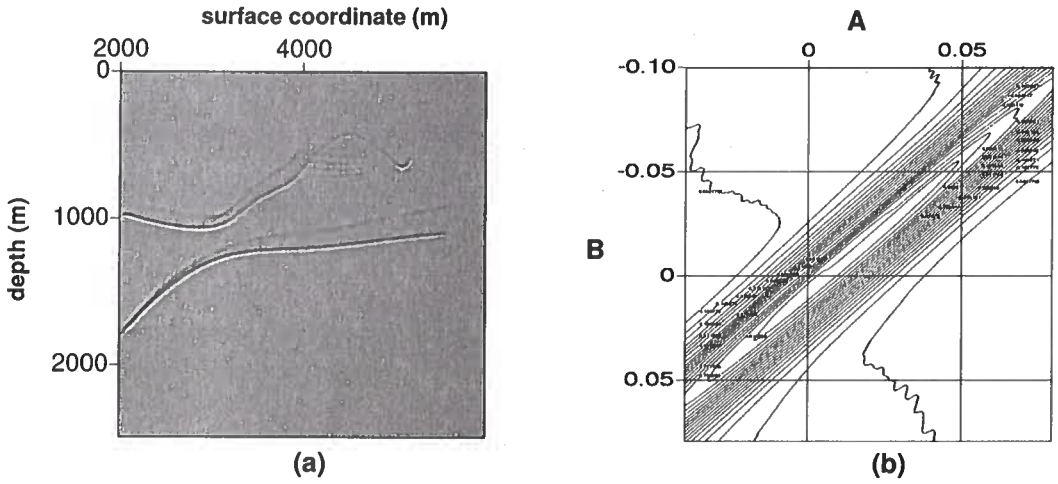

Figure 4.2. (a) Image of the model from Figure 4.1 obtained using a homogeneous isotropic velocity field with $V_{P0} = 2600$ m/s. (b) Semblance contour plot computed from equation (4.2) for the shallow reflector at the surface location 3 km.

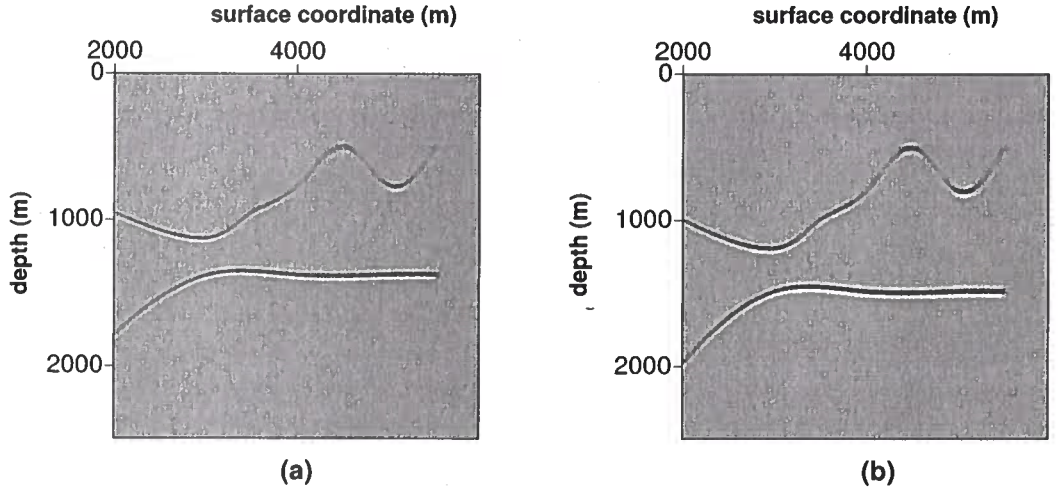

Figure 4.3. Stacked image after (a) four iterations; (b) eight iterations.

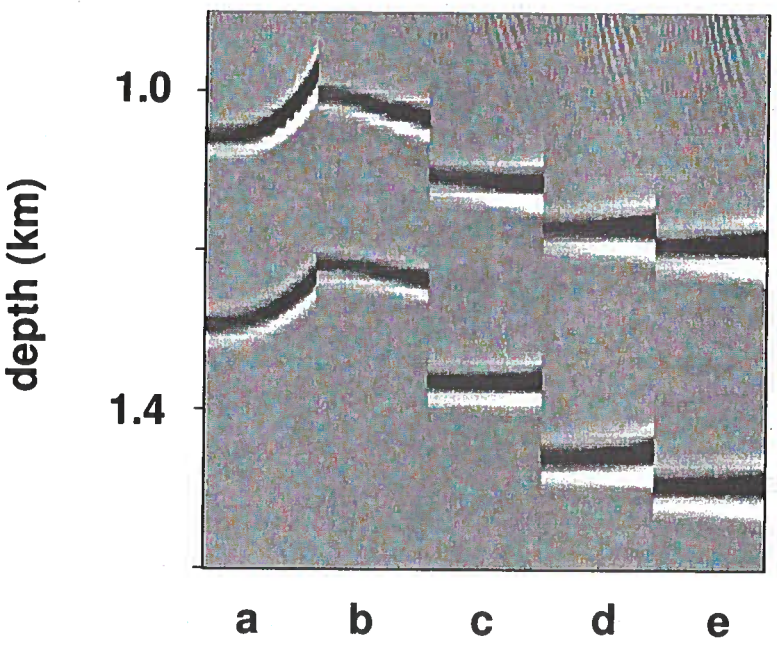

Figure 4.4. Residual moveout in image gathers for both reflectors at the surface location 3 km: (a) for the initial model; (b) after two, (c) four, (d) six, and (e) eight iterations. The residual moveout is minimized during the velocity-updating process.

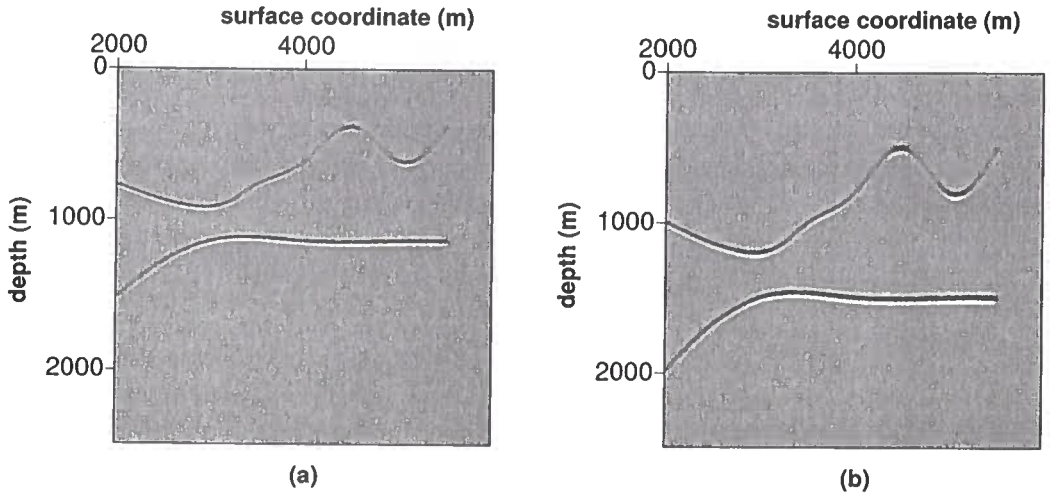

Figure 4.5. (a) Stacked image obtained after velocity analysis with the wrong value of the vertical velocity $V_{P0}(x = 3\,\text{km}, z = 0) = 2000$ m/s. The estimated medium parameters are $k_z = 0.58\ ^{-1}$, $k_x = 0.15\ \text{s}^{-1}$, $\epsilon = 0.51$, $\delta = 0.17$. (b) Stacked image for the correct medium parameters (Figure 4.1). Since V_{P0} in section (a) is smaller than the true value, both reflectors are shifted up with respect to their correct positions in section (b).

the caption of Figure 4.5 are distorted, the effective parameters responsible for the residual moveout are close to their actual values: $V_{\text{nmo}}(x = 3\,\text{km}, z = 0) = 2315$ m/s, $k_z = 0.58\ \text{s}^{-1}$, $\hat{k}_x = 0.17\ \text{s}^{-1}$, and $\eta = 0.25$.

This result corroborates the analysis of residual moveout in chapters 2 and 3 and confirms that my algorithm converges toward the correct parameters V_{nmo}, k_z, $\hat{k}_x$, and η, even if the vertical velocity V_{P0} on the surface of the layer is poorly known. Since V_{P0} assumed in the velocity analysis is too low, however, both reflectors in Figure 4.5a are imaged at depths that are about 23% smaller than the actual ones in Figure 4.5b. The depth distortion also leads to the rotation of the dipping segments of the reflecting interfaces, which is discussed in more detail below.

4.3 MVA in the presence of noise

To evaluate the influence of noise on the estimation of the medium parameters and the quality of imaging, I added Gaussian noise to the data set from Figure 4.1. The signal-to-noise ratio, measured as the ratio of the peak amplitude of the signal to the root-mean-square (rms) amplitude of the background noise, is about 1.5, and the frequency bands of the noise and signal are identical (Figure 4.6a). The estimates of the medium parameters obtained after the migration velocity analysis with the correct value of V_{P0} at the surface location 3 km are as follows: $k_z = 0.56 \pm 0.04\ \text{s}^{-1}$, $k_x = 0.2 \pm 0.0\ \text{s}^{-1}$, $\epsilon = 0.12 \pm 0.02$, and

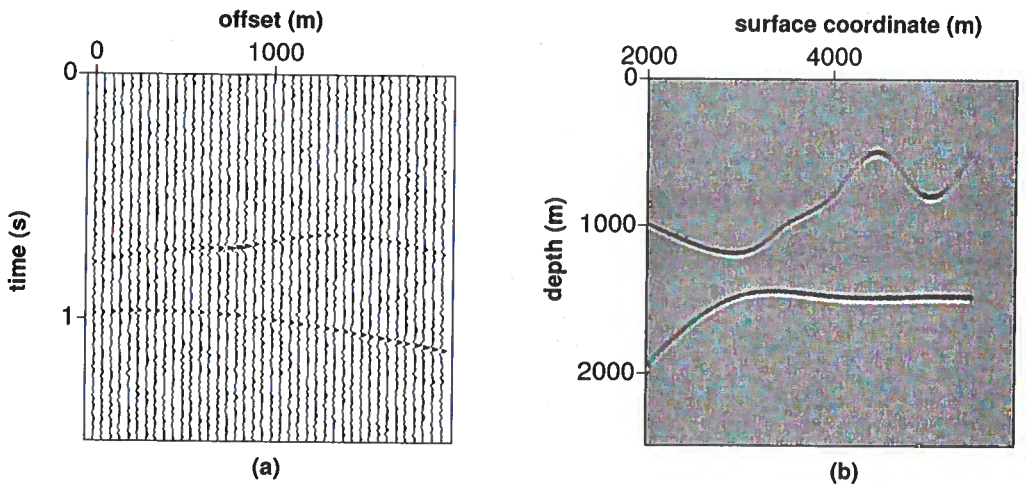

Figure 4.6. Influence of noise on the velocity analysis and migration. (a) A shot gather from the dataset in Figure 4.1 after the addition of Gaussian noise; the signal-to-noise ratio is 1.5. (b) The image obtained for the noisy dataset.

$\delta = -0.09 \pm 0.02$. The error bars were computed in the same way as those for the noise-free synthetic example above (Figure 4.3), but the depth-picking error for all offsets and image locations was assumed to be 15 m instead of 5 m. Clearly, the noise contamination did not cause measurable errors in the medium parameters or noticeable distortions in the stacked image (Figure 4.6b).

Even for the much more severely contaminated data set in Figure 4.7, the inverted medium parameters are close to the actual values: $k_z = 0.52 \pm 0.07$ s^{-1}, $k_x = 0.2 \pm 0.01$ s^{-1}, $\epsilon = 0.13 \pm 0.03$, and $\delta = -0.07 \pm 0.03$, Here the error bars were computed under the assumption that the noise increased the depth-picking error to 20 m. (Since the dominant wavelength in this example was about 80 m, picking errors are unlikely to exceed 20 m, even for a substantial level of noise.) Also, despite the low signal-to-noise ratio, the migrated stacked section in Figure 4.7b has a sufficiently high quality, comparable to that of the true image in Figure 4.1.

I conclude that the migration velocity analysis employed here gives reliable estimates of the anisotropic parameters and velocity gradients in the presence of random noise. One aiding factor is that the MVA operates on migrated data, which have a higher signal-to-noise ratio than the original records because of partial stacking applied to the data during the migration step. The semblance (coherency) operator used to evaluate the residual moveout on image gathers also contributes to the robustness of the parameter estimation by suppressing remaining random noise in the migrated data.

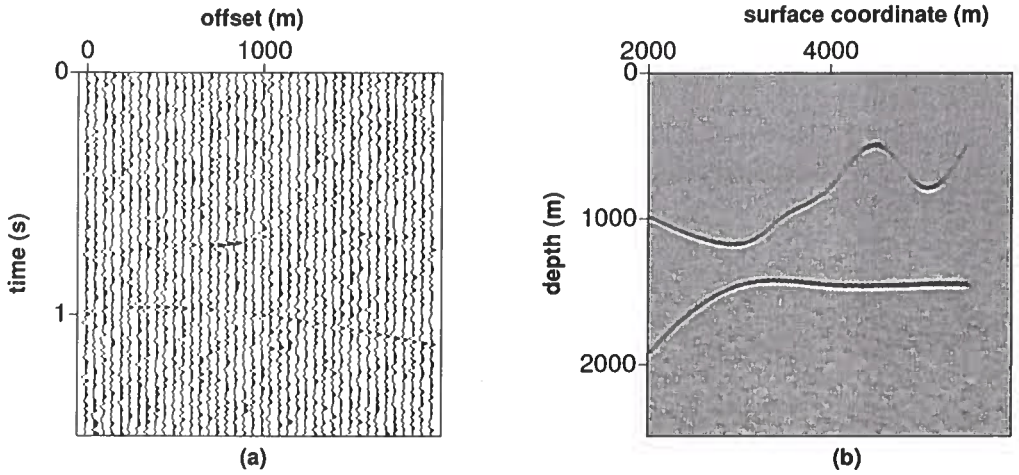

Figure 4.7. Influence of noise on the velocity analysis and migration. (a) The same shot gather as in Figure 4.6, but with a more severe noise contamination (signal-to-noise ratio is 1). (b) The image obtained for the noisy dataset.

4.4 Sensitivity Study

The above results demonstrate that, in principle, the residual moveout from two reflectors in a factorized layer is sufficient to estimate the four key parameters V_{nmo}, k_z, $\hat{k}_x$, and η. This section is devoted to an important practical issue related to the implementation of my algorithm. By performing a series of numerical tests, I establish the minimum depth separation between the two reflectors needed for stable parameter estimation.

Consider two horizontal reflectors embedded in the factorized $v(x,z)$ medium with the parameters listed in the caption of Figure 4.8. The depth of the shallow reflector is fixed at 1000 m, while the depth of the second reflector varies from 1050 m to 2000 m. Figures 4.8–4.9 illustrate the dependence of the error in the estimated parameters k_z, k_x, ϵ, and δ on the distance between the reflectors. The errors in the parameters were computed from equation (4.3) assuming that the error in picking the migrated depths is ± 5 m. The velocity analysis operated with the residual moveout on 12 image gathers (with 20 offsets each) whose horizontal coordinates span a distance of 1200 m. For all tests, the vertical velocity at one location on the surface was held at the correct value.

For the parameters k_z, ϵ and δ, the dependence of the estimated error on the distance d between the reflectors has a similar character (Figures 4.8, 4.10, and 4.11). The error initially decreases rapidly with increasing d and then becomes almost constant as d approaches 500 m. For a maximum offset-to-depth ratio (at the shallow reflector) of two, the error curves flatten out for $d \approx 250$ m, which is equal to 1/5 of the depth of the bottom reflector. If the maximum offset-to-depth ratio is 1.5, the curve flattens out for a larger

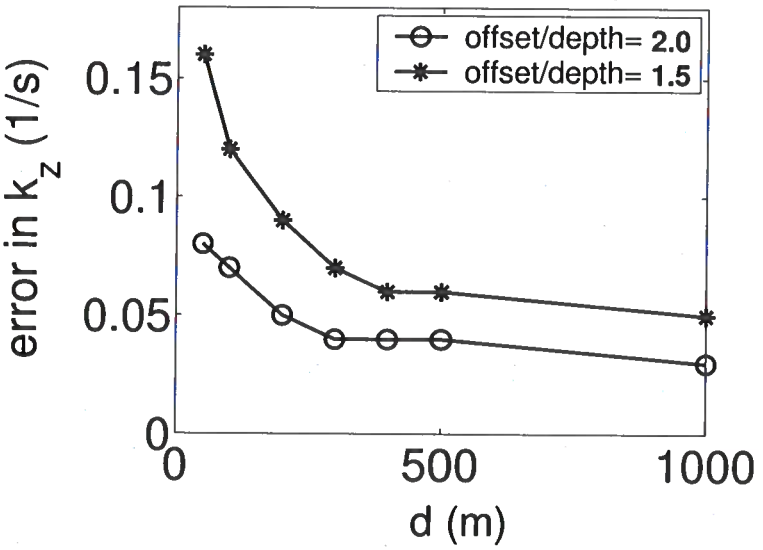

Figure 4.8. Influence of the vertical distance d between the two horizontal reflectors used in the velocity analysis on the absolute error in the vertical gradient k_z. The depth of the shallow reflector is 1 km; the maximum offset is 2 km for the upper curve and 1.5 km for the lower curve. The model parameters are $V_{P0}(x = 3\,\text{km}, z = 0) = 2600$ m/s, $k_z = 0.6$ s^{-1}, $k_x = 0.2$ s^{-1}, $\epsilon = 0.2$, and $\delta = 0.1$.

depth $d \approx 350$ m ($\approx$1/4 of the depth of the bottom reflector).

This behavior of the error curves is in good agreement with the analysis of the effective NMO velocity and parameter η in chapters 2 and 3. Accurate estimation of the vertical gradient k_z, and then the NMO velocity at the surface of the factorized layer, requires a sufficiently large difference between the NMO velocities of the two events used in the velocity analysis [see equation (3.6)]. In other words, the reflectors should be sufficiently separated in depth to resolve the interval NMO velocity, which carries information about the gradient k_z. An accurate estimate of k_z makes it possible to obtain V_{nmo} at the surface and then, using the nonhyperbolic portion of the moveout curve, the parameter η. The minimum suitable vertical distance d found here is close to the minimum layer thickness conventionally assumed in interval velocity estimation based on the Dix equation.

In contrast, the error in the horizontal gradient k_x is practically insensitive to variations in the distance between the two reflectors (Figure 4.9) because the lateral spread of the coordinates of the image gathers is kept constant at 1.2 km. The influence of the maximum horizontal distance between the image gathers on the error in k_x is shown in Figure 4.12. As expected, the gradient k_x becomes better constrained with increasing lateral spread of the image gathers, with the error curve flattening out for spreads exceeding 300-400 m.

Note that the errors in all parameters reduce with increasing number of offsets in the image gathers, which can influence the sensitivity estimates. Although the results of the

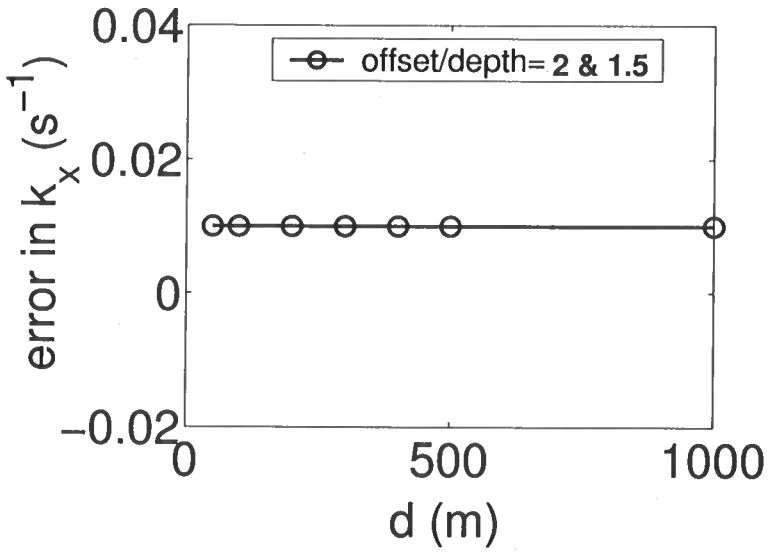

Figure 4.9. Influence of the distance between the two horizontal reflectors on the absolute error in the horizontal gradient k_x. The parameters are the same as in Figure 4.8.

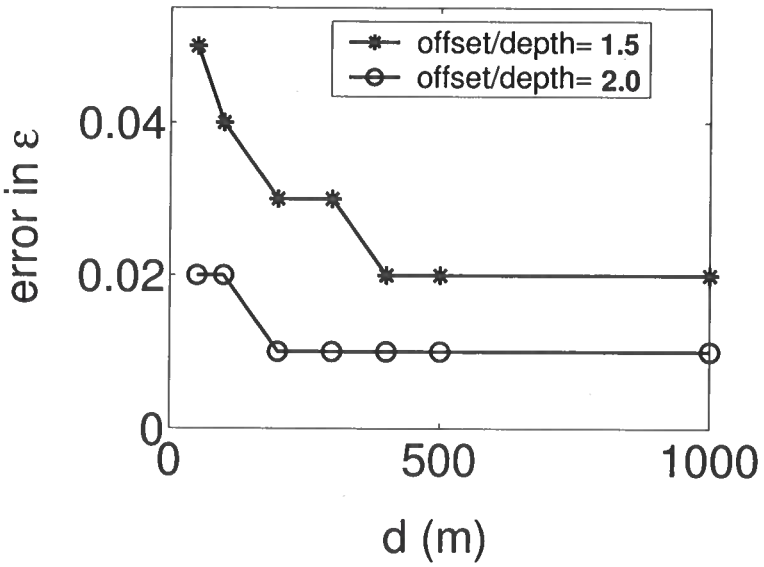

Figure 4.10. Influence of the distance between the two horizontal reflectors on the absolute error in the parameter ϵ. The parameters are the same as in Figure 4.8.

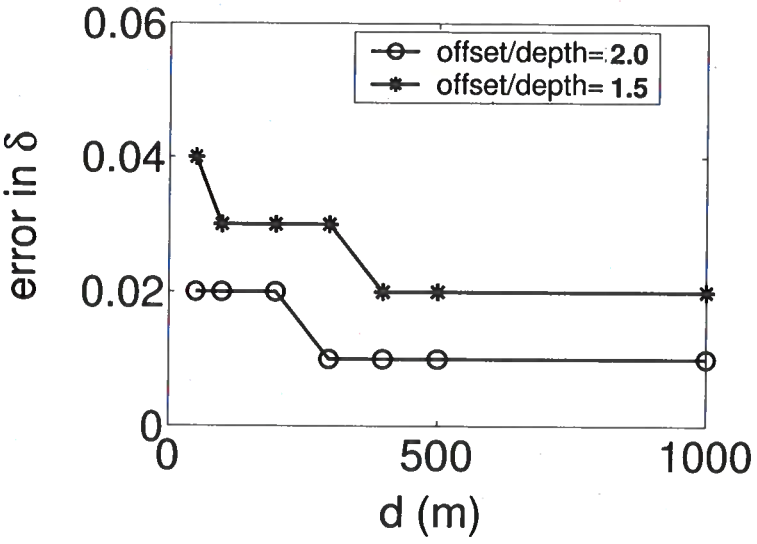

Figure 4.11. Influence of the distance between the two horizontal reflectors on the absolute error in the parameter δ. The parameters are the same as in Figure 4.8.

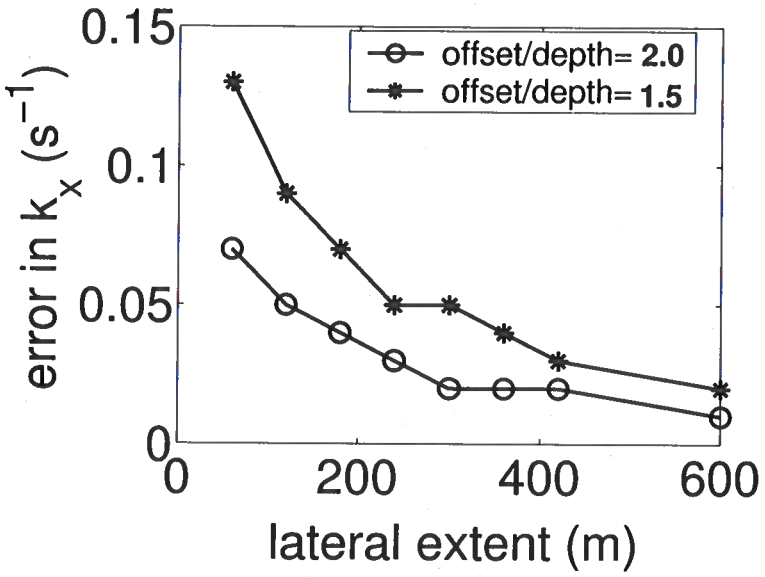

Figure 4.12. Influence of the lateral spread of the image gathers on the absolute error in k_x. The reflector depths are 1 km and 1.2 km; the other parameters are the same as in Figure 4.10. The velocity analysis is performed on 12 image gathers, each with 20 offsets.

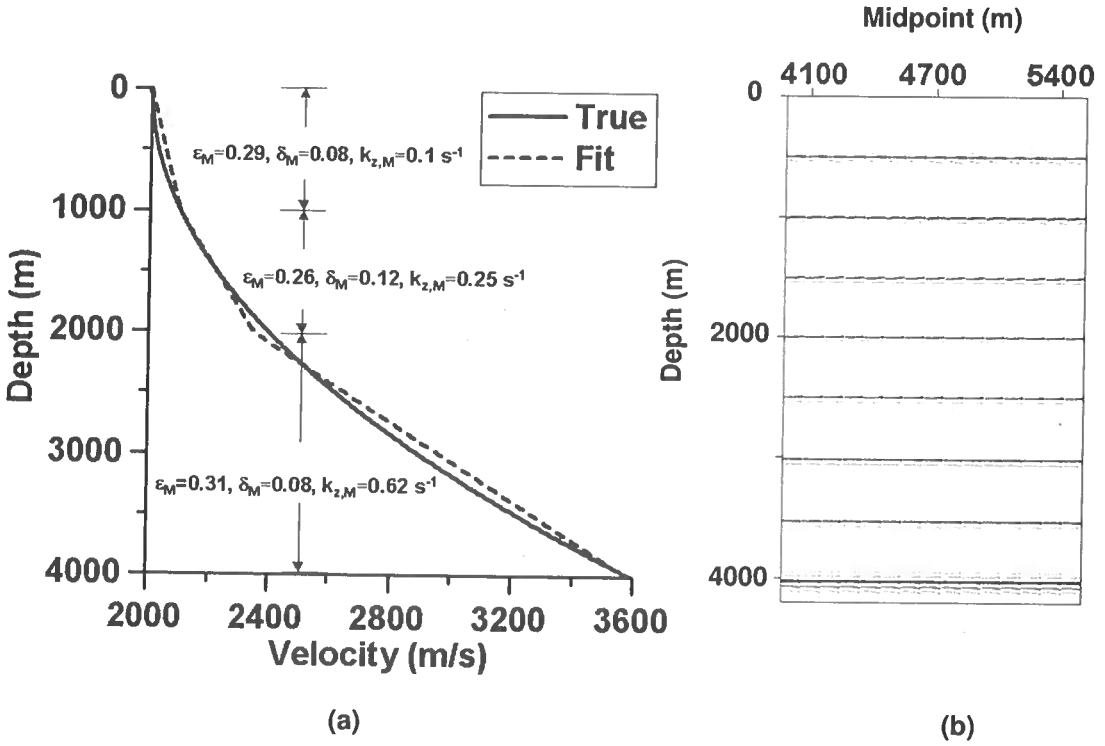

Figure 4.13. A comparison of the true (solid line) and estimated (dashed line) variation of V_{P0} after approximating the true velocity function as piecewice factorized $v(z)$ media. The true medium has a velocity variation $V_{P0}(z) = 2000 + 0.0001z^2$ m/s, $\epsilon = 0.3$, and $\delta = 0.1$. In the true medium, reflectors are spaced every 500 m and the maximum offset is equal to 4000 m. The parameters estimated using the moveout associated with all reflectors are shown in Figure 4.13a with subscripts M, and 15 image gathers obtained after prestack depth migration with the estimated parameters are shown in Figure 4.13a.

error analysis also depend on the anisotropic coefficients ϵ and δ and the velocity gradients, this dependence is not significant if the velocity update is performed with reasonable constraints on the model parameters.

4.5 Nonlinear velocity variation

If the true vertical-velocity variation is not linear, it may be well approximated by many piecewise factorized $v(x, z)$ layers or blocks. Consider a factorized medium with a nonlinear variation in vertical velocity $[V_{P0}(z) = V_{P0} + 0.0001z^2]$, and the anisotropic parameters $\epsilon = 0.3$ and $\delta = 0.1$, and suppose that eight horizontal reflectors exist at depth intervals of 500 m. Using the moveout associated with two reflectors for each estimated factorized $v(z)$ section, I reconstruct a piecewise continuous factorized $v(z)$ medium that is close to the true nonlinear velocity distribution (Figure 4.13). The accuracy of the estimated parameters is

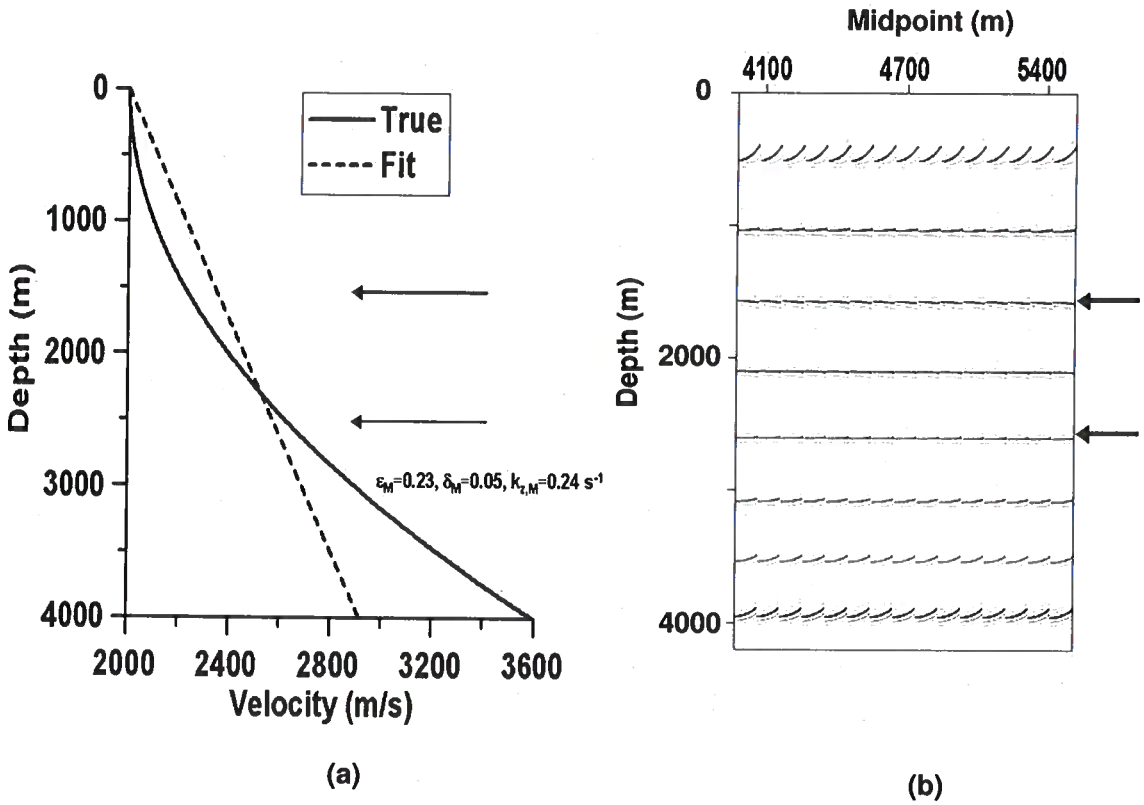

Figure 4.14. Same as Figure 4.13, but now the parameters were estimated using the moveout associated with only two reflectors at depths 1500 and 2500 m (the reflectors used for the inversion are indicated in the figures with arrows).

confirmed by the flat image gathers in Figure 4.13b. The parameters were estimated in a layer stripping mode. The vertical velocity at the top of the shallowest section was fixed at the correct value assumed to be known *a priori*, while the values at the top of the other two deeper sections were chosen so as to ensure that the vertical velocity field is continuous.

The accuracy of the approximation however, depends on whether the reflectors allow us to sample the velocity function in sufficient detail. Consider the same true medium as in Figure 4.13, but now with only two reflectors at 1500 m and 2500 m depths. In this case, only a single factorized $v(z)$ medium can be estimated (Figure 4.14a). The image gathers obtained after migration with the estimated parameters are shown in Figure 4.14b. The events associated with the reflectors at true depths 1500 and 2500 m are flat, but the events both above and below are overcorrected because the corresponding NMO velocity is too low. Therefore, although piecewise factorized $v(x, z)$ media may be used to approximate nonlinear velocity fields, a sufficient number of reflectors that are well separated in depth is required for the inversion to be accurate.

Chapter 5

Migration velocity analysis: Two synthetic examples

5.1 Test for a simple three-layer synthetic model

After having performed a series of tests for a single factorized layer, I now apply the algorithm to a three-layer model shown in Figure 5.1. Each layer contains two reflecting interfaces, as required in the method, with every second reflector serving as the boundary between layers. The first and third layers are vertically heterogeneous $[v(z)]$ and isotropic, while the second layer is a factorized, laterally heterogeneous $[v(x,z)]$ VTI medium. All interfaces are quasi-horizontal, with the largest dips (at the flanks of the syncline) 10° or less. The model is designed to represent a typical depositional environment in the Gulf of Mexico, where anisotropic shale layers (the middle layer in Figure 5.1) are often embedded between isotropic sands.

For the velocity analysis I use image gathers located along the left flank of the syncline with surface coordinates ranging from 4400 m to 5600 m; the maximum offset-to-depth ratio for the image gathers is close to two. The medium parameters are estimated in the layer-stripping mode starting at the surface. For the first (top) layer, the vertical velocity is assumed to be known at a single surface location $[V_{P0}(x = 4000, z = 0) = 1500$ m/s$]$. The chosen value of V_{P0} corresponds to that for water-bottom sediments; on land, V_{P0} at the top of the model may be estimated from near-surface velocity measurements. The iterative velocity update starts with a homogeneous isotropic model ($V_{P0} = 1500$ m/s). The parameters k_z, k_x, ϵ, and δ in the first layer, obtained from the migration velocity analysis with the correct vertical velocity $V_{P0}(x = 4000, z = 0)$, are close to the true values (Figure 5.2).

To estimate the medium parameters in the second and third layers, I need to fix the vertical velocity at a certain spatial location in each layer. Three different scenarios for choosing V_{P0} in the second and third layers are examined below.

5.1.1 V_{P0} at the top of each layer is known

Suppose a vertical borehole was drilled at the surface location 4000 m, and the vertical velocity at the top of the second and third layers was measured from sonic logs or check shots. Prestack depth migration with the estimated parameters of the first layer yields the depth of the top of the second layer at the surface location 4000 m. Using the correct value of the vertical velocity at this point $V_{P0}(x = 4000, z = 800) = 2300$ m/s, I carry

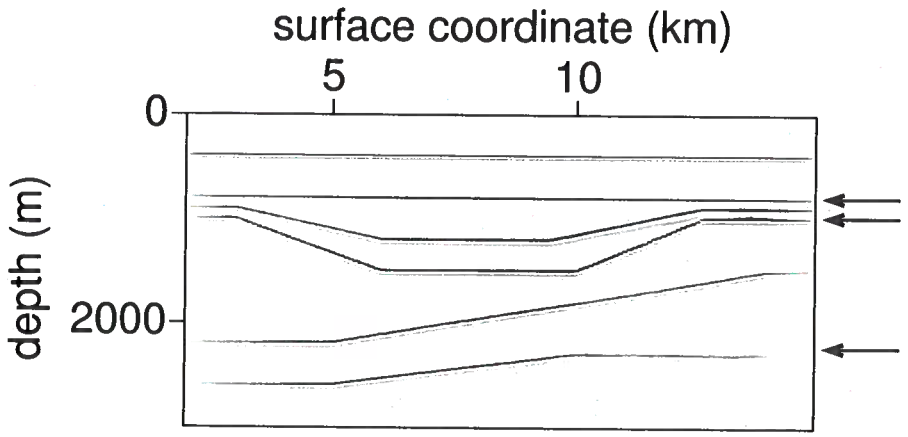

Figure 5.1. True image of a three-layer factorized medium. Every second reflector (indicated here with arrows) represents the bottom of a layer. The parameters of the first subsurface layer are $V_{P0}(x = 4000, z = 0) = 1500$ m/s, $k_z = 1.0$ s^{-1}, and $k_x = \epsilon = \delta = 0$; for the second layer, $V_{P0}(x = 4000, z = 800) = 2300$ m/s, $k_z = 0.6$ s^{-1}, $k_x = 0.1$ s^{-1}, $\epsilon = 0.1$, and $\delta = -0.1$; for the third layer, $V_{P0}(x = 4000, z = 1162) = 2718$ m/s, $k_z = 0.3$ s^{-1}, and $k_x = \epsilon = \delta = 0$.

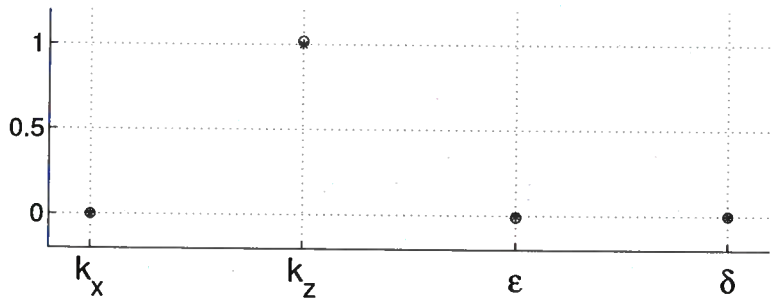

Figure 5.2. Estimated ($\circ$) and true ($\star$) parameters of the first layer obtained using the correct $V_{P0}(x = 4000, z = 0) = 1500$ m/s on the surface.

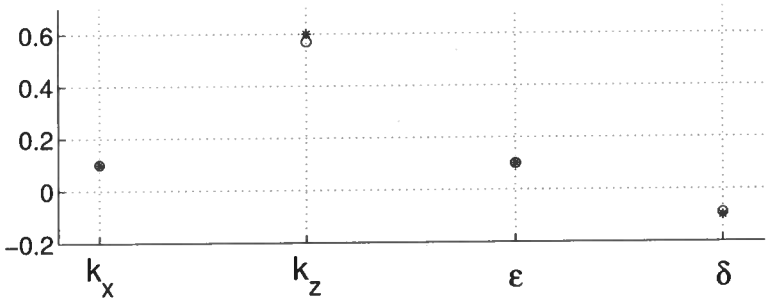

Figure 5.3. Estimated (∘) and true (⋆) parameters of the second layer obtained using the correct $V_{P0}(x = 4000, z = 800) = 2300$ m/s at the layer's top.

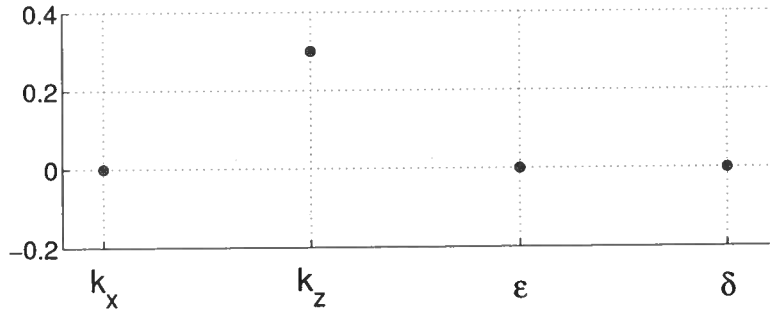

Figure 5.4. Estimated (∘) and true (⋆) parameters of the third layer obtained using the correct $V_{P0}(x = 4000, z = 1162) = 2718$ m/s at the layer's top.

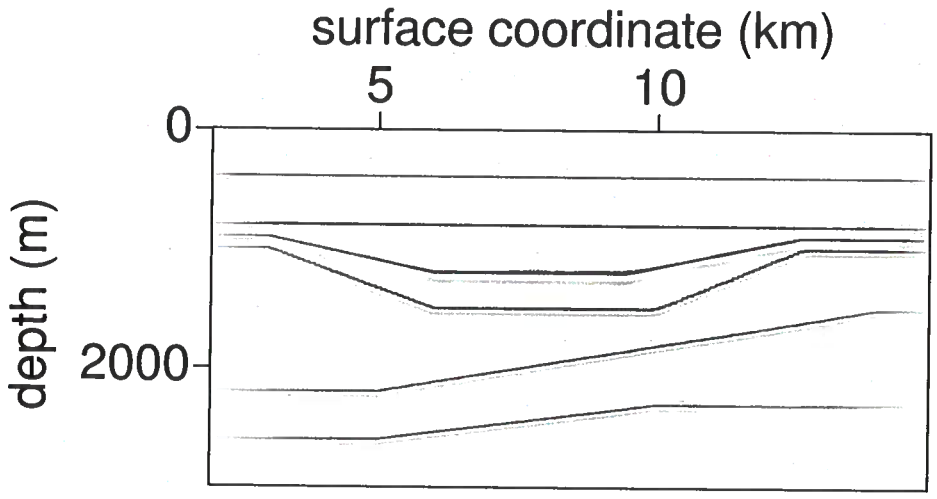

Figure 5.5. Stacked image obtained after prestack depth migration using the estimated parameters from Figures 5.2–5.4. The vertical velocity V_{P0} at the top of each layer was taken as known at the correct value.

out the velocity analysis for the second layer, which results in good estimates of all four parameters (Figure 5.3). Repeating the same procedure for the third layer with the velocity $V_{P0}(x = 4000, z = 1162) = 2718$ m/s, I obtain interval parameters close to the true values (Figure 5.4).

The shapes and depths of the reflectors imaged for the reconstructed velocity model (Figure 5.5) closely resemble those on the true image (Figure 5.1). This test confirms that migration velocity analysis in layered factorized VTI $v(x, z)$ media can be used to invert for the velocity gradients k_z and k_x and the anisotropic coefficients ϵ and δ if the vertical velocity is known at a single point in each layer.

5.1.2 V_{P0} in the second layer is incorrect

Now suppose that the vertical velocity $V_{P0}(x = 4000, z = 800)$ used for the top of the second layer has error (2600 m/s instead of 2300 m/s). Although this error in V_{P0} causes distortions in the inverted values of the other parameters (Figure 5.6), the effective quantities $V_{\rm nmo}(x = 4000, z = 800) = 2080$ m/s, $k_z = 0.56\,{\rm s}^{-1}$, $\hat{k}_x = 0.09\,{\rm s}^{-1}$, and $\eta = 0.23$ do not significantly differ from the true values, which corroborates the results for a single layer (Figure 4.5). Since the assumed value of $V_{P0}(x = 4000, z = 800)$ is higher than the correct velocity, the second layer is stretched in depth by about 13%, and the bottom of the syncline is imaged at a depth that is 80 m too large (Figure 5.8). This depth stretch in

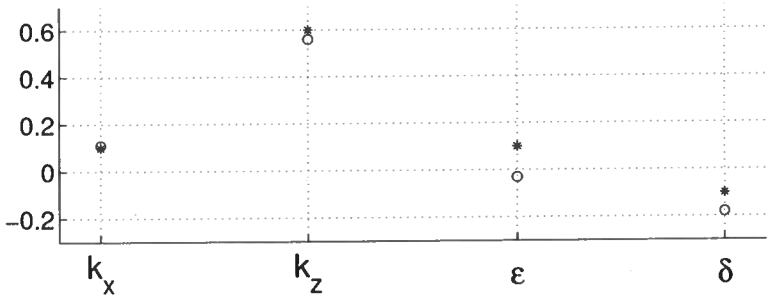

Figure 5.6. Estimated ($\circ$) and true ($\star$) parameters of the second layer obtained with an inaccurate value of the vertical velocity at the top of the second layer [$V_{P0}(x = 4000, z = 800) = 2600$ m/s].

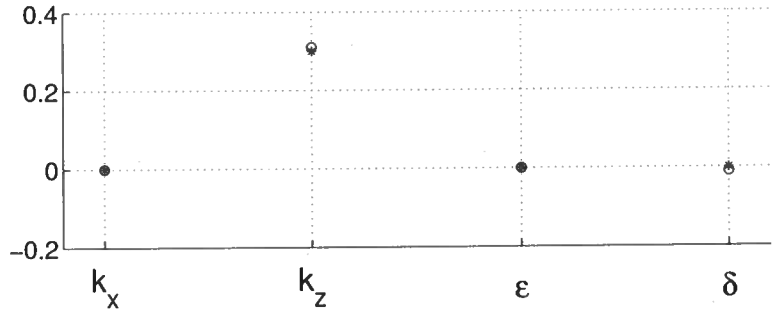

Figure 5.7. Estimated ($\circ$) and the true ($\star$) parameters of the third layer obtained with an inaccurate value of the vertical velocity at the top of the second layer [$V_{P0}(x = 4000, z = 800) = 2600$ m/s] but the correct $V_{P0}(x = 4000, z = 1208) = 2732$ m/s at the top of the third layer.

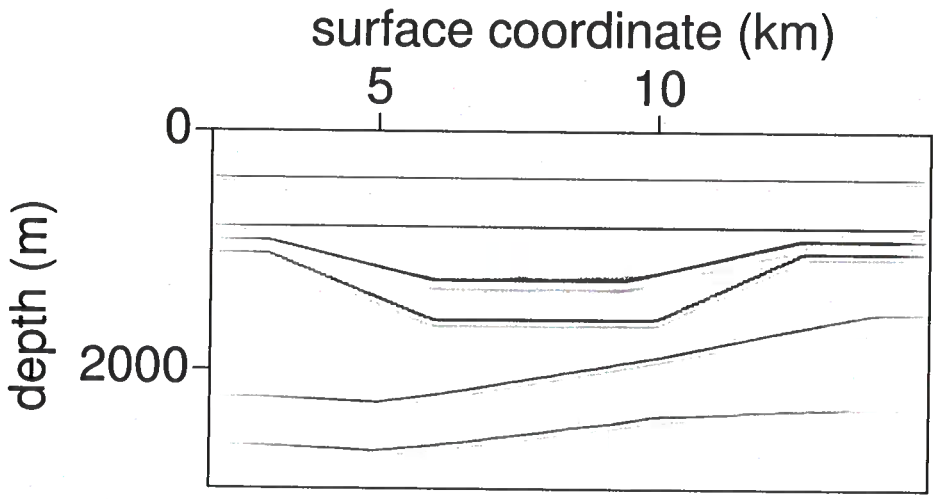

Figure 5.8. Stacked image obtained after prestack depth migration using the estimated parameters from Figures 5.2, 5.6, and 5.7. The vertical velocity V_{P0} at the top of the second layer was inaccurate.

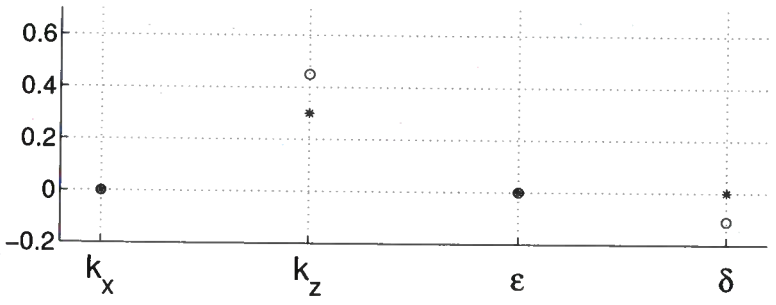

Figure 5.9. Estimated ($\circ$) and the true ($\star$) parameters of the third layer obtained for a large error in vertical velocity at the top of the second layer [$V_{P0}(x = 4000, z = 800) = 3500$ m/s] but the correct $V_{P0}(x = 4000, z = 1358) = 2778$ m/s at the top of the third layer. Because of the large distortions in the shape of the second layer, the estimated parameters $V_{\text{nmo}}(x = 4000\,\text{m}, z = 1345\,\text{m}) = 2453$ m/s, $k_z = 0.45$ s^{-1}, and $\eta = 0.14$ do not correspond to the correct $V_{\text{nmo}}(x = 4000\,\text{m}, z = 1345\,\text{m}) = 2778$ m/s, $k_z = 0.3$, and $\eta = 0.0$.

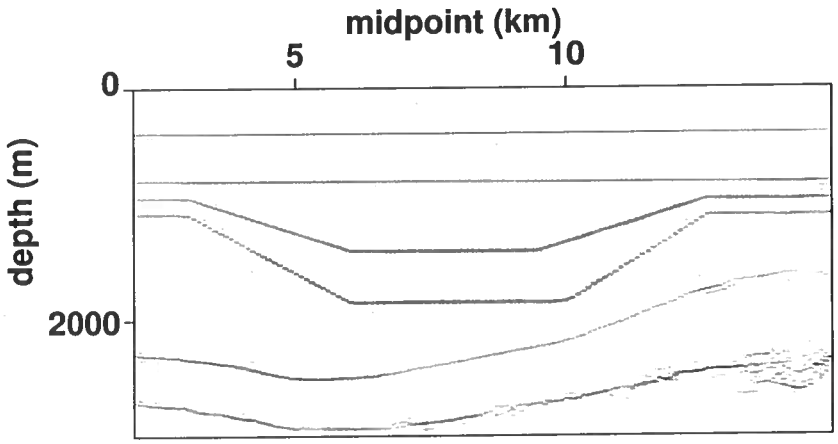

Figure 5.10. Stacked image after prestack depth migration with the estimated parameters shown in Figure 5.2 for the first layer, after introducing a large error in V_{P0} [$V_{P0}(x = 4000, z = 800) = 3500$ m/s] but keeping the correct values of V_{nmo}, η, k_z, and $\hat{k}_x$ in the second layer, and using the estimated parameters shown in Figure 5.9 for the third layer.

the second layer also causes a tilt of the syncline's flanks whose dips in Figure 5.8 exceed the true values.

To continue the velocity analysis, I fix the vertical velocity at the imaged top of the third layer at the correct value. Despite the depth shift of the top of the third layer, the algorithm yields accurate values of all four interval parameters (Figure 5.7). Because of the depth and dip distortions in the second layer, however, the two bottom reflectors are imaged at somewhat greater depths and are slightly deformed (Figure 5.8). In particular, on the left side of the section the fifth and sixth reflectors are no longer horizontal; they have acquired mild dips to conform to the stretched synclinal structure above.

For small errors in V_{P0}, the depth shifts in the second layer are small and do not influence the parameter estimates in the third layer (Figure 5.7). If, however, the error in V_{P0} in the second layer is large [$V_{P0}(x = 4000, z = 800) = 3500$ m/s, an error of over 52%], the resulting error in the dips of the second layer may cause a large enough differential lateral depth stretch to cause erroneous estimates of the parameters in the third layer. Then, as illustrated by Figure 5.9, V_{nmo}, k_z, and η will no longer be estimated with good accuracy in the third layer, and the resulting distortions in the imaged dips and depths of the reflectors are clearly seen in the stacked image (Figure 5.10). $\hat{k}_x$ will also be estimated with an error, but here, the error is negligible ($\Delta\hat{k}_x = 0.002$) and is ignored.

In general, the accuracy of all parameters V_{nmo}, k_z, $\hat{k}_x$, and η below a dipping anisotropic layer depends on the dip and the error in V_{P0} in the overburden. The error in the parameters

increases with increasing error in V_{P0} and with increasing dip, and is of concern especially in the presence of large dips (Le Stunff *et al.*, 2001; Grechka *et al.*, 2002). Therefore, although in the above example an error of 52% in V_{P0} may seem unrealistically large to be of any serious concern in parameter estimation, it should be noted that for much larger dips a smaller error is V_{P0} may be sufficient to cause similar errors.

5.1.3 V_{P0} is continuous across the boundaries

If no borehole information is available, one assumption that might be made is that the velocity V_{P0} is a continuous function of depth. Continuous velocity fields are acceptable approximations to the true velocity field because (1) the seismic wavelet has a finite frequency, which averages the true velocity field over the dominant seismic wavelength, and (2) parameter estimation methods, like the one I have developed, depend on traveltimes, which, being integral functions of the true velocity field, tend to smooth out velocity variations. Indeed, only the smooth low wavenumber components of the velocity field can be recovered robustly from reflection traveltimes (Santosa and Symes, 1989), and such estimates are almost always continuous.

When lateral velocity variation is insignificant, the velocity field may be assumed to be continuous at all points along the interface of the two layers or blocks, and, for the velocity analysis, V_{P0} may be fixed at any point along the interface. In the presence of significant lateral variation, however, my choice of a linear factorized $v(x,z)$ model does not always allow all points along the interface to be continuous. To determine a desirable point of continuity, I first migrate the data in the target layer with an isotropic homogeneous velocity field and then note the residual moveout of events at midpoints close to where I perform the velocity analysis. The migration velocity was chosen to equal the estimated V_{P0} at the bottom of the known adjacent layer. I choose the lateral location with the minimal residual moveout as the point of continuity. An isotropic homogeneous velocity field was used for migration because information about k_z and k_x were not available. If, however, such information were available, then they may also be used to compute the migration velocity field. At the point of continuity, I calculate V_{P0} with the estimated parameters of the known adjacent layer, and keep it fixed while performing velocity analysis in the target layer.

Note that estimating V_{P0}, or for that matter, a point of continuity, requires searching the null-space of the inverse problem. Hence, an error in the estimate is likely, and, among other things, the magnitude of the error depends on the values of the medium parameters and where the velocity analysis is performed. Because the moveout of events depends on the effective NMO velocity, the point of continuity estimated using my method is influenced by the true values of δ and k_z (Chapter 2). The influence of k_z can be reduced by studying events close to the boundary of the two layers or blocks. However, the influence of δ cannot be ignored. In general, my method tends to favour a lateral location where $V_{P0,M} \rightarrow V_{\mathrm{nmo},T}$, which results in minimizing the absolute value of $\delta_M \rightarrow 0$. Since subsurface values of δ are usually small I expect that the errors introduced by implementing this procedure will be small and a reasonable velocity model can be constructed with minimal *a priori* information,

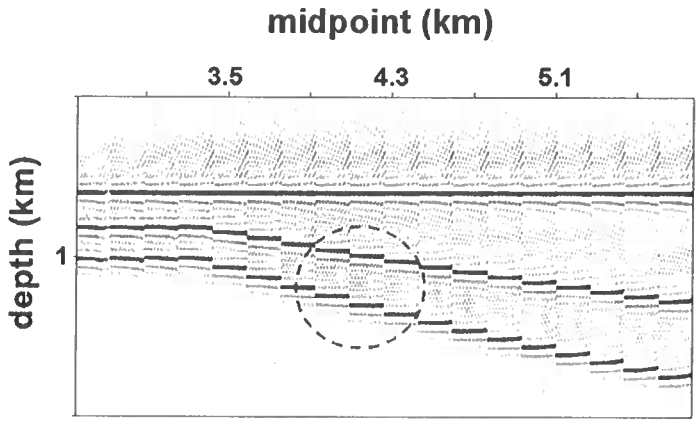

Figure 5.11. Image gathers for the second, third, and fourth reflectors obtained after using a homogeneous isotropic velocity field for the second layer that is continuous across the second reflector. The minimum residual moveout of events along the third and fourth reflectors is at midpoint locations near 3900 m.

such as knowing the vertical velocity at the top of the subsurface.

To illustrate this procedure I apply this technique on the synthetic example shown in Figure 5.1, and in Chapter 6 I show the validity of this approach on field data. To identify the point of continuity at the boundary between the first and second layers, I examine the moveout along the third and fourth reflectors (only for offsets smaller than 1000 m) after migration with an isotropic homogeneous velocity field in the second layer. The migration velocity was chosen to be equal to the true velocity at the bottom of the first layer (i.e., at the second reflector); image gathers obtained after migration are shown in Figure 5.11. To select the point of continuity, I pick the surface coordinate with the smallest residual moveout on the image gathers at the third and fourth reflectors. This criterion yielded $x = 3900$ m, which is sufficiently close to the true point of continuity for the second reflector ($x = 4000$ m). Using the estimated vertical velocity at $x = 3900$ m [$V_{P0}(x = 3900, z = 800) = 2316$ m/s], I estimate the parameters of the second layer with high accuracy (Figure 5.12).

To find the point of continuity between the second and third layers, I again perform prestack depth migrations assuming that the third layer is homogeneous and isotropic. Since the second layer is laterally heterogeneous, the migration velocities range from 2400 m/s to 3400 m/s. Applying the criterion of minimum residual moveout for the fifth and the sixth reflectors, the point of continuity was found at ($x = 5937, z = 1483$), where the vertical velocity is $V_{P0} = 2900$ m/s. Although the location ($x = 5937, z = 1483$) is shifted by almost 1000 m from the true continuity point between the second and third layers, it is close enough that the results of the velocity analysis (Figure 5.13) and imaging (Figure 5.14)

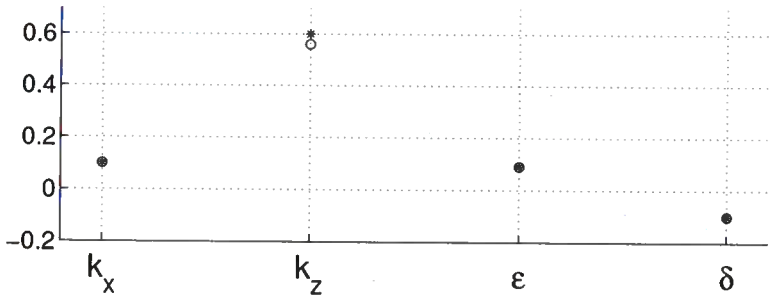

Figure 5.12. Estimated (∘) and true (⋆) parameters of the second layer obtained assuming that V_{P0} is continuous between the first and second layers at the point $(x = 3900, z = 1208)$.

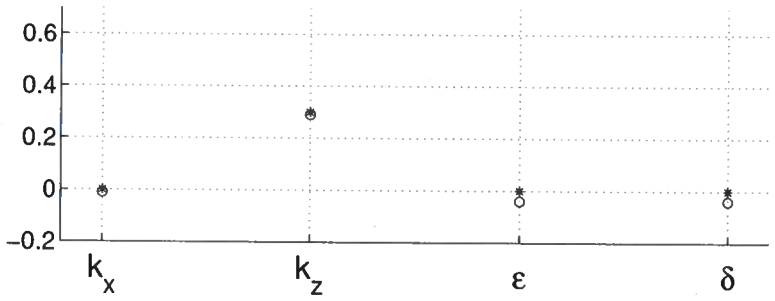

Figure 5.13. Estimated (∘) and true (⋆) parameters of the third layer obtained assuming that V_{P0} is continuous between the first and second layers at the point $(x = 3900, z = 1208)$ and between the second and third layers at the point $(x = 5937, z = 1483)$.

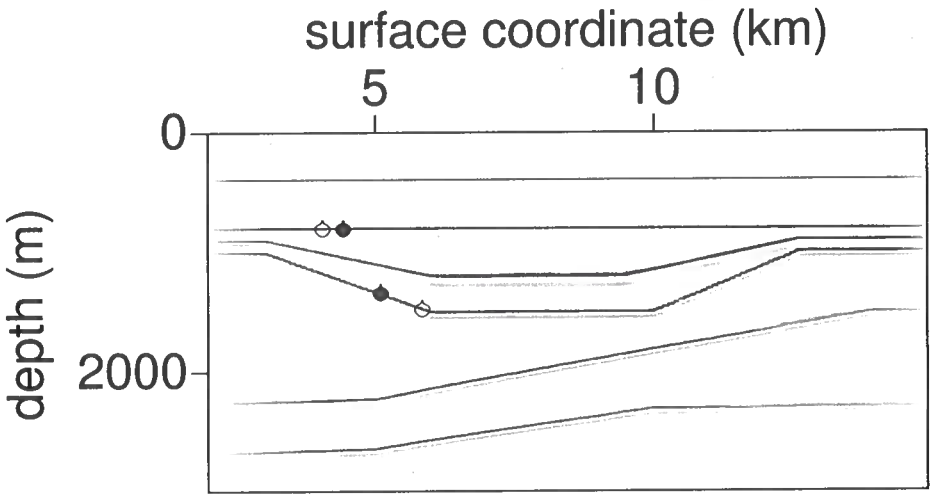

Figure 5.14. Stacked image obtained after prestack depth migration using the estimated parameters from Figures 5.2, 5.12, and 5.13. The vertical velocity was assumed to be continuous between the first and second layers at the point ($x = 3900, z = 1208$) and between the second and third layers at the point ($x = 5937, z = 1483$); these points are marked by ($\circ$). The true continuity points are marked by ($\bullet$).

are quite satisfactory.

In the absence of borehole data, the assumption of continuous vertical velocity provides a practical way to build an anisotropic heterogeneous model for prestack migration. Depending on the complexity of the model, however, the point of continuity may be estimated with a substantial lateral shift or may not exist at all. Still, my tests show that for models without steep dips or strong lateral heterogeneity, an error in identifying the point of continuity does not distort the effective parameters V_{nmo}, k_z, $\hat{k}_x$, and η. That is, precision in that location is not essential. Therefore, the migrated section would still be well focused, although the imaged reflectors would be subject to a depth stretch if V_{P0} is erroneously estimated.

5.2 Test for a more complicated synthetic model

Now consider a more complicated model (Figure 5.15) consisting of five layers or blocks. The first block represents water, the second and fourth blocks are factorized $v(z)$ VTI, the third block is factorized $v(x,z)$ VTI, and the fifth block is isotropic $v(x,z)$. Dips reach maximum values of about 60 °. For such large dips I expect even small errors in V_{P0} in the overburden to cause imaging errors at the target.

The layer-stripping technique discussed above is used to perform the velocity analysis. As before, in the absence of any *in situ* velocity information, I assume V_{P0} to be continuous at a certain point on block boundaries. Keeping the value of V_{P0} fixed at the point of continuity, I use the moveout of events associated with two reflectors to estimate the rest of the parameters in each block.

Migrating the data in the first block with water velocity delineates the bottom of this block. To obtain the parameters of the second block, I first fix the value of V_{P0} at the top of the second block at its true velocity ($V_{P0} = 1500$ m/s). This represents the top of a near surface block with velocity close that of water. Then using the residual moveout information of two events in the second block, I estimate its parameters with good accuracy (compare Figures 5.15 and 5.16).

To estimate the point of continuity between the second and third blocks, I migrate the data with a homogeneous isotropic velocity field. The migration velocity was chosen equal to the vertical velocity at the bottom of the second block. The location on the third reflector closest to the point on the fourth reflector with the smallest residual moveout was chosen as the point of continuity. Keeping $V_{P0} = 2470$ m/s at the point of continuity ($x = 3000\,\text{m}, z = 1590\,\text{m}$) fixed, I estimate the parameters of the third block. Although my estimated point of continuity differs from the true one ($x = 3250\,\text{m}, z = 1600\,\text{m}$), it is readily close enough such that, as Figure 5.16 shows, the estimated parameters and the imaged reflectors are obtained with good accuracy.

To estimate the point of continuity and V_{P0} at the top of the fourth block, migration for the sixth and seventh reflectors is carried out with a range of isotropic homogeneous velocity fields (between 2470 m/s to 3010 m/s). The minimum residual moveout of events on the sixth and seventh reflectors is observed for a velocity of 3010 m/s, which corresponds to the estimated velocity in the third block at a point ($x = 5000\,\text{m}, z = 2293\,\text{m}$) on the

boundary between the third and fourth blocks. I choose this point as the point of continuity between the two blocks. In the true model, however, a point of continuity between third and fourth blocks does not exist. Therefore, by introducing a point of continuity I make a 4% error in V_{P0}, setting $V_{P0}(x = 5000\,\text{m}, z = 2293\,\text{m}) = 3010$ m/s instead of of the true value of 3117 m/s. Because of the error in V_{P0}, the other estimated parameters are estimated with an error, the thickness of the block is reduced, and the reflectors in this block are imaged with smaller than the correct dips (Figure 5.16). Note that if the discontinuity between the two blocks were larger, then the error in estimating V_{P0} by introducing a point of continuity would also be larger.

Assuming that the fifth block is known to be isotropic, no *a priori* information about V_{P0} is necessary to estimate the parameters in this block (Liu, 1995). Using only the residual moveout information at midpoint locations at the left end of the model, where the overburden is close to being horizontally layered, I estimate V_{P0}, k_x, and k_z with good accuracy (Figure 5.16).

Figure 5.17 shows image gathers after depth migration with the estimated velocity field. Except for the encircled area events everywhere in the section are flat. The residual moveout visible in the fifth block around midpoint 4.5 km is caused by the distortions in the fourth block, which is related to the error in V_{P0} discussed above. As illustrated by Figure 5.18, a negative error in V_{P0} in the fourth block causes a pull up of the bottom of the block, and subsequently, portions of reflectors in the fifth block directly below the squeezed fourth block are also pulled up. This results in a false kink to appear in the eighth and ninth reflectors. Around this kink image gathers are not flat even if the correct values of the parameters are used to migrate the fifth block. If this residual moveout can be identified, then the vertical velocity in the overburden may be adjusted manually or automatically to flatten the gathers. In this example, I manually adjusted the vertical velocity in the fourth block, while keeping V_{nmo}, $\hat{k}_x$, k_z, and η at the correct values, until the residual moveout in the fifth block around midpoint 4.5 km was minimized. The resulting flat image gathers obtained with the correct V_{P0} are shown in Figure 5.19 and the corresponding stacked image is displayed in Figure 5.20.

Note that the need to correct V_{P0} in block IV was evident only because I had correctly assumed that block V was isotropic and the parameters in the block were correctly estimated. More often than not, however, such *a priori* information is not available. Then, the presence of residual moveout may indicate errors in the estimated parameters for the target layer that can be corrected by accounting for more anisotropy or heterogeneity. For example, one may attempt to incorrectly flatten the residual moveout in block V by making it a factorized $v(x, z)$ medium, or by subdividing the block laterally or vertically into two smaller isotropic heterogeneous blocks such that the excess heterogeneity and anisotropy compensates for the error in V_{P0} in block IV. Indeed, the parameter estimation from reflection seismic data is a nonunique problem, and the ambiguities increase with the complexity of the medium. For a complicated medium there are many models, all wrong, that may flatten events in image gathers (Stork, 1992), but the key in implementing MVA is to use a technique that requires minimal *a priori* information to resolve the existing ambiguities.

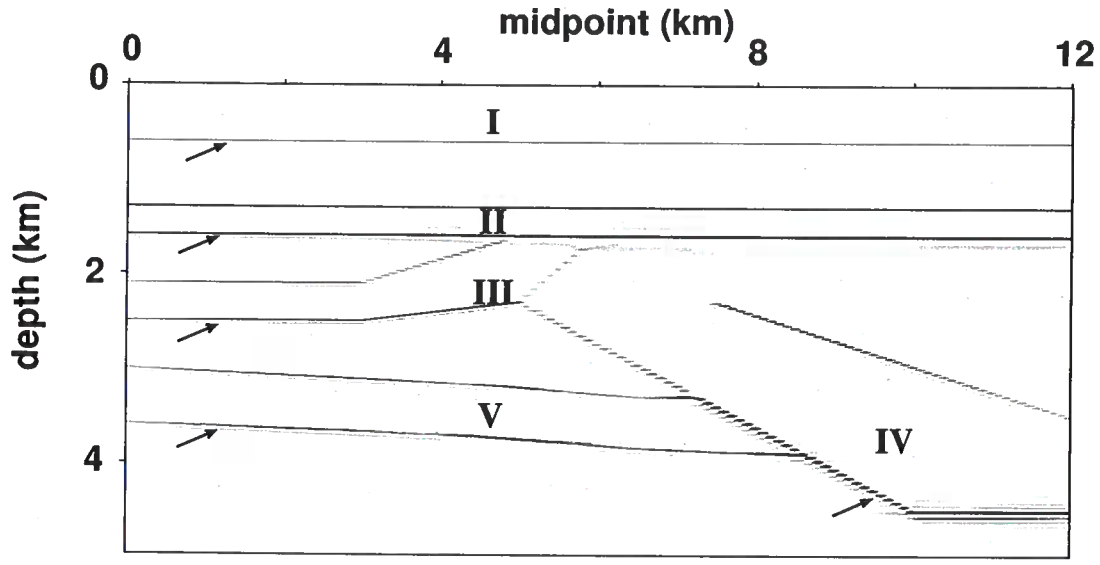

Figure 5.15. True image of a multilayered factorized medium. The blocks are numbered with Roman numerals. Except for the nearsurface water layer, each block includes two reflectors, where every second reflector (here indicated by the arrows) represents the bottom of a block. Block I is homogeneous and isotropic with a velocity of 1500 m/s. Parameters for block II are $V_{P0}(z = 600\,\mathrm{m}) = 1500\mathrm{m/s}$, $k_z = 1.0\ \mathrm{s}^{-1}$, $k_x = 0.0\ \mathrm{s}^{-1}$, $\epsilon = 0.36$, and $\delta = 0.1$; for block III, $V_{P0}(x = 3250\,\mathrm{m}, z = 1600\,\mathrm{m}) = 2500$ m/s, $k_z = 0.3\ \mathrm{s}^{-1}$, $k_x = 0.2\ \mathrm{s}^{-1}$, $\epsilon = 0.1$, and $\delta = 0.0$; for block IV, $V_{P0}(x = 5000\,\mathrm{m}, z = 2300\,\mathrm{m}) = 3120$ m/s, $k_z = 0.5\ \mathrm{s}^{-1}$, $k_x = 0.0\ \mathrm{s}^{-1}$, $\epsilon = 0.3$, and $\delta = 0.15$; for block V, which is isotropic, $V_{P0}(x = 7750\,\mathrm{m}, z = 3800\,\mathrm{m}) = 3865$ m/s, $k_z = 1.0\ \mathrm{s}^{-1}$, $k_x = 0.1\ \mathrm{s}^{-1}$, $\epsilon = 0.0$ and $\delta = 0.0$.

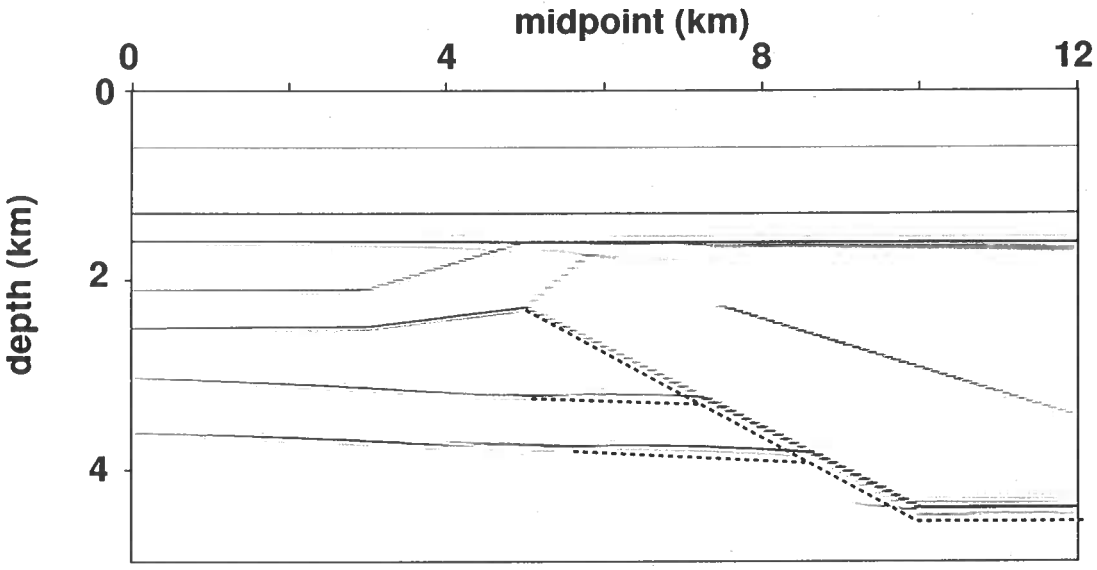

Figure 5.16. Image obtained after prestack depth migration with the estimated parameters. The velocity in block I was assumed to be known. Estimated parameters for block II are $V_{P0}(z = 600\,\text{m}) = 1500\text{m/s}$, $k_z = 0.98\ \text{s}^{-1}$, $k_x = 0.0\ \text{s}^{-1}$, $\epsilon = 0.38$, and $\delta = 0.12$. for block III, $V_{P0}(x = 3000\,\text{m}, z = 1590\,\text{m}) = 2470\ \text{m/s}$, $k_z = 0.19\ \text{s}^{-1}$, $k_x = 0.22\ \text{s}^{-1}$, $\epsilon = 0.09$, and $\delta = 0.0$; for block IV, $V_{P0}(x = 5000\,\text{m}, z = 2293\,\text{m}) = 3010\ \text{m/s}$, $k_z = 0.51\ \text{s}^{-1}$, $k_x = 0.0\ \text{s}^{-1}$, $\epsilon = 0.36$, and $\delta = 0.21$; for block V, $V_{P0}(x = 7750\,\text{m}, z = 3800\,\text{m}) = 3764\ \text{m/s}$, $k_z = 0.85\ \text{s}^{-1}$, $k_x = 0.1\ \text{s}^{-1}$, $\epsilon = 0.0$, and $\delta = 0.0$. The imaged positions of the reflectors are shown with the solid lines; the dashed lines mark the true position of reflectors in the fourth and fifth blocks.

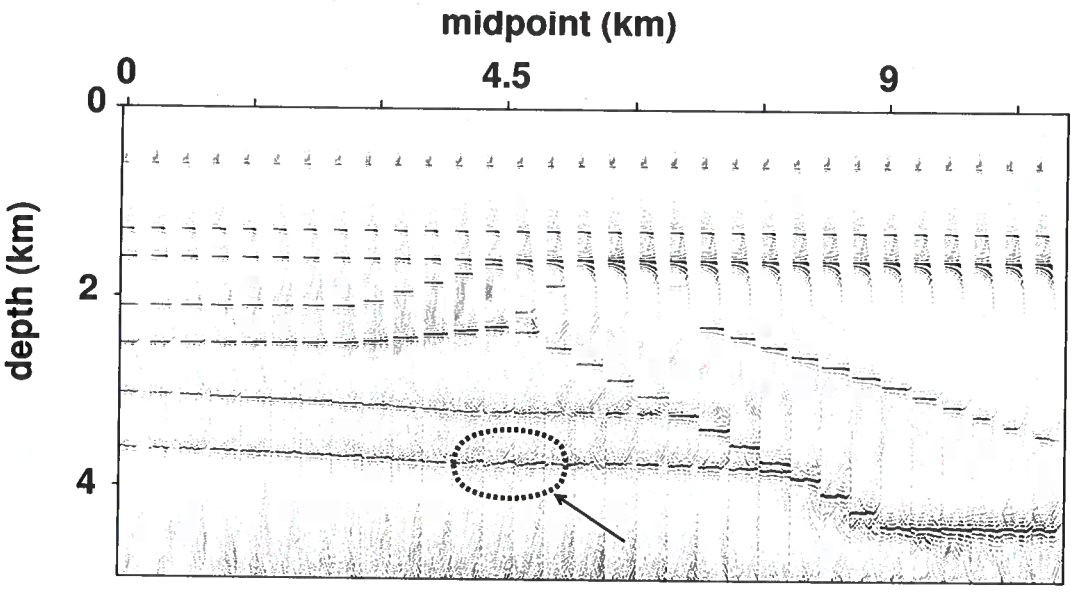

Figure 5.17. Image gathers obtained after depth migration with the estimated parameters shown in Figure 5.16. Except for the encircled region (marked by the arrow), reflection events are flat throughout the section.

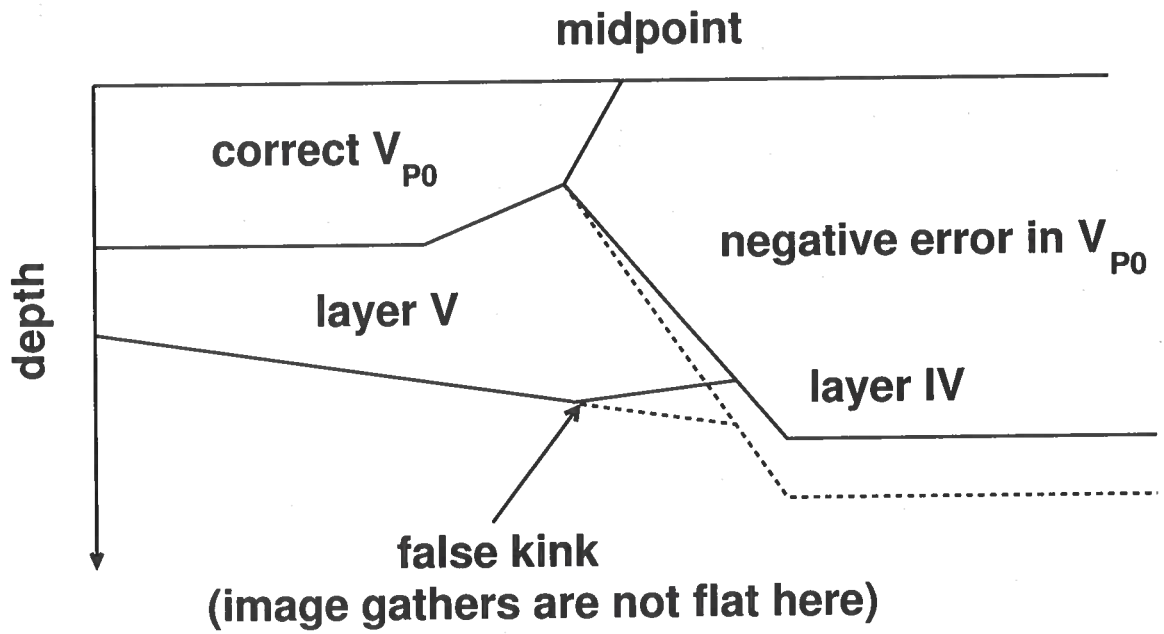

Figure 5.18. Cartoon showing that a negative error in V_{P0} in the fourth block causes a pull up of reflectors in that block. This in turn, results in imaging the reflectors in the fifth block with a false kink. The solid lines show the imaged positions of the reflectors; the dashed lines show their true positions. Events in image gathers close to the kink are not flat, even though the parameters in the fifth block were estimated with good accuracy.

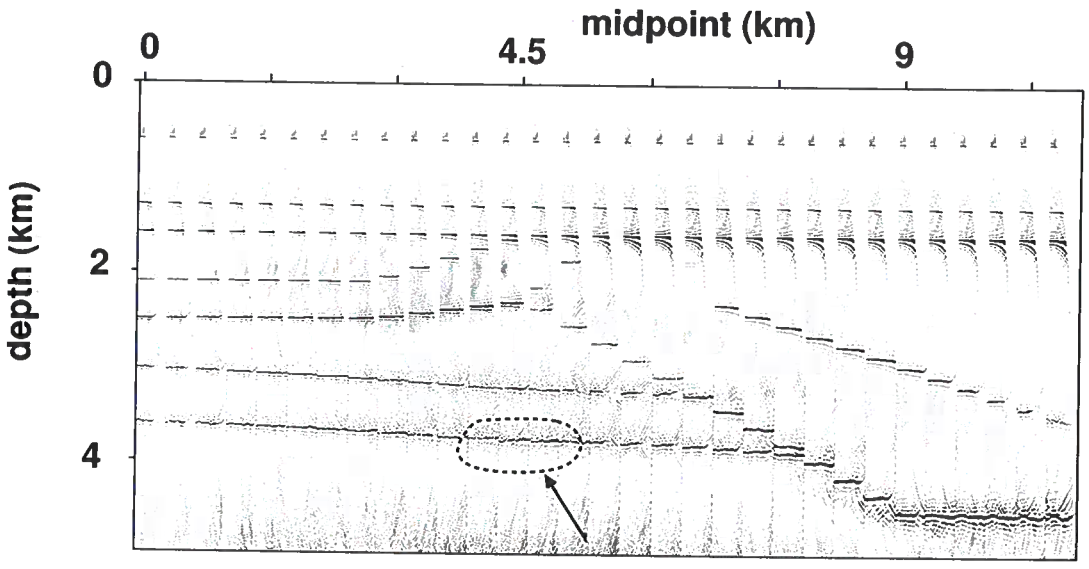

Figure 5.19. Same as Figure 5.17, but now the correct value of V_{P0} was used in the fourth block [$V_{P0}(x = 5000\,\mathrm{m}, z = 2293\,\mathrm{m}) = 3117$ m/s, $\epsilon = 0.30$, $\delta = 0.16$, and $k_z = 0.51$ s^{-1}]. Note that all events, including those inside the encircled area, are flat.

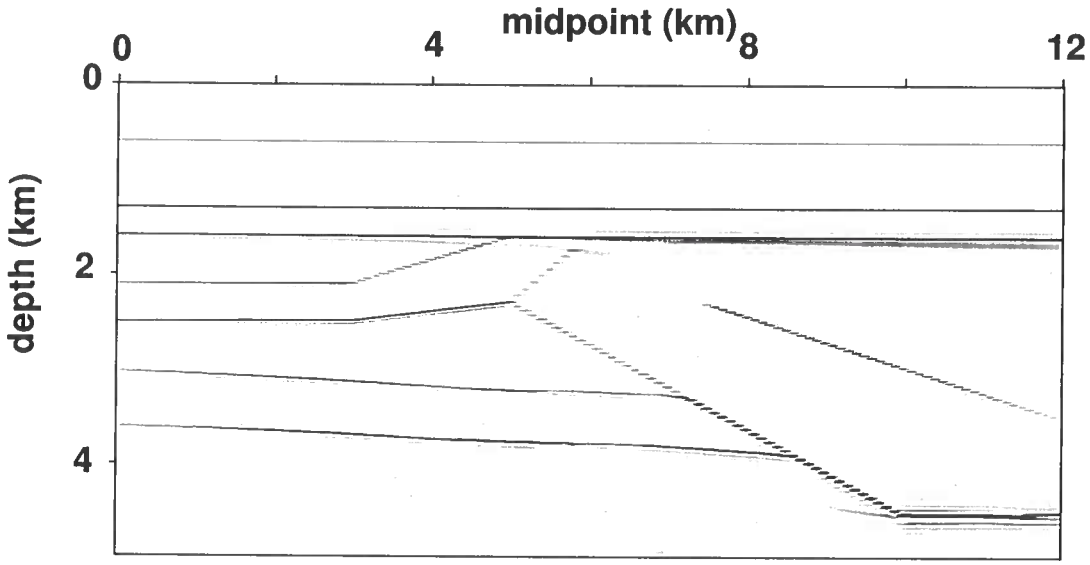

Figure 5.20. Same as Figure 5.16, but now the correct value of V_{P0} was used in the fourth block [$V_{P0}(x = 5000\,\text{m}, z = 2293\,\text{m}) = 3117$ m/s, $\epsilon = 0.30$, $\delta = 0.16$, and $k_z = 0.51$ s^{-1}].

Chapter 6

Field data examples

6.1 Geological history of the area

Here I apply the migration velocity analysis technique developed above to two offshore seismic lines from West Africa. The geology of the area is governed by tectonic rifting that occurred around the early Cretaceous. The major tectono-stratigraphic units in the order they were formed are (Brice *et al.*, 1982): (1) Prerift with gentle tectonism; (2) synrift I with strong tectonism; (3) synrift II with moderate tectonism; (4) postrift with gentle tectonism, and (5) regional subsidence with major tilting. The available seismic sections record only the subsidence and postrift phases in geologic history, a schematic diagram of which is shown in Figure 6.1.

The regional subsidence phase dates to the Oligocene and Miocene times. It is characterized by a rapidly deposited regressive sequence, turbidites, shaly clastics, and high-pressure shale. The reflectors within this unit are weak and discontinuous, often chaotic, and show extensive cut-and-fill patterns. The ubiquitous presence of shales makes this section strongly anisotropic. The thickness of this unit increases away from the shore, and at places can reach six kilometers.

The postrift deposition dates to the early Tertiary. This unit is thicker near the shore, where it can be up to two kilometers thick. Marine clastics and carbonates, nonmarine red beds, and transgressive sequences make up most of its lithologic character. Seismic velocity within the postrift unit varies significantly and is proportional to the carbonate content in the sediments. The structural style is defined by gentle conformable folds towards the top while faulting and complex halokinesis characterizes its base.

6.2 First line

The lateral extent of this section is about 9 km; it primarily consists of subhorizontal reflectors with negligible lateral velocity variation. The water is about 150 m deep, and the subsidence and the postrift units are both approximately 2 km thick. A time variant gain was applied to boost the amplitudes at late times; a dip filter and a mute were applied on CMP gathers to remove groundroll and some near-surface low-velocity dipping events.

As the first step in building the velocity model and imaging the subsurface, I identified the water bottom by migrating and stacking the data with a moveout velocity of 1500 m/s. Next, I estimated the velocity field of the near-surface sediments. Because this block is too thin ($\approx$ 400 m) to allow picking of two separate events for a stable inversion, I did not use

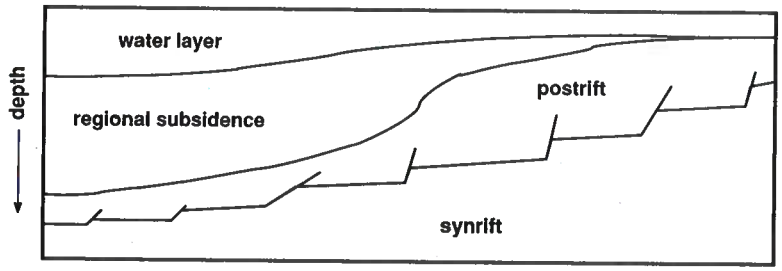

Figure 6.1. Cartoon of the geological history of the area showing the subsidence, postrift, and the synrift units.

migration velocity analysis to estimate its velocity field. Instead, I assumed that the top of this block had the water velocity (1500 m/s) and computed the vertical gradient $k_z = 0.8$ s^{-1} by solving equation (3.6) using NMO velocities obtained from standard stacking velocity analysis. Figure 6.2 shows common image gathers after migration with the estimated near-surface velocity field. The deepest events with no residual moveout define the bottom of this block.

Next, I proceed to estimate the velocity of the third block using migration velocity analysis. To estimate the vertical velocity at the top of the block, which is required to get unique estimates of the medium parameters, I assume that V_{P0} at a certain point on the boundary between the second and the third blocks is continuous. Because the residual moveout of events in the third block shows negligible lateral variation (Figure 6.2), I expect that the lateral gradient k_x in this block can be neglected. In the absence of any lateral velocity variation and dipping reflectors, any point on the boundary between the two blocks can suffice as the point of continuity. I assumed that the velocity is continuous at the point ($x = 3000\,\text{m}, z = 452\,\text{m}$), which is close to the midpoints where I picked residual moveout and performed MVA, and computed $V_{P0} = 1740$ m/s at this point using the estimated parameters of the near-surface block. Using this V_{P0} and the residual moveout of two events between midpoints 0 and 3 km (Figure 6.3), I estimated k_z, k_x, ϵ, and δ. Starting with a homogeneous isotropic velocity model, the algorithm converged to $k_z = 0.6 \pm 0.03$ s^{-1}, $k_x = 0.0 \pm 0.01$ s^{-1}, $\epsilon = 0.3 \pm 0.03$, and $\delta = 0.06 \pm 0.02$. These parameters correspond to a value of $\eta = 0.21 \pm 0.03$, which indicates that the block is strongly anisotropic. Although these estimated parameters flatten events at midpoints less than four kilometers, events at midpoints greater than four kilometers are overcorrected (Figure 6.3). Therefore, the third block has a limited lateral extent, as marked in Figure 6.3.

To compute the optimal parameters for the fourth block, I do migration velocity analysis in the same depth interval as that for the third block, but at the right segment of the line, where residual moveout is still present. As before, I select the point of continuity between the second (near-surface) and the fourth block close to the midpoints where I performed MVA ($x = 7000\,\text{m}$, $z = 310$ m) and compute the vertical velocity at this point ($V_{P0} = 1625$ m/s)

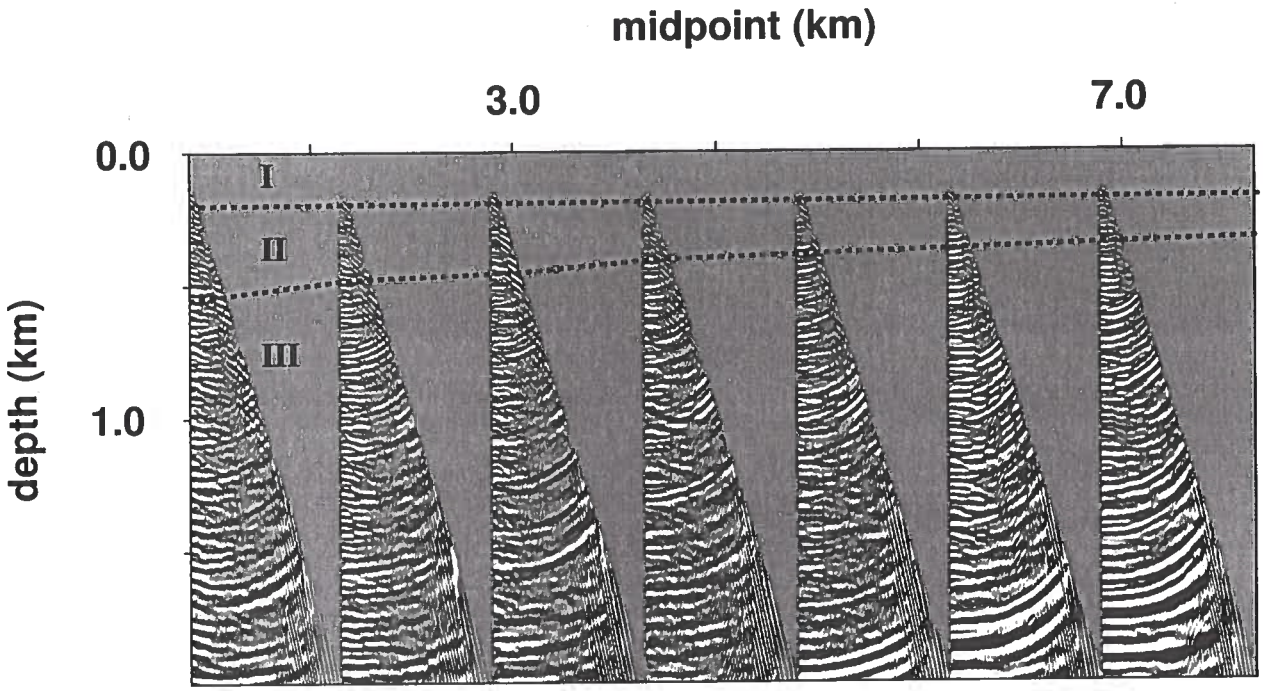

Figure 6.2. Common-image gathers, computed with an increment of one kilometer, after prestack depth migration using $V_{P0} = 1500$ m/s for the water layer, and $V_{P0} = 1500$ m/s and $k_z = 0.8$ s^{-1} for the sediments. The locations of the blocks I, II, and III are marked. The dashed line marks the maximum depths at which events are flat; it was used as the bottom of the second (near surface) block and the top of the third block. The overcorrected events below the dashed line indicate that these parameters are not appropriate for the deeper reflectors.

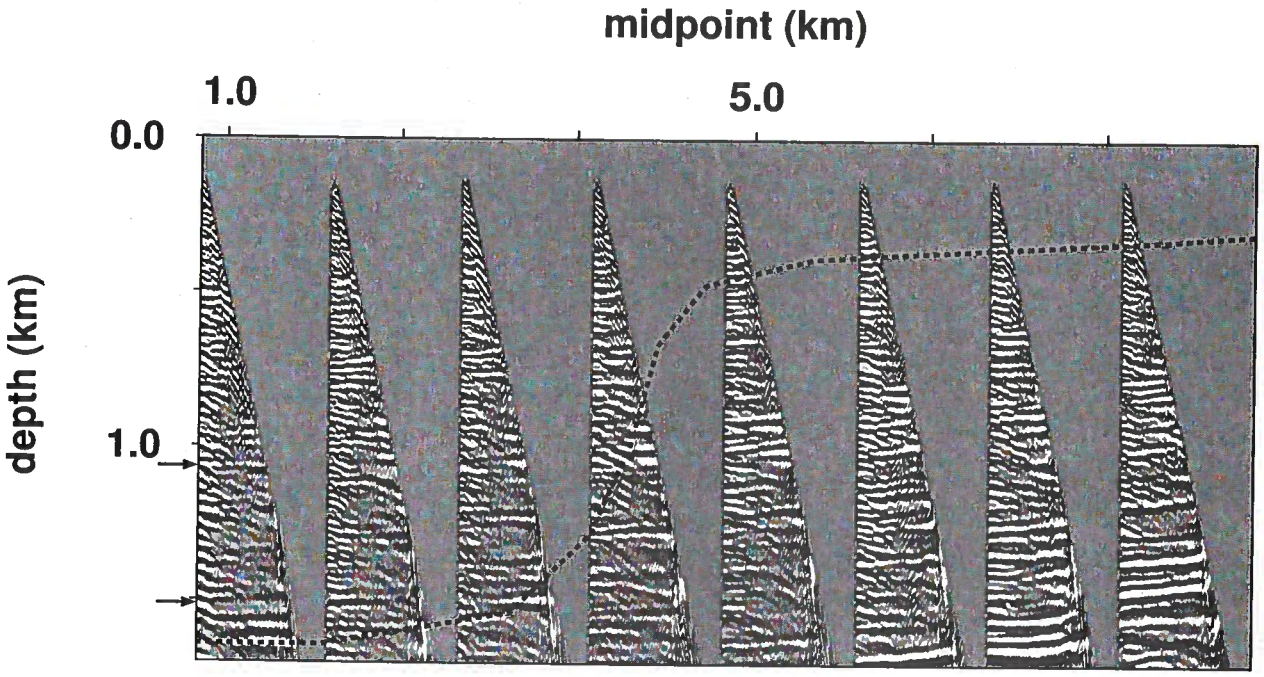

Figure 6.3. Common-image gathers after migration velocity analysis using the residual moveout between midpoints one and three km along the two events marked by the arrows. The dashed line marks the bottom of the third block. Most events below the dashed line exhibit residual moveout.

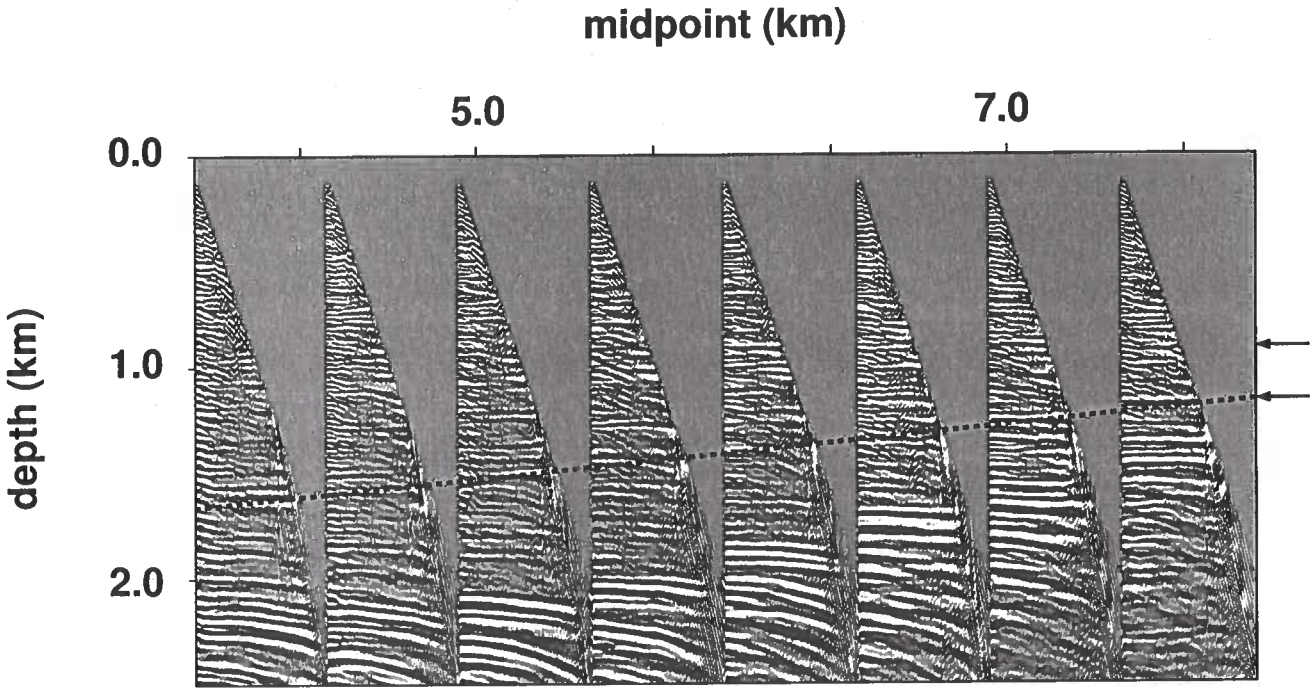

Figure 6.4. Common-image gathers, computed with an increment of 500 m, after migration velocity analysis using the residual moveout between midpoints 6.5 km and 8 km along the two events marked by the arrows. The flat events above the dashed line indicate that the estimated parameters are good for this part of the section. The dashed line separates the third and fourth blocks from the deeper, fifth, block.

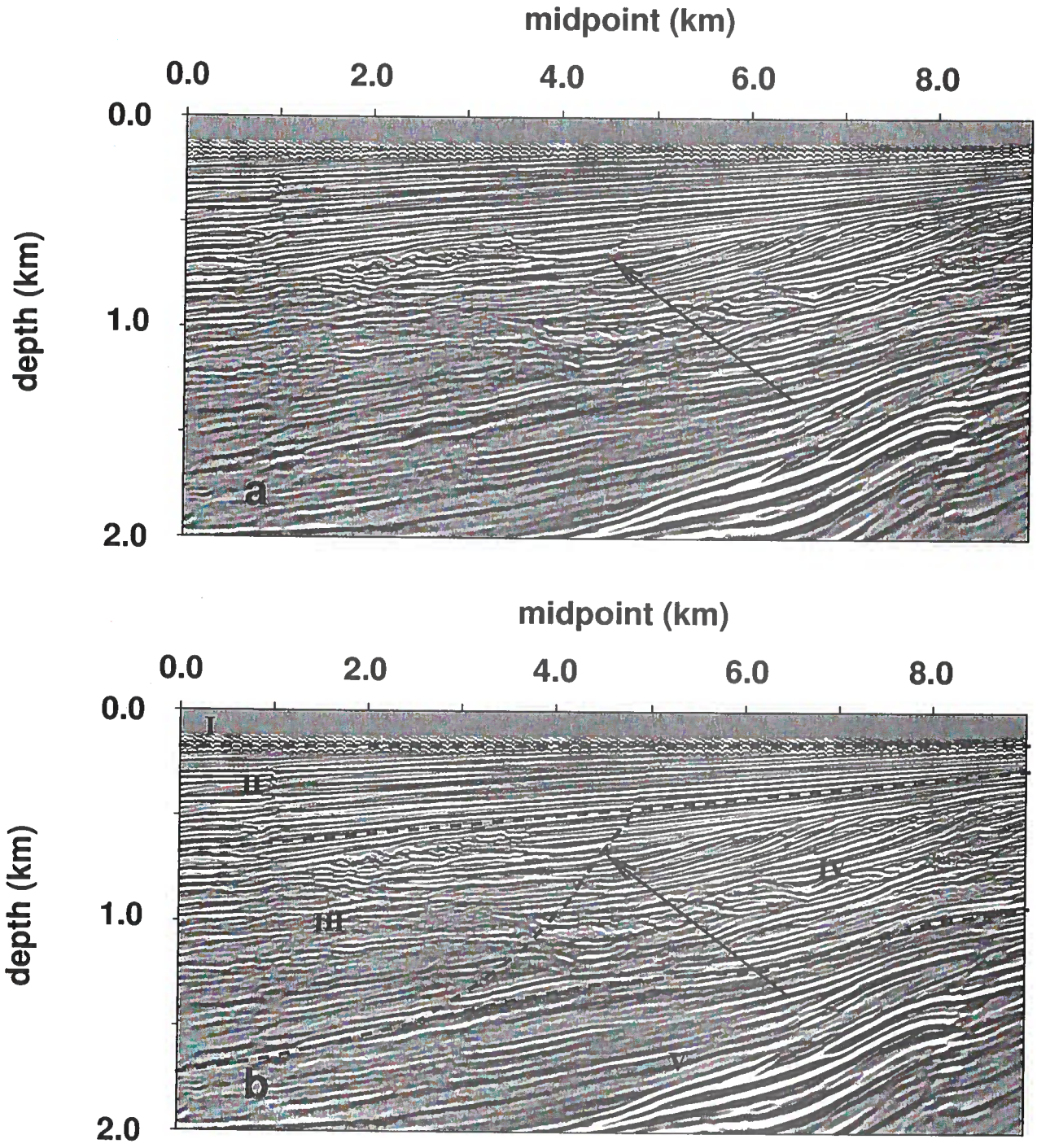

Figure 6.5. (a) First two km of the stacked depth section after prestack depth migration with the estimated parameters. (b) Same section, with the block boundaries marked. The arrow points to the fault that separates the third and the fourth blocks.

using the parameters of the second block. Keeping $V_{P0}(x = 7000\,\mathrm{m}, z = 310\mathrm{m}) = 1625$ m/s fixed, I carried out migration velocity analysis using the residual moveout of two events (Figure 6.4) between midpoints 6 and 8 km. The algorithm converged to the following values $k_z = 0.65 \pm 0.03$ s^{-1}, $k_x = 0.0 \pm 0.01$ s^{-1}, $\epsilon = 0.35 \pm 0.03$, and $\delta = 0.1 \pm 0.02$. The image gathers after migration with the parameters of the fourth block estimated from migration velocity analysis are shown in Figure 6.4, and the shallow portion of the stacked section is shown in Figure 6.5. The arrow in Figure 6.5 points to the fault plane that serves as the boundary between the third and fourth blocks, and the bottom of these two blocks is marked by the dashed line in Figure 6.4. Observe that, although the parameters of the fourth block flatten events in this block, deeper events remain undercorrected.

The optimal parameters required to flatten the undercorrected events in the fifth block were again estimated by migration velocity analysis. To estimate the value of V_{P0} at the top of the block, I did an isotropic homogeneous prestack depth migration using the vertical velocity at the bottom of the fourth block evaluated close to the midpoints where I perform velocity analysis [$V_{P0} = 2230$ m/s]. The decrease in the residual moveout with increasing lateral coordinate (Figure 6.6) clearly indicates the presence of a significant lateral velocity variation in the fifth block. Since the minimum residual moveout was observed at midpoint 7 km, I assumed ($x = 7000\,\mathrm{m}, z = 1235\,\mathrm{m}$) to be the point of continuity between blocks four and five, and fixed $V_{P0} = 2230$ m/s at this point for the migration velocity analysis. Using the residual moveout between midpoints 4 and 6 km along the two reflectors marked in Figure 6.7 yields $k_z = 0.83 \pm 0.04$ s^{-1}, $k_x = 0.04 \pm 0.01$ s^{-1}, $\epsilon = 0.19 \pm 0.03$, and $\delta = 0.06 \pm 0.03$. The stacked image obtained after migration with the estimated parameters is shown in Figure 6.7, and the corresponding common-image gathers (most of them are flat) are shown in Figure 6.8.

The estimated vertical velocity field is shown in Figure 6.9, and the parameter η is shown in Figure 6.10. As expected, the ubiquitous presence of shales in the subsidence unit at depths less than two kilometers makes this section strongly anisotropic ($\eta \approx 0.21$). The deeper postrift unit is also anisotropic, although to a lesser extent than the shallow subsidence unit, and is characterized by moderate lateral velocity variation. In the subsidence unit, the large maximum offset-to-depth ratios (≈ 2) for the two reflectors available for velocity analysis provides sufficiently tight constraints on the value of η in the entire unit. In the postrift section, however, only the shallow reflector has the maximum offset-to-depth ratio close to two; the maximum offsets for the deeper reflector is smaller than the depth. Thus, the value of η in this unit is well-constrained only above the first reflector. Absence of prominent reflectors at greater depths and decreasing offset-to-depth ratios make estimates of η for the deeper part of the section unstable.

For this line, my estimate for the maximum value of η ($\eta_{\max} \approx 0.21$) is much larger than that obtained by Alkhalifah (1996) ($\eta_{\max} \approx 0.1$). Although it is difficult to compare these two values, it is likely that my method gives more reliable estimates, because migration velocity analysis is more robust in the presence of noise than time-domain techniques; also by considering the factorized model, I was able to decouple heterogeneity and anisotropy, which was not possible to do using time-domain techniques. In addition, the time-depth curve computed from my estimated vertical velocity field at midpoint 5 km closely matches

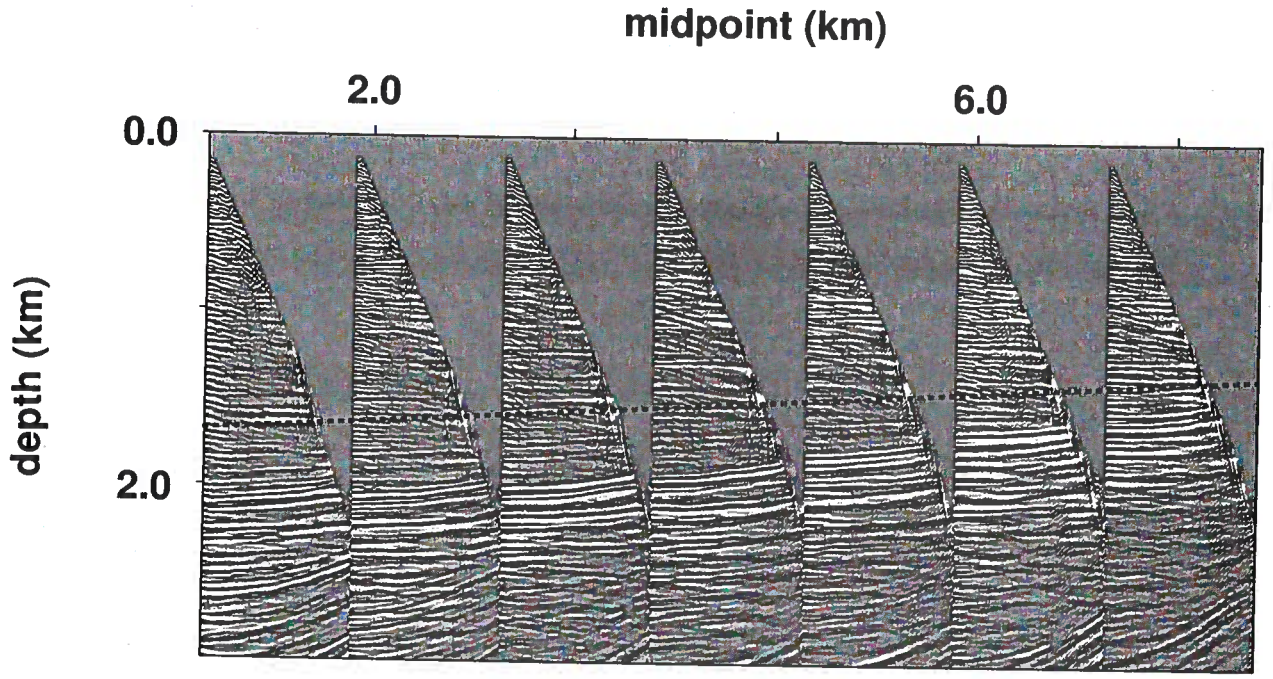

Figure 6.6. Common-image gathers after migration using the estimated parameters in blocks 1-4, and an isotropic homogeneous velocity field with $V_{P0} = 2230$ m/s for the deeper section. Observe that, the residual moveout of events below the bottom of the third and fourth blocks (marked with the dashed line) decreases from left to right.

the curve computed from *in situ* measurements at a borehole close to this line (Figure 6.11).

6.3 Second line

Although migration velocity analysis improves parameter estimation because of its robustness in the presence of noise, it is valuable primarily because of its ability to provide estimates of medium parameters and to do imaging in the presence of significant lateral velocity variation. In this section, I apply my algorithm to another line from offshore West Africa, where the anisotropy coefficients and the vertical velocity varies significantly. This line is further offshore and has a slightly deeper water column than does the first line. Again, shales are expected to be the main cause of anisotropy. A time-variant gain was applied to boost the amplitudes at large times; a dip filter and a mute were applied on CMP gathers to remove the groundroll and some near surface low-velocity dipping events; the data were also bandpass-filtered between 5 and 35 hz.

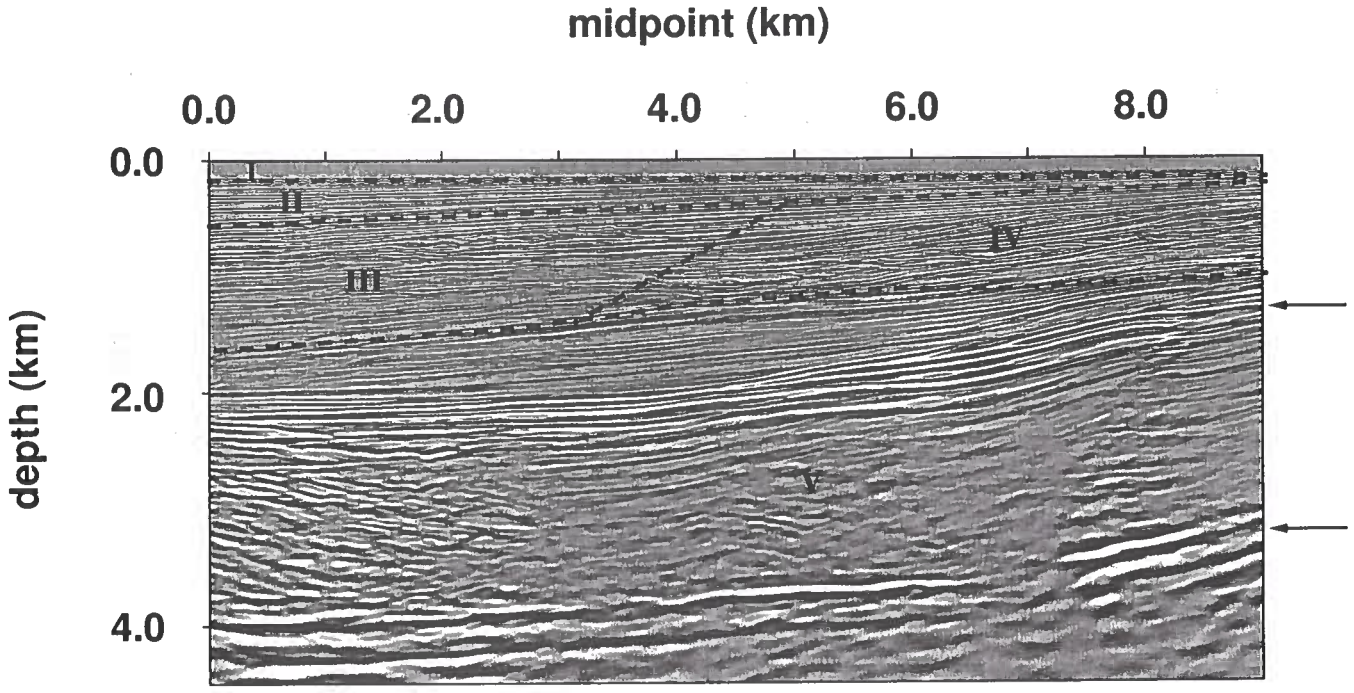

Figure 6.7. Stacked section after prestack depth migration with the estimated parameters for all five blocks. The arrows mark the reflectors used to estimate the parameters of the fifth block. The first reflector is the bottom of the subsidence unit and the second reflector is the bottom of the postrift unit. Note that the block boundaries of the velocity field do not follow these geological markers.

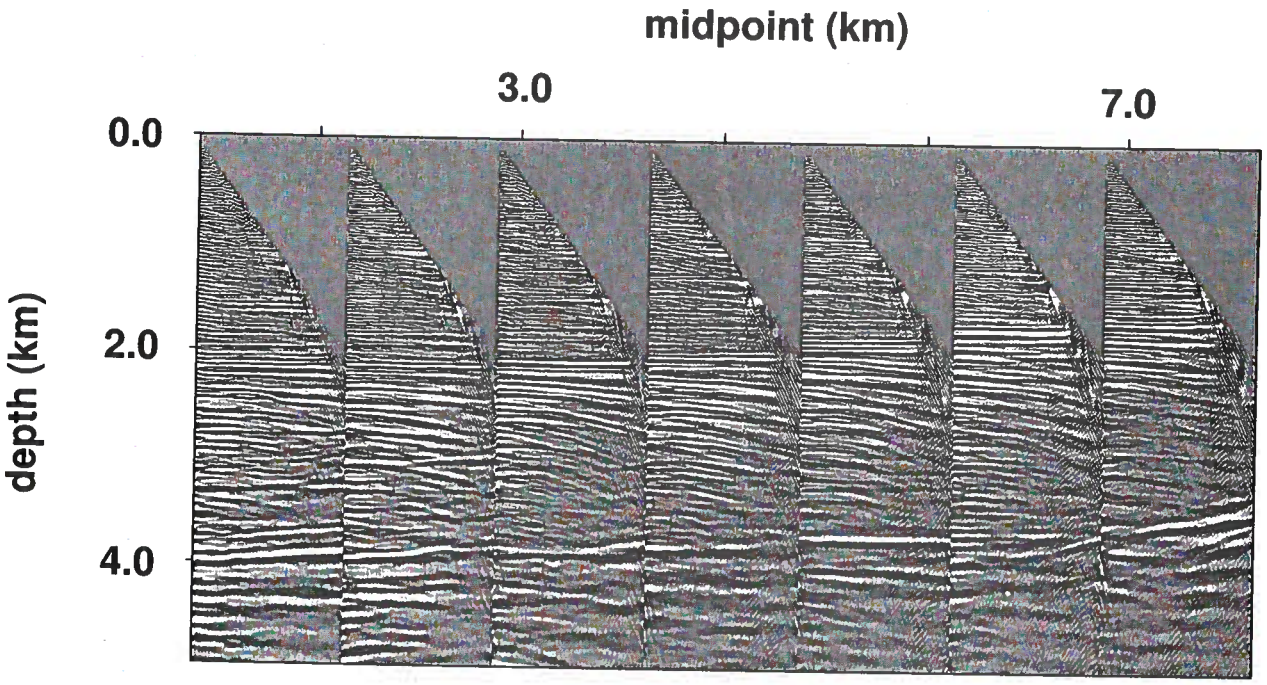

Figure 6.8. Common-image gathers after prestack depth migration with the estimated parameters. Most of the undercorrected events stack at extremely low velocity, and possibly are interbed multiples.

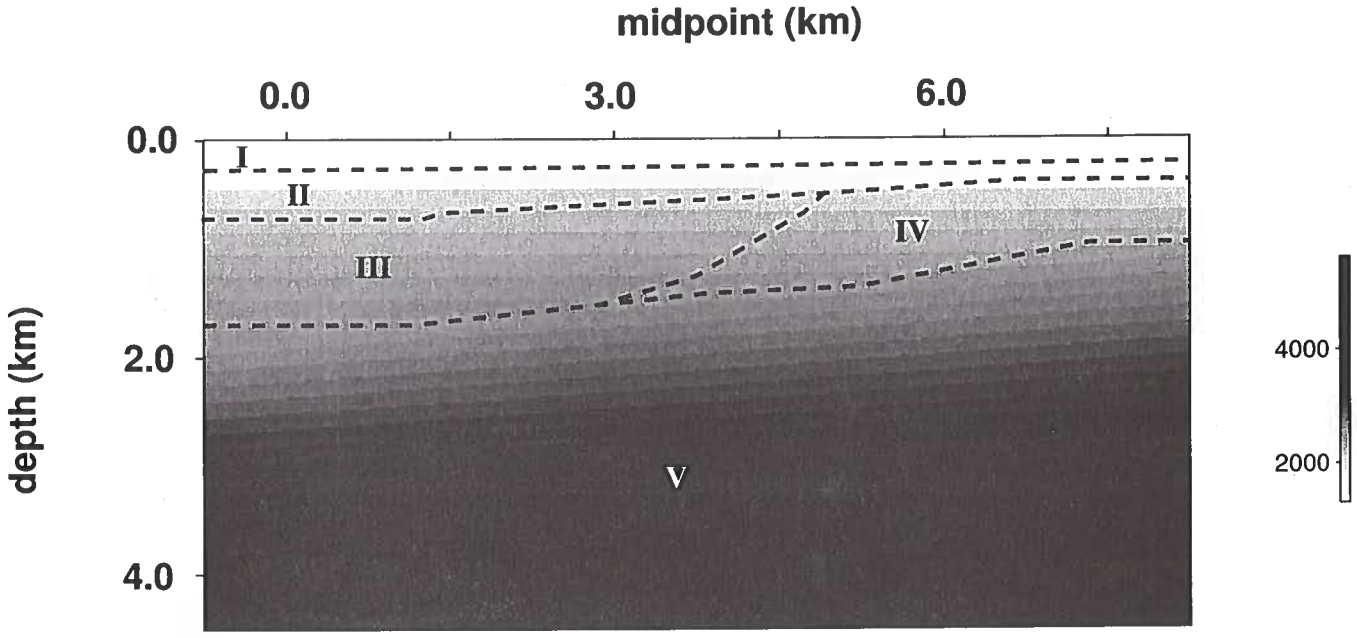

Figure 6.9. Depth section showing the estimated vertical velocity field. The dashed lines mark the block boundaries. The values in the legend are in m/s.

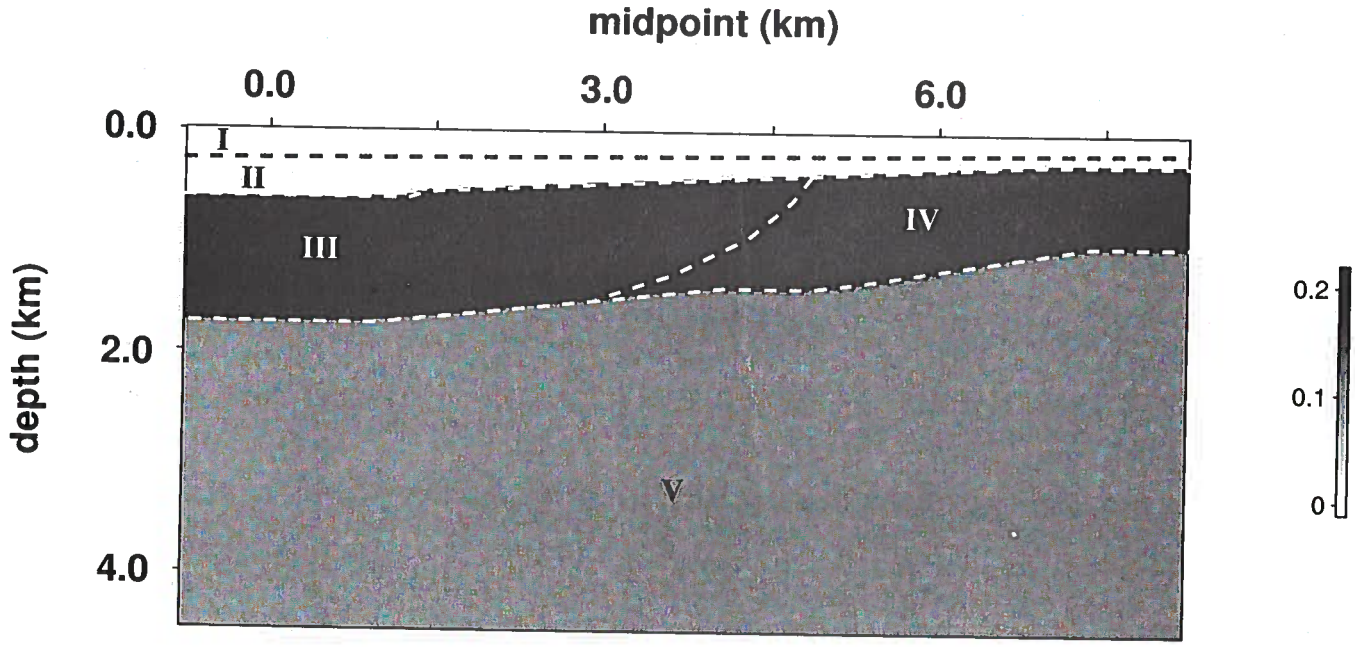

Figure 6.10. Depth section showing the estimated anellipticity parameter η.

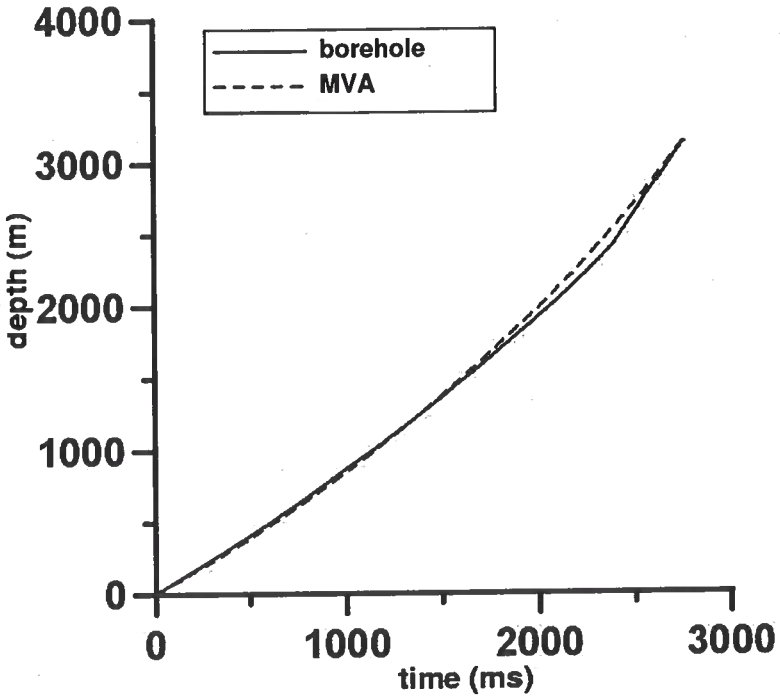

Figure 6.11. Comparison of the estimated time-depth curve at midpoint 5 km (dashed) with one derived from sonic logs and check shot data (courtesy of ChevronTexaco) in a borehole close to the line (solid).

Figure 6.12a shows the final prestack depth-migrated section with the estimated parameters, and Figure 6.12b shows the factorized VTI blocks that comprised the model. The estimated V_{P0}, ϵ, δ, and the anellipticity parameter η are shown in Figures 6.13-6.16. The parameters were estimated using the same procedure as that described for the first line. For blocks II, III, IV, and V, the migration velocity analysis was done after fixing the vertical velocity at the top of each block. I assumed that the vertical velocity was continuous between blocks I and II, I and V, II and III, and II and IV. Since blocks I, II, III, and V have negligible lateral variation, the choice of this point of continuity was not important. For the fourth block, however, significant lateral velocity variation exists. Therefore, I first did a homogeneous isotropic migration with the velocity equal to that of the bottom of the second block and examined the residual moveout on the resulting depth-migrated gathers shown in Figure 6.17. As the lateral position increases from 0 to 5 km, the moveout changes from being overcorrected to being undercorrected. Since the minimum residual moveout was observed at approximately 2.5 km, I chose this lateral position at the bottom of the second block as the point of continuity between the second and the fourth blocks. Fixing the value of the vertical velocity at this point I did migration velocity analysis to estimate the parameters. A large part of the fourth block has maximum offset-to-depth ratio less than two. Since this is less than optimal for the estimation of η, from horizontal events, I also used reflections from the prominent fault plane (dip$\approx 35°$) at the bottom of this block for the analysis. Reflections from this dipping fault plane were also used for the parameter estimation in the third block.

Anisotropy was not accounted for in block VI because the average maximum offset-to-depth ratio (≈ 1) in this block is not sufficient to constrain the parameter η. Therefore, I only estimated the isotropic parameters V_{P0}, defined at a point in the block, and the lateral and vertical gradients, k_x and k_z. In general, the moveout of a single event is sufficient to estimate these parameters, but here, in the absence of nonhyperbolic moveout, I used the hyperbolic portion of the moveout curve for two reflectors separated in depth.

The image gathers in Figure 6.18 show that the estimated parameters flatten the majority of the events in the entire section and confirm that the piecewise factorized VTI medium is a good approximation for the true velocity field in the area. The remaining residual moveout present for a few events is likely caused by multiples and high-wavenumber velocity variations, possibly at a scale much smaller than the spread of a typical CMP.

Block I is water, while blocks II, III, IV, V, and the portion of block VI above the first prominent reflector make up the subsidence unit. Sediments below this reflector are part of the postrift unit. Blocks IV and VI exhibit significant lateral velocity variation (in Block IV, $k_x = -0.07$ s^{-1} and in Block VI, $k_x = 0.16$ s^{-1}), which results in a decrease in V_{P0} towards the middle of the section. A low-velocity zone is close to the major fault plane that runs right through the middle of the section, and may point to a zone of weakness that often accompanies major faulting.

Also note that for this line the estimated anisotropy is less than that estimated for the first line (here $\eta_{\max} \approx 0.12 \pm 0.04$, in comparison to $\eta_{\max} \approx 0.21 \pm 0.03$ for the first line). One possible reason for the smaller values of η is that the shales in this area are less consolidated. When shales are not consolidated, the clay platelets, which are the main

source of anisotropy are not well aligned. This usually results in smaller estimates for η. Another possible reason could be attributed to the presence of overpressure, which is well documented in this area (Brice *et al.*, 1982; Alkhalifah, 1996). Decreasing the deviatoric stress reduces the value of the anellipticity parameter η (Sarkar *et al.*, 2003). Overpressure, which may cause a reduction in the deviatoric stress, could, therefore, also be one of the plausible causes for the lower anisotropy values recorded here. The depth section of η suggests that the shales are confined to only the third, fourth and fifth blocks, where η is significant. However, geological information in this area indicates that shales extend all the way to the bottom of the subsidence unit. To detect its presence precisely at greater depths from seismic measurements, however, it is necessary to have larger offsets or dipping events.

Figures 6.19a and b were used by Alkhalifah (1996) to illustrate the improvements in imaging after taking anisotropy into account. By including anisotropy, Alkhalifah (1996) was able to image the fault plane at midpoint 7.5 km and depth 3 km (Figure 6.19)b, which is absent on the isotropic image (Figure 6.19)a. The major fault plane that runs right through the section between midpoints 2 and 8 km and subhorizontal reflectors at midpoint 3 km and depth 2.7 km also show improved continuity on the anisotropic section. A comparison of the prestack depth-migrated image computed in Figure 6.20b and the time-migrated image in Figure 6.20a illustrates further improvements achieved by the MVA and prestack depth migration. Improvements are observed for the subhorizontal reflectors at midpoint 4.5 km and depth 1.4 km, the fault plane reflection at midpoint 7.5 km and depth 3 km, the subhorizontal reflectors in the subsidence unit just above this fault plane, the major fault-plane reflection extending between midpoints 2 and 8 km, and the reflectors just above and below this fault plane. Perhaps the most dramatic difference between the two images is in the shape and position of the two prominent reflectors that define the top and bottom of the postrift unit and span the entire lateral extent of the section between depths 2.5 and 5 kms. Because time migration does not account for the lateral variation in the vertical velocity, these two reflectors appear dipping on the time-migrated image. This dip was largely removed in Figure 6.20b by taking into account the significant lateral velocity variation in block VI. Also, since time migration ignores the lateral velocity variation in block IV, the antithetic faults, which are so clearly visible at midpoint 4 km and depth 2 km on the depth-migrated section, appear fuzzy in Figure 6.20a.

For this line my estimates of the maximum value of η ($\eta \approx 0.12$) is smaller than what was reported by Alkhalifah (1996) ($\eta \approx 0.2$). One likely reason for this difference is the presence of significant lateral heterogeneity, which was not taken into account in the DMO based methods followed in Alkhalifah (1996). Since I used MVA to estimate the parameters, I was able to describe the velocity variation with greater resolution and accuracy. The improved estimates give a clearer picture of the line, as is evident in Figure 6.20b.

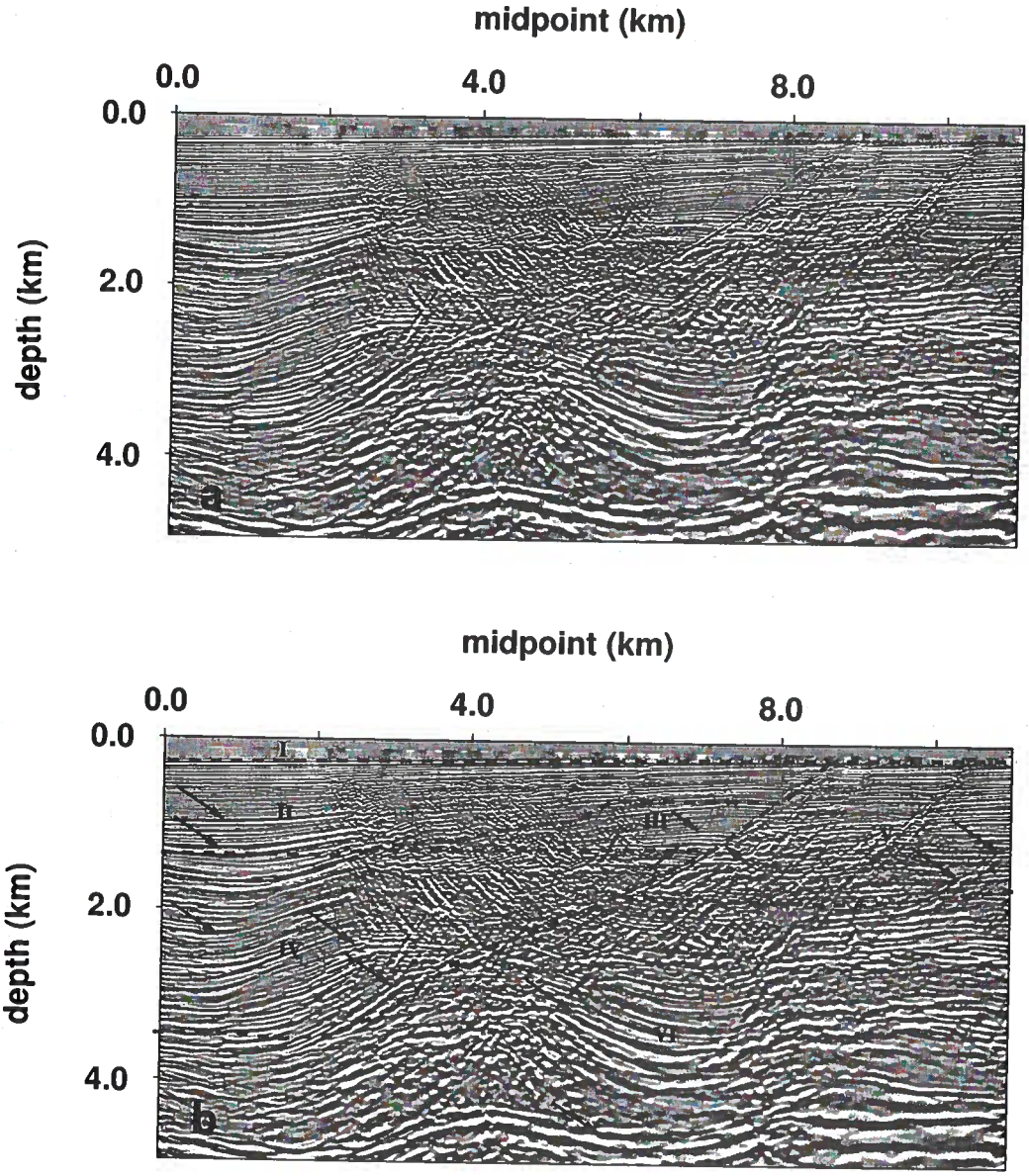

Figure 6.12. (a) Stacked section after prestack depth migration using the estimated parameters. (b) Same section with the blocks used in the velocity analysis marked by dashed lines. The arrows mark the reflectors used in the MVA. Block I is water with $V_{P0} = 1500$ m/s; the parameters estimated for block II are $V_{P0}(x = 4\,\text{km}, z = 240\,\text{m}) = 1500$ m/s, $k_z = 0.66 \pm 0.03$ s^{-1}, $k_x = 0.02 \pm 0.01$ s^{-1}, $\epsilon = 0.02 \pm 0.02$, and $\delta = -0.02 \pm 0.02$; for block III, $V_{P0}(x = 6.0\,\text{km}, z = 650\,\text{m}) = 1890$ m/s, $k_z = 0.4 \pm 0.04$ s^{-1}, $k_x = 0.01 \pm 0.01$ s^{-1}, $\epsilon = 0.12 \pm 0.03$, and $\delta = 0.03 \pm 0.03$; for block IV, $V_{P0}(x = 2.5\,\text{km}, z = 1400\,\text{m}) = 2200$ m/s, $k_z = 0.4 \pm 0.04$ s^{-1}, $k_x = -0.07 \pm 0.02$ s^{-1}, $\epsilon = 0.19 \pm 0.03$, and $\delta = 0.07 \pm 0.03$; for block V, $V_{P0}(x = 8.5\,\text{km}, z = 250\,\text{m}) = 1500$ m/s, $k_z = 0.65 \pm 0.03$ s^{-1}, $k_x = 0.03 \pm 0.02$ s^{-1}, $\epsilon = 0.15 \pm 0.02$, and $\delta = 0.06 \pm 0.02$; and for block VI, $V_{P0}(x = 6.5\,\text{km}, z = 1950\,\text{m}) = 2500$ m/s, $k_z = 0.65 \pm 0.03$ s^{-1}, $k_x = 0.16 \pm 0.02$ s^{-1}, $\epsilon = 0.0$, and $\delta = 0.0$.

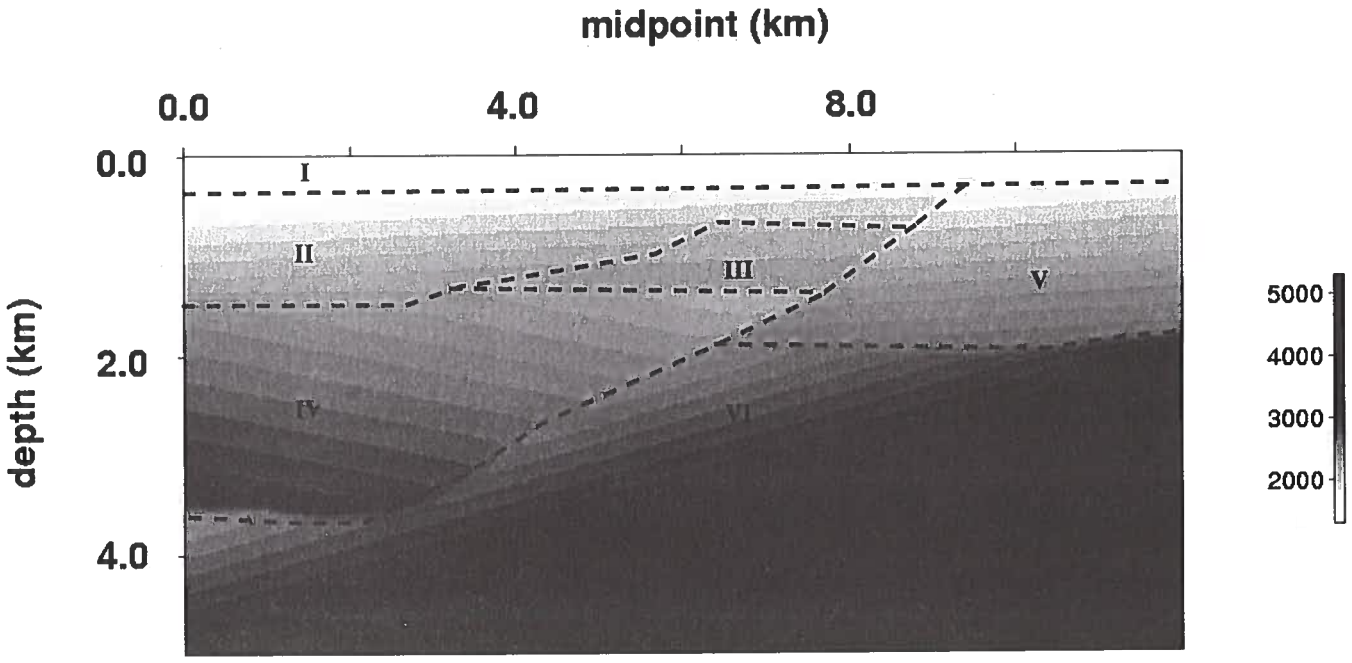

Figure 6.13. Depth section of the estimated vertical-velocity field.

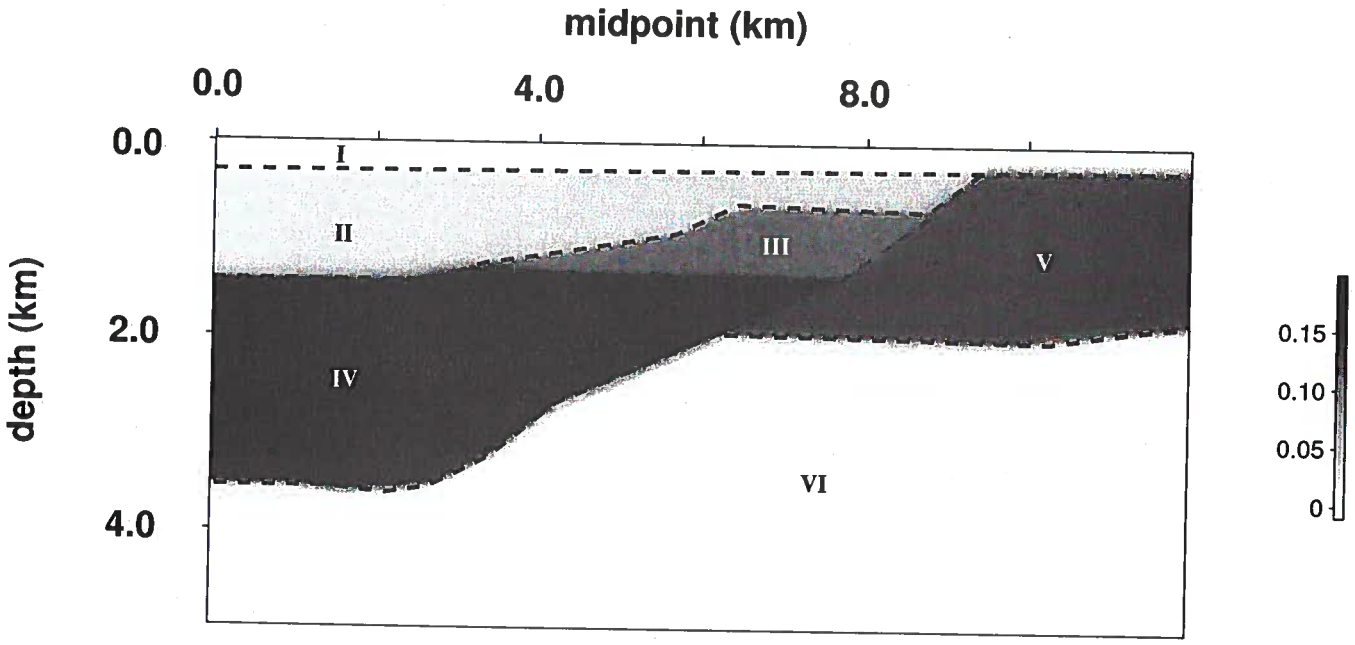

Figure 6.14. Depth section of the estimated parameter ϵ.

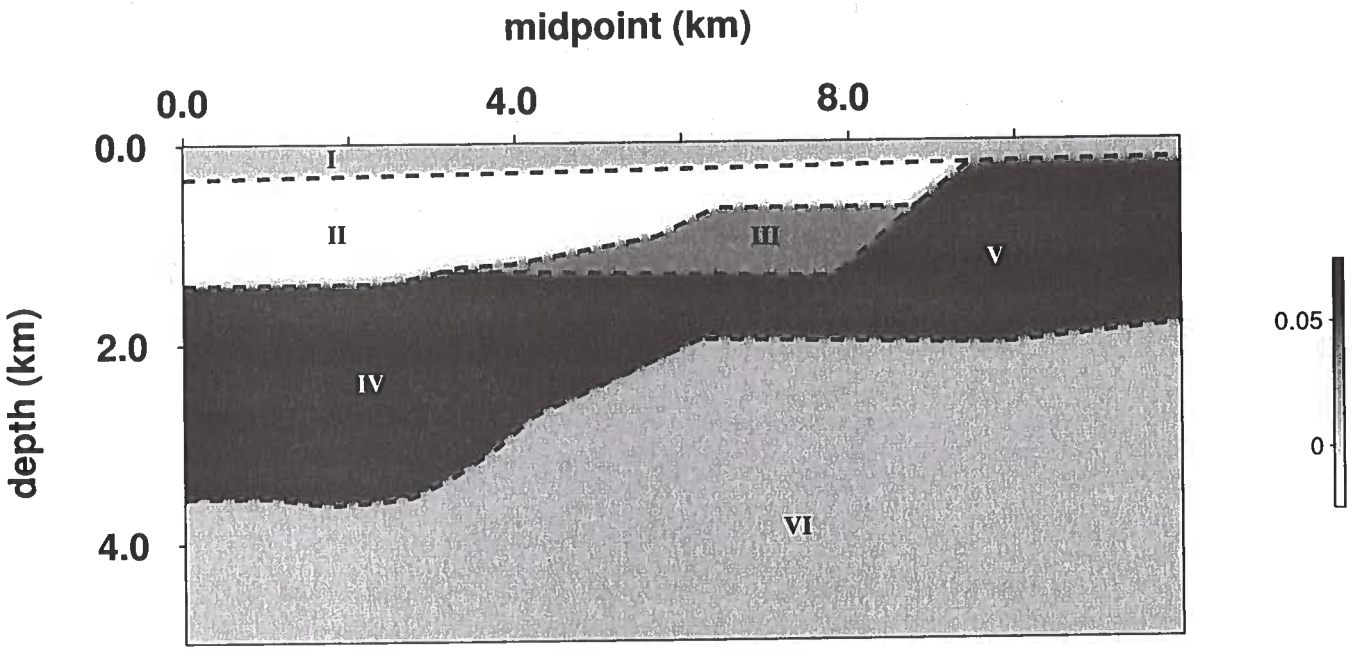

Figure 6.15. Depth section of the estimated parameter δ.

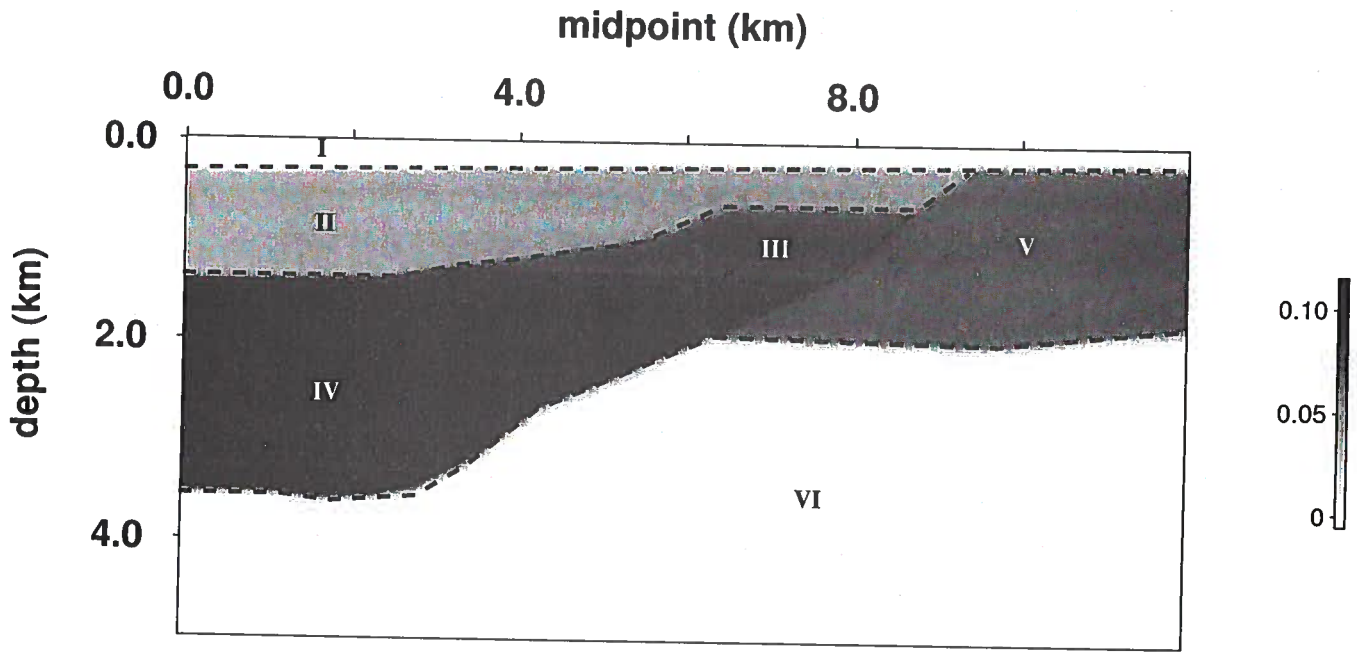

Figure 6.16. Depth section of the estimated parameter η.

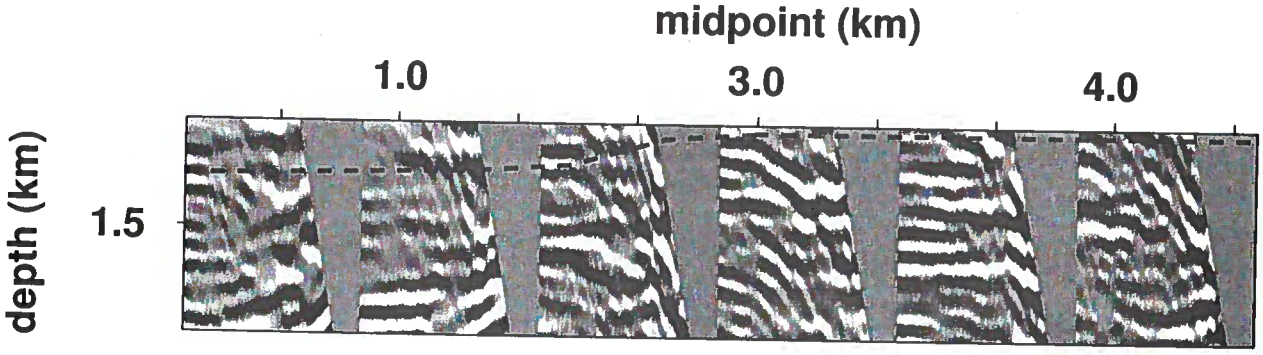

Figure 6.17. Common-image gathers after migration using a homogeneous isotropic model with the velocity equal to that at the bottom of the second block, shown here between depths 1300 m and 1700 m. The residual moveout of most events is overcorrected on the left and undercorrected on the right. The minimum residual moveout is observed between 2 and 3 km. The dashed line marks the bottom of the second block.

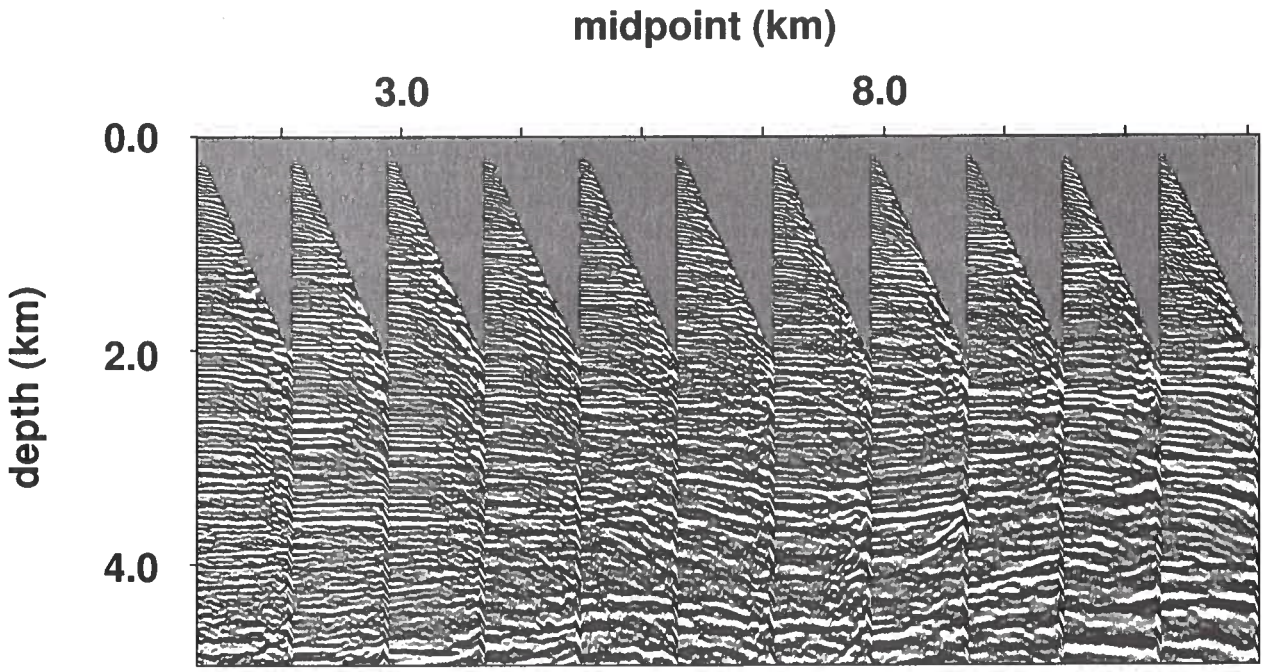

Figure 6.18. Common-image gathers at 1 km spacing, after migration with the estimated parameters.

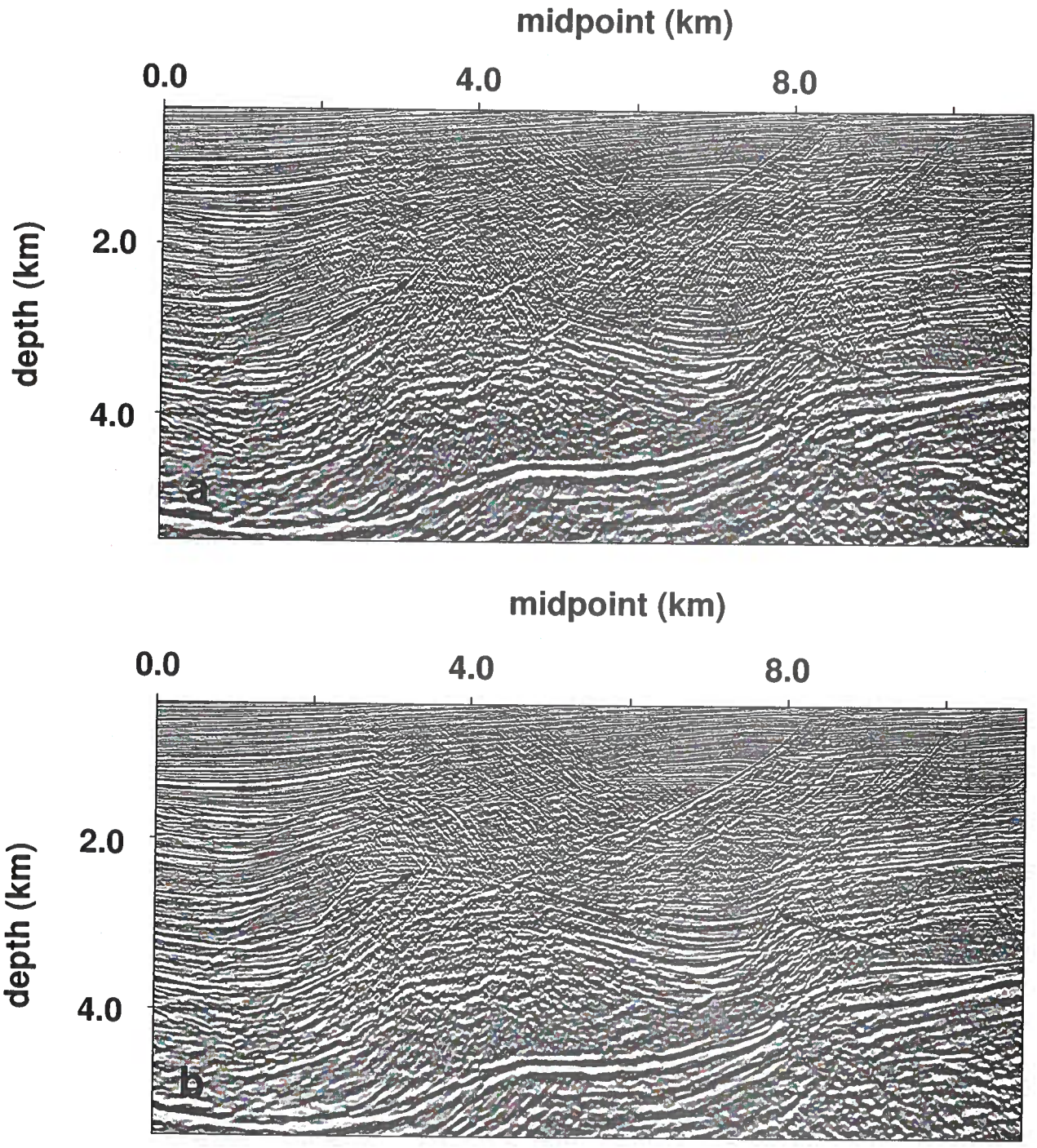

Figure 6.19. Second line after (a) isotropic and (b) anisotropic phase-shift time migration (after Alkhalifah, 1996). Figures (a) and (b) have been filtered to match the frequency spectrum of the depth-migrated section shown in Figure 6.12 and also stretched to depth using the vertical-velocity function (Figure 6.13) evaluated at midpoint 6 km. Arrows point to few improvements that result after accounting for anisotropy.

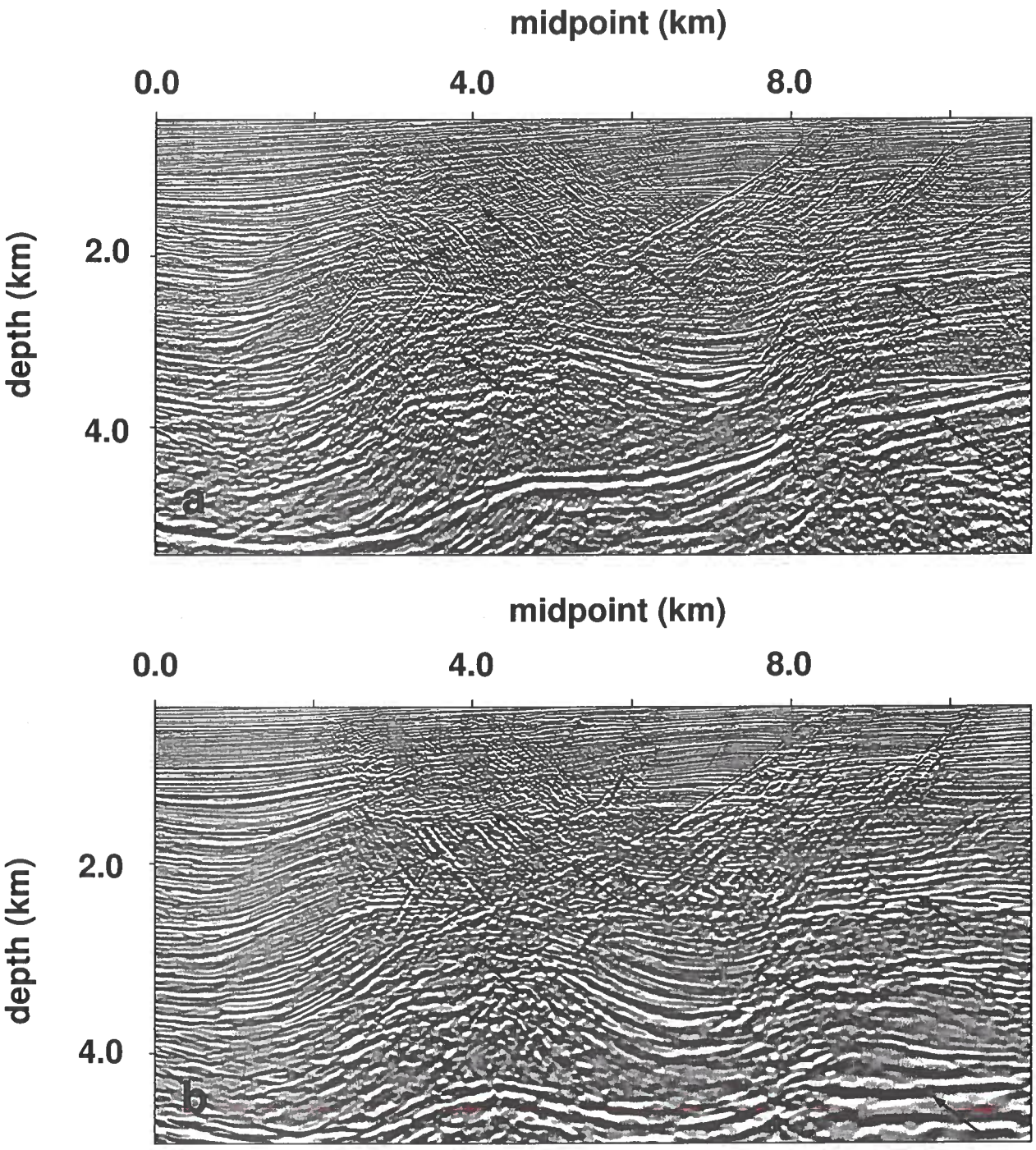

Figure 6.20. Second line after (a) anisotropic phase-shift time migration (after Alkhalifah, 1996) and (b) prestack depth migration. Arrows point to few improvements that result after migration velocity analysis and prestack depth migration.

Chapter 7

Conclusions and future work

7.1 Discussion

Approximating heterogeneous VTI models by factorized blocks or layers with linear velocity variation provides a convenient way to reconstruct vertically and laterally heterogeneous anisotropic velocity fields for P-wave prestack imaging. The migration velocity analysis (MVA) algorithm introduced here estimates the anisotropic parameters and velocity gradients in each subsurface block by minimizing the residual moveout of P-wave reflection events in image gathers. Tests on a specific field data set show that the piecewise factorized model can adequately describe velocity variations in the subsurface. The depth-domain MVA methodology reconstructed the velocity field with much greater resolution and accuracy than was previously possible using time-domain techniques.

In conventional seismic processing for isotropic media, image gathers have proved to be a convenient tool for refining velocity models as well as for a quick qualitative assessment of the accuracy of velocity analysis. If the medium is anisotropic, however, reflection moveout is governed by several anisotropic parameters, and the interpretation of image gathers becomes much more complicated. I presented an analytic and numerical study of P-wave common-image gathers in homogeneous and factorized $v(z)$ and $v(x,z)$ VTI media. Using the weak-anisotropy approximation, I obtained a simple representation of image gathers for horizontal events in homogeneous VTI media in terms of the vertical velocity V_{P0}, the NMO velocity $V_{\rm nmo}$ and the Alkhalifah-Tsvankin parameter η. Although this equation describes imaged depths, its structure is similar to that of the nonhyperbolic equation for P-wave reflection traveltimes (Alkhalifah and Tsvankin, 1995). The moveout on image gathers depends on the parameters $V_{\rm nmo}$ and η, with the NMO velocity responsible for the small-offset term and η governing the term quartic in offset. Therefore, although in principle the correct values of both $V_{\rm nmo}$ and η are needed to flatten an event, the influence of η becomes substantial only for offset-to-depth ratios exceeding unity.

In agreement with the general result of Alkhalifah and Tsvankin (1995), the same conditions (correct values of $V_{\rm nmo}$ and η) are needed to flatten dipping events in image gathers, but, in the presence of dip, η makes a substantial contribution to the near-offset moveout as well. The magnitude of residual moveout for a fixed error in $V_{\rm nmo}$ decreases with dip, while the residuals caused by an error in η reach their maximum value for intermediate dips (25°–35° in my examples). Even if migration is performed with the correct parameters $V_{\rm nmo}$ and η, and the events are flat and well-focused, the imaged depth differs from the true depth by a factor equal to the ratio of the migration and true vertical velocities; that is, by

a factor dependent on the unknown Thomsen parameter δ.

For factorized $v(z)$ models with a constant vertical velocity gradient k_z, the equation for moveout of horizontal events in image gathers has the same form as that in homogeneous media, but the effective vertical and NMO velocities are now ofcourse influenced by the vertical velocity gradient. Flattening events with any dip in $v(z)$ media requires the correct values of the NMO velocity at the surface, the coefficient η, and the gradient k_z. The influence of errors in k_z on the residual moveout decreases with dip (as is the case for errors in $V_{\rm nmo}$) but increases with reflector depth.

Extension of these results to laterally heterogeneous $v(x,z)$ models is based on the NMO equation of Grechka and Tsvankin (1999), which includes a correction term dependent on the lateral variation of the vertical velocity (or vertical traveltime). For a weak linear velocity dependence on x, the correction term vanishes, and the NMO velocity is equal to the corresponding value in the laterally homogeneous background. To equalize the background NMO velocities for all x, migration should be done with the correct value of the parameter combination $k_x\sqrt{1+2\delta}$ (k_x is the horizontal velocity gradient). Therefore, moveout on image gathers in $v(x,z)$ media is controlled by four parameter combinations: $V_{\rm nmo}(x=z=0)=V_{P0}\sqrt{1+2\delta}$, η, k_z, and $k_x\sqrt{1+2\delta}$. A positive error in any of these quantities causes undercorrection (i.e., the imaged depth increases with offset) and a negative error causes overcorrection. Although these parameters were derived assuming weak lateral heterogeneity, they are valid for any strength of anisotropy and heterogeneity.

Hence, the vertical velocity gradient k_z is constrained by P-wave image gathers not only in the $v(z)$ model, but also in laterally heterogeneous media. As a result, although the inversion of P-wave data for the vertical velocity and Thomsen coefficients will suffer from inherent ambiguities, minimal *a priori* assumptions may be sufficient to remove the trade-offs among the VTI parameters. For example, if the vertical velocity V_{P0} is known at any single surface location, then the estimated gradient k_z can be used to reconstruct the function $V_{P0}(z)$ and find the depth scale of the model. Also, in this case, the anisotropic parameter δ can be estimated from the NMO velocity at the surface ($V_{P0}\sqrt{1+2\delta}$), and, in turn, used to estimate the horizontal gradient k_x and the parameter ϵ.

If the medium is isotropic and sufficiently large offsets are available, the parameters V_{P0}, k_z, and k_x can be estimated using the residual moveout from a single reflector (Liu, 1997). In the presence of anisotropy, however, the residual moveout from a single reflector constrains only the effective quantities $v_{\rm nmo}$ and $\hat{\eta}$, even if large offsets are available. To estimate $V_{\rm nmo}$, k_z, k_x, and η, two reflectors separated in depth are required. Note that in the absence of nonhyperbolic moveout, two reflectors are also required to estimate k_z in isotropic media. Since conventional isotropic processing focuses on only the hyperbolic portion of the moveout curve and ignores nonhyperbolic moveout, the requirement of using two reflectors in anisotropic media is not much different from the requirements of isotropic velocity analysis.

Application of this MVA method confirms the conclusion that stable recovery of the parameters $V_{\rm nmo}$, k_z, $\hat{k}_x$, and η requires reflection moveout from at least two interfaces within each block sufficiently separated in depth. Numerical tests indicate that the velocity-analysis algorithm yields robust estimates of the four parameters if the vertical distance between the

two interfaces exceeds 1/4 of the depth of the bottom reflector. The precision in the estimate of k_x increases with the lateral spread of midpoint locations used in MVA. Another essential condition, for the stable estimation of the parameter η, is either the presence of dipping interfaces (dips should exceed 25°) or acquisition of long-spread data from subhorizontal reflectors providing maximum offset-to-depth ratios of at least two.

The residual moveout on image gathers for large offset-to-depth ratios was described by a nonhyperbolic function that depends on two independent moveout parameters. Although these parameters are not directly used in the velocity analysis, their best-fit values found from semblance search give an accurate approximation for the residual moveout. When the standard semblance operator fails, as may happen in the presence of polarity reversals occurring in Class II sands, modified semblance routines suggested by Sarkar *et al.* (2001, 2002) may be used instead.

The MVA is implemented in an iterative fashion, with the variance in the residual moveout minimized at each iteration step. At each step I solve a set of linear equations to estimate the updates in the medium parameters. With the updated parameters I perform prestack depth migration and obtain an image that is better focused than what was obtained in the previous iteration. I stop the algorithm when image gathers are flat. Since the parameter estimation is done in the post-migrated domain, the algorithm is robust in the presence of random noise and does not lose accuracy for models with significant lateral heterogeneity and dipping structures. Because V_{P0} is unconstrained by reflection P-wave data, I have to assume that the vertical velocity is known in each factorized block before estimating k_x, k_z, ϵ, and δ. If the factorized layer is too thin, the inversion can become unstable. The inversion may be stabilized by estimating k_z from NMO velocities using equation (3.6) and keeping this value fixed while estimating ϵ, δ, and k_x from MVA.

Vertical velocity information, which is required to constrain the inversion, can often be obtained from borehole data using either check shots or sonic logs. If no borehole information is available, a suitable model for depth imaging can sometimes be constructed by assuming that V_{P0} is continuous across block boundaries. Then, the entire velocity model in depth can be estimated from the residual moveout of P-wave reflection events. The examples presented in the thesis demonstrate that the assumption of continuity of V_{P0} offers a practical way to build reasonably accurate anisotropic velocity models. As the level of structural complexity increases, however, the true velocity field may have large velocity jumps across different blocks, and the adopted continuous velocity field will result in errors in the final image.

For relatively simple models with subhorizontal interfaces, the distortions related to an error in the vertical velocity are limited to a depth stretch that can vary from one layer to another. The moveout of events in image gathers is not influenced by an incorrect choice of V_{P0}, and the migrated image remains well focused as long as the algorithm yields accurate values of $V_{\rm nmo}$, k_z, $\hat{k}_x$, and η. In the presence of dipping interfaces, an overstated value of V_{P0} causes the imaged dips to be larger than the true ones; if V_{P0} is understated, the imaged dips are too small. In multilayered media, a depth stretch for dipping interfaces in the overburden can distort the shape of the underlying reflectors, even if the parameters immediately above these reflectors are estimated correctly.

In the presence of significant dip or curvature, P-wave reflection moveout and, therefore, residual moveout on image gathers become dependent on the vertical velocity and the parameters ϵ and δ (Le Stunff *et al.*, 2001; Grechka *et al.*, 2002). Then errors in V_{P0} in the overburden will not only cause errors in parameter estimation at the target, but will also result in poor imaging of target reflectors. For models of this type, the layer-stripping approach adopted in my MVA algorithm is not always adequate. Instead a simultaneous multilayer parameter estimation technique is necessary to constrain the parameters accurately.

Application of the MVA analysis approach to two field lines from West Africa confirms previous results that the subsurface is strongly anisotropic ($\eta_{\max} \approx 0.2$). The estimated velocity field also indicates the presence of significant lateral heterogeneity, which was previously unaccounted for by time-domain techniques (Alkhalifah, 1996). After MVA and prestack depth migration, the faults showed greater continuity, antithetic faults that were fuzzy in the time-migrated images were well focused and distinctly visible, geological features close to the major faults were well focused, subhorizontal reflectors in the anisotropic regions were better delineated, and many of the deeper reflectors were better positioned in depth. In particular, false dips seen on the time-migrated image were removed after MVA and prestack depth migration.

By approximating the subsurface with piecewise factorized $v(x, z)$ media, I was able to account for the vertical and lateral variation in the anisotropic parameters with much greater resolution than that achieved by time-domain methods. Flat image gathers after migration suggest that the factorized $v(x, z)$ medium is a good model for approximating realistic subsurface velocity variation. The successful implementation of my method on field data shows that the assumption of a continuous vertical velocity field can offer a reasonable way to build heterogeneous anisotropic velocity fields in depth that is suitable for prestack depth migration with minimal *a priori* information. The time-depth curve obtained from the MVA algorithm matches closely the curve computed from borehole data.

As in any other MVA technique, the main cost of my method is in the migration step, which makes this algorithm substantially more expensive than time-domain parameter estimation methods proposed in Alkhalifah (1996) and Grechka *et al.* (2002). Also, anisotropic migration is more expensive than isotropic migration because of the extra cost involved in computing reflection traveltimes. This extra cost is, however, negligible in comparison to the cost incurred in the actual migration step, which is the same for both isotropic and anisotropic media. In general, because of the larger number of parameters required to characterize anisotropic media, anisotropic parameter estimation requires a longer iteration process for convergence. This results in a greater number of migration and velocity analysis steps, which makes the anisotropic MVA more expensive than isotropic migration velocity analysis.

7.2 Conclusions

(1) I have developed a method suitable for velocity model building and imaging of P-wave data in heterogeneous VTI media.

(2) To develop such a process with minimal trade-offs between the estimated parameters the subsurface was approximated with piecewise factorized VTI blocks or layers. In each factorized block, the anisotropic parameters are independent of the spatial position, while the vertical velocity varies linearly with depth and lateral position. This model is simple enough to allow analytic insight into the trade-offs in parameter estimation, and, at the same time, it adequately describes realistic subsurface velocity variations.

(3) Even in the presence of lateral velocity variation, the vertical gradient in the vertical velocity V_{P0} can be uniquely estimated from surface seismic data without *a priori* information. The lateral gradient is, however, coupled to the anisotropy and cannot be resolved without knowledge of the Thomsen parameter δ.

(4) The velocity-analysis algorithm is implemented in the post-migrated domain. Thus, it is robust in the presence of uncorrelated random noise and is suitable for media that have significant lateral velocity variation.

(5) In general, knowledge of the vertical velocity is required at a point in each factorized layer or block to obtain the lateral gradient and anisotropic parameters. However, an anisotropic velocity field for imaging purposes may be constructed by assuming the vertical velocity to be continuous across layer boundaries. Then, minimal *a priori* information, such as knowledge of the vertical velocity at the surface, may be sufficient to constrain the velocity field.

(6) Application of this technique to field data from offshore West Africa suggests that the method may be suitable for velocity analysis and imaging when the subsurface is both heterogeneous and anisotropic.

7.3 Future work

7.3.1 3-D data

In this thesis I limited my study to 2-D data and introduced a method suitable for model building and imaging in the presence of heterogeneity (vertical and lateral) and vertical transverse isotropy. The ideas developed here can be readily extended to 3-D as well. In 3-D, the moveout of events will be governed by five parameters: $V_{\rm nmo}$, k_z, $\hat{k}_x$, $\hat{k}_y = k_y\sqrt{1+2\delta}$ (k_y is the lateral gradient along the $y-$axis and $\hat{k}_y$ is the effective lateral gradient in the same direction), and η, which can be estimated from the residual moveout of two events separated in depth and measured at three different midpoint locations containing two different azimuths. As in 2-D, knowledge of the vertical velocity at a single point in the medium will be required to estimate the medium parameters k_z, k_x, k_y, ϵ, and δ.

7.3.2 Multicomponent data

With the advent of ocean bottom cable (OBC), it is now possible to acquire converted (PS) modes offshore. Because one of the raypaths in PS reflection data is pure shear, PS data can improve imaging in areas where P-waves fail (e.g., beneath gas clouds). Moreover, since PS data are more sensitive to anisotropic parameters, they can be combined with P data to help improve anisotropic parameter estimation.

One of the main difficulties in extending the factorized model suggested in this thesis to PS data, however, is in accounting for the spatial variation in the vertical shear-wave velocity V_{S0}. The vertical gradient in V_{S0} was neglected in my study because V_{S0} does not substantially influence P-wave kinematics (Tsvankin, 2001). Strictly following the factorized model for PS data would imply that the gradients in V_{S0} are the same as the gradients in V_{P0}, which for all practical purposes is unrealistic because in the subsurface their gradients differ. Therefore, when working with PS data, a straightforward extension of my algorithm may not be possible. Certain modifications will need to be made in the model to account for the different spatial variations in V_{P0} and V_{S0}.

7.3.3 Tilted symmetry axis and media with lower symmetries

In some regions, such as the Canadian foothills, strong evidence suggests that the subsurface is transversely isotropic with a tilted symmetry axis. For such conditions, it is important to estimate not only the anisotropic parameters ϵ and δ, but also the tilt of the symmetry axis (ν). Indeed, the tilt can have a significant impact on the NMO velocity (Tsvankin, 2001). By dividing the subsurface into factorized TI blocks, where each block is characterized by constant values of ϵ, δ, ν, and a linearly varying V_{P0}, it may be possible to build velocity models for prestack depth imaging in heterogeneous TI media with a tilted symmetry axis.

The algorithm can also be extended to media with lower symmetries. For example, heterogeneous orthorhombic media are commonly encountered in fractured and stressed subsurface formations. Such media can be approximated with piecewise factorized $v(x,z)$ orthorhombic blocks, where in each factorized block the anisotropic parameters are constant while the vertical velocity V_{P0} varies linearly in the vertical and lateral directions. Since kinematics within each symmetry plane are the same as those in VTI media, my algorithm can be readily applied, and anisotropic parameters defined in the symmetry planes readily estimated. Away from the symmetry planes, however, the feasibility of the application of my algorithm will depend on how velocity gradients couple with the various anisotropic parameters, and requires further study.

7.3.4 Multilayer parameter estimation

In the presence of significant dips, an error in V_{P0} in the overburden may cause errors in the estimation of V_{nmo}, $\hat{k}_x$, k_z, and η of the target layer, and image gathers at target reflectors will not be flat. To correct for these errors, my method, which is based on layer stripping, requires the user to manually adjust the vertical velocity in the overburden to improve the image at the target. This may result in a cumbersome iterative procedure of correcting V_{P0} in the overburden and imaging at the target until the target is properly imaged. To avoid a manual iterative procedure such as this, simultaneous parameter estimation is required for multiple layers. Although I expect the multilayer update to be less well posed in comparison to the single-layer updates used here, it may provide a way to estimate the correct vertical velocity in the overburden with even less *a priori* information.

References

Alkhalifah, T. 1995a. Efficient synthetic seismogram generation in transversely isotropic, inhomogeneous media. *Geophysics*, **60**, 1139–1150.

Alkhalifah, T. 1995b. Gaussian beam depth migration for anisotropic media. *Geophysics*, **60**, 1474–1484.

Alkhalifah, T. 1996. *Velocity analysis for transversely isotropic media.* Ph.D. thesis, Colorado School of Mines, Golden, Colorado, USA.

Alkhalifah, T. 1997. Velocity analysis using nonhyperbolic moveout in transversely isotropic media. *Geophysics*, **62**, 1839–1854.

Alkhalifah, T. 2000. An acoustic wave equation for anisotropic media. *Geophysics*, **65**, 1239–1251.

Alkhalifah, T., and Tsvankin, I. 1995. Velocity analysis for transversely isotropic media. *Geophysics*, **60**, 1550–1566.

Alkhalifah, T., Tsvankin, I., Larner, K., and Toldi, J. 1996. Velocity analysis and imaging in transversely isotropic media: Methodology and a case study. *The Leading Edge*, May, 371–378.

Backus, G. E. 1970. Long-wave elastic anisotropy caused by horizontal layering. *J. Geophys. Res.*, **67**, 4427–4440.

Banik, N. C. 1984. Velocity anisotropy of shales and depth estimation in the North Sea basin. *Geophysics*, **49**, 1411–1419.

Birch, F. 1942. *Handbook of Physical Constants.* GSA Special Paper 36. Geological Society of America.

Birch, F. 1961. The velocity of compressional waves in rocks to 10 kilobars. *J. Geophys. Res.*, **66**, 2199–2223.

Brice, S. R., Cochran, M. D., Pardo, G., and Edwards, A. D. 1982. Tectonics and sedimentation of the South Atlantic rift sequence: Cabinda, Angola. *Pages 5–18 of: Studies in continental margin geology*, vol. 34. J. S. Watkins and C. L. Drake Eds., AAPG memoir.

Chauris, H., and Noble, M. 2001. Two-dimensional velocity macro model estimation from seismic reflection data by local differential semblance optimization: application to synthetic and real data sets. *Geophys. J. Int.*, **144**, 14–26.

Faust, L.Y. 1951. Seismic velocity as a function of depth and geologic time. *Geophysics*, **16**, 192–206.

Faust, L.Y. 1953. A velocity function including lithologic variation. *Geophysics*, **18**, 271–288.

Gajewski, D., and Pšenčík, I. 1987. Computation of high-frequency seismic wavefields in 3-D laterally inhomogeneous anisotropic media. *Geophys. J. R. Astr. Soc.*, **91**, 383–411.

Gardner, G. H. F., French, W. S., and Matzuk, T. 1974. Elements of migration and velocity analysis. *Geophysics*, **39**, 811–825.

Grechka, V., and Tsvankin, I. 1998a. 3-D description of normal moveout velocity for anisotropic inhomogeneous media. *Geophysics*, **63**, 1079–1092.

Grechka, V., and Tsvankin, I. 1998b. Feasibility of nonhyperbolic moveout inversion in transversely isotropic media. *Geophysics*, **63**, 957–969.

Grechka, V., and Tsvankin, I. 1999. 3-D moveout inversion in azimuthally anisotropic media with lateral velocity variation: Theory and a case study. *Geophysics*, **64**, 1202–1218.

Grechka, V., Pech, A., and Tsvankin, I. 2002. P-wave stacking-velocity tomography for VTI media. *Geophys. Prosp.*, **50**, 151–168.

Han, B., Galikeev, T., Grechka, V., Rousseau, J., and Tsvankin, I. 2000. A synthetic example of anisotropic P-wave processing for a model from the Gulf of Mexico. *In: Proceedings of the Ninth International Workshop on Seismic Anisotropy (9IWSA).* (Ikelle. L., and Gangi, A., Eds.), Soc. Expl. Geophys., Tulsa.

Helbig, K. 1984. Anisotropy and dispersion in periodically layered media. *Geophysics*, **49**, 364–373.

Jaramillo, H., and Larner, K. 1995. *Prestack migration error in transversely isotropic media.* In CWP Project Review.

Le Stunff, Y., and Jeannot, J.P. 1998. Pre-stack anisotropic depth imaging. *In: 60th EAGE conference, Extended Abstracts.*

Le Stunff, Y., Grechka, V., and Tsvankin, I. 2001. Depth-domain velocity analysis in VTI media using surface P-wave data: Is it feasible? *Geophysics*, **66**, 897–903.

Liu, Z. 1995. *Migration velocity analysis.* Ph.D. thesis, Colorado School of Mines, Dept. of Geophysics, Golden, Colorado, USA.

Liu, Z. 1997. An analytic approach to migration velocity analysis. *Geophysics*, **62**.

Meng, Z. 1999. *Tetrahedral based earth models, ray tracing in tetrahedral models and analytical migration velocity analysis.* Ph.D. thesis, Colorado School of Mines, Dept. of Geophysics, Golden, Colorado, USA.

Santosa, F., and Symes, W. W. 1989. An analysis of least-squares velocity inversion. *In: Geophysical monograph series.* (Raymon Brown Ed.), SEG, Tulsa.

Sarkar, D., Castagna, J. P., and Lamb, W. J. 2001. AVO and velocity analysis. *Geophysics*, **66**, 1284–1293.

Sarkar, D., Baumel, R. T., and Larner, K. L. 2002. Velocity analysis in the presence of amplitude variation. *Geophysics*, **67**, 1664–1672.

Sarkar, D., Bakulin, A., and Kranz, R. L. 2003. Anisotropic inversion of seismic data for stressed media: Theory and a physical modeling study on Berea Sandstone. *Geophysics*, **68**, 690–704.

Sayers, C. 1994. The elastic anisotropy of shales. *J. Geophys. Res.*, **99**, 767–774.

Stork, C. 1988. *Ray trace tomographic velocity analysis of surface seismic reflection data.* Ph.D. thesis, California Institute of Technology, Pasadena, California, USA.

Stork, C. 1992. Reflection tomography in the post migrated domain. *Geophysics*, **57**, 1290–1304.

Thomsen, L. 1986. Weak elastic anisotropy. *Geophysics*, **51**, 1954–1966.

Tsvankin, I. 2001. *Seismic signatures and analysis of reflection data in anisotropic media.* Elsevier Science.

Tsvankin, I., and Thomsen, L. 1994. Nonhyperbolic reflection moveout in anisotropic media. *Geophysics*, **59**, 1290–1304.

Červený, V. 1972. Seismic rays and ray intensities in inhomogeneous anisotropic media. *Geophys. J. R. Astr. Soc.,*, **29**, 1–13.

Červený, V. 1989. Ray tracing in factorized anisotropic inhomogeneous media. *Geophys. J. Int.*, **99**, 91–100.

Appendix A

Image gather for a horizontal reflector in a homogeneous VTI medium

Consider a horizontal reflector located at the depth z_T in a VTI medium with the vertical velocity $V_{P0,T}$ and Thomsen parameters ϵ_T and δ_T (Figure A.1). Suppose P-wave data acquired over such a model are migrated with the parameters $V_{P0,M}$, ϵ_M, and δ_M. Clearly, for a horizontal reflector the image point does not move laterally. Therefore, the reflection traveltimes in the true (t_T) and migration (t_M) models for the half-offset h can be written as

$$t_T = \frac{2\sqrt{h^2 + z_T^2}}{V_{g,T}(\phi)} \tag{A.1}$$

and

$$t_M = \frac{2\sqrt{h^2 + z_M^2}}{V_{g,M}(\phi')}, \tag{A.2}$$

where $V_{g,T}$ is the group velocity at the group angle ϕ in the true model, and $V_{g,M}$ is the group velocity at the group angle ϕ' in the model used for migration.

Under the assumption of weak anisotropy, quadratic and higher-order terms in the anisotropic coefficients can be neglected, and the group velocity can be replaced with the corresponding phase velocity (Thomsen, 1986; Tsvankin, 2001):

$$V_{g,T}(\phi) = V_{P0,T}\left[1 + \delta_T \sin^2\phi + (\epsilon_T - \delta_T)\sin^4\phi\right]. \tag{A.3}$$

Likewise, for the migration model

$$V_{g,M}(\phi') = V_{P0,M}\left[1 + \delta_M \sin^2\phi' + (\epsilon_M - \delta_M)\sin^4\phi'\right]. \tag{A.4}$$

Substituting equations (A.3) and (A.4) into equations (A.1) and (A.2), equating the true and migration traveltimes ($t_T = t_M$), and linearizing the resulting expression in the anisotropic coefficients yields

$$\gamma^2 (h^2 + z_T^2)\left[1 - 2\delta_T \sin^2\phi - 2(\epsilon_T - \delta_T)\sin^4\phi\right] = (h^2 + z_M^2)[1 - 2\delta_M \sin^2\phi - 2(\epsilon_M - \delta_M)\sin^4\phi'], \tag{A.5}$$

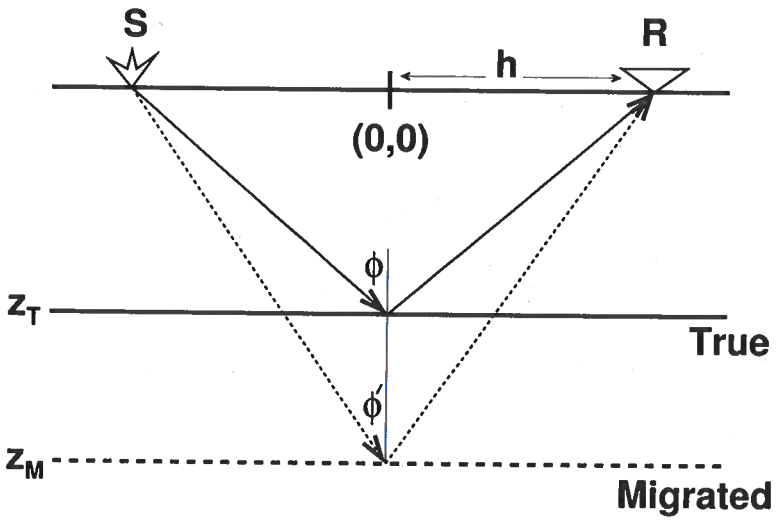

Figure A.1. True and migrated positions of a horizontal reflector.

where $\gamma \equiv V_{P0,M}/V_{P0,T}$.

Expressing

$$\sin^2\phi = \frac{h^2}{h^2+z_T^2} \quad \text{and} \quad \sin^2\phi' = \frac{h^2}{h^2+z_M^2} \tag{A.6}$$

in equation (A.5) and solving for z_M, I obtain

$$z_M^2 \approx \gamma^2 z_T^2 + h^2(2\delta_M - 1 + \gamma^2 - 2\delta_T\gamma^2) - \frac{2h^4\gamma^2(\epsilon_T-\delta_T)}{h^2+z_T^2} + \frac{2h^4(\epsilon_M-\delta_M)}{\gamma^2\,(h^2+z_T^2)}. \tag{A.7}$$

The coefficient of h^2 can be represented as

$$(2\delta_M - 1 + \gamma^2 - 2\delta_T\gamma^2) \approx V_{P0,M}^2\left(\frac{1}{V_{\text{nmo},T}^2} - \frac{1}{V_{\text{nmo},M}^2}\right), \tag{A.8}$$

where $V_{\text{nmo}} = V_{P0}\sqrt{1+2\delta} \approx V_{P0}\,(1+\delta)$. Similarly, the coefficient of $[2h^4/(h^2+z_T^2)]$ takes the form

$$\gamma^2(\epsilon_T-\delta_T) - \frac{(\epsilon_M-\delta_M)}{\gamma^2} \approx \left(\eta_T\frac{V_{\text{nmo},M}^2}{V_{\text{nmo},T}^2} - \eta_M\frac{V_{\text{nmo},T}^2}{V_{\text{nmo},M}^2}\right), \tag{A.9}$$

where $\eta \equiv (\epsilon-\delta)/(1+2\delta) \approx \epsilon-\delta$. Therefore, equation (A.7) can be rewritten in terms of V_{nmo} and η as

$$z_M^2 \approx \gamma^2 z_T^2 + h^2 V_{P0,M}^2\left(\frac{1}{V_{\text{nmo},T}^2} - \frac{1}{V_{\text{nmo},M}^2}\right) + \frac{2h^4}{h^2+z_T^2}\left(\eta_M\frac{V_{\text{nmo},T}^2}{V_{\text{nmo},M}^2} - \eta_T\frac{V_{\text{nmo},M}^2}{V_{\text{nmo},T}^2}\right). \tag{A.10}$$

Appendix B

Image gather in a factorized $v(z)$ medium

Here, I extend the results of Appendix A to factorized $v(z)$ VTI media defined by the vertical velocity $V_{P0,T}$ at zero depth, the vertical velocity gradient $k_{z,T}$, and Thomsen parameters ϵ_T and δ_T. The one-way zero-offset time τ for a horizontal reflector can be found as the following function of depth z:

$$\begin{aligned} \tau &= \int_0^z \frac{d\xi}{V(\xi)} \\ &= \int_0^z \frac{d\xi}{V_{P0,T} + k_{z,T}\,\xi} \\ &= \frac{1}{k_{z,T}} \ln\left[\frac{V_{P0,T} + k_{z,T}\,z}{V_{P0,T}}\right]. \end{aligned} \tag{B.1}$$

Expressing z as a function of τ yields

$$z = \frac{V_{P0,T}}{k_{z,T}} \left(e^{k_{z,T}\,\tau} - 1\right). \tag{B.2}$$

Substituting z into the equation $V_{P0,T}(z) = V_{P0,T} + k_{z,T}\,z$ allows one to represent the vertical velocity as a function of the zero-offset time:

$$V_{P0}(\tau) = V_{P0,T}\, e^{k_{z,T}\,\tau}. \tag{B.3}$$

Then the interval NMO velocity is given by

$$V_{\mathrm{nmo}}(\tau) = V_{P0,T}\,\sqrt{1+2\delta_T}\; e^{k_{z,T}\,\tau}. \tag{B.4}$$

Applying the Dix formula and substituting equation (B.4), I obtain the effective NMO velocity for a reflector at the depth z_T:

$$\begin{aligned} v^2_{\mathrm{nmo},T}(\tau_0) &= \frac{1}{\tau_0}\int_0^{\tau_0} V^2_{\mathrm{nmo}}(\tau)d\tau, \\ &= \frac{V^2_{P0,T}\,(1+2\delta_T)}{2\,\tau_0\,k_{z,T}} \left(e^{2k_{z,T}\,\tau_0} - 1\right), \text{ or} \\ v^2_{\mathrm{nmo},T}(t_0) &= \frac{V^2_{P0,T}\,(1+2\delta_T)}{t_0\,k_{z,T}} \left(e^{k_{z,T}\,t_0} - 1\right), \end{aligned} \tag{B.5}$$

where $t_0 = 2\tau_0$ is the two-way zero-offset time.

As shown in Alkhalifah (1997) and Appendix 4B of Tsvankin (2001), the zero-offset time t_0, the NMO velocity $v_{\rm nmo}$, and the parameter $\hat{\eta}$, which is defined as

$$\begin{aligned}\hat{\eta}_T &= \frac{1}{8}\left\{\frac{(1+8\eta_T)}{v^4_{{\rm nmo},T}(\tau_0)\,\tau_0}\left[\int_0^{\tau_0} V^4_{\rm nmo}(\tau)d\tau\right]-1\right\}\\ &= \frac{1}{8}\left\{\frac{(1+8\eta_T)(e^{2k_{z,T}\,t_0}-1)\,k_{z,T}\,t_0}{2(e^{k_{z,T}\,t_0}-1)^2}-1\right\},\end{aligned} \tag{B.6}$$

fully determine reflection moveout from horizontal interfaces in $v(z)$ VTI media. Hence, for the purpose of migrating horizontal events, the true factorized $v(z)$ medium can be replaced by a homogeneous VTI model with the vertical velocity equal to the average vertical velocity ($\hat{V}_{P0,T}$) above the reflector, the NMO velocity equal to $v_{{\rm nmo},T}$, and the parameter η equal to $\hat{\eta}_T$. Note that $\hat{\eta}_T$ depends on the zero-offset time t_0, and hence, on the depth z_T.

For a migrated image point at half-offset h, the same substitutions can be used to replace the factorized $v(z)$ migration model above the image point with an equivalent homogeneous model. Therefore, the linearized equation of an image gather for a factorized $v(z)$ medium can be adapted from equation (A.10) for homogeneous media:

$$\begin{aligned}z^2_M(h) &\approx \gamma^2 z_T^2 + h^2\,\hat{V}^2_{P0,M}[z_M(h)]\left\{\frac{1}{v^2_{{\rm nmo},T}(z_T)}-\frac{1}{v^2_{{\rm nmo},M}[z_M(h)]}\right\}\\ &+ \frac{2h^4}{h^2+z_T^2}\left\{\hat{\eta}_M[z_M(h)]\frac{v^2_{{\rm nmo},T}(z_T)}{v^2_{{\rm nmo},M}[z_M(h)]}-\hat{\eta}_T[z_T(h)]\frac{v^2_{{\rm nmo},M}[z_M(h)]}{v^2_{{\rm nmo},T}(z_T)}\right\},\end{aligned} \tag{B.7}$$

where $\gamma \equiv \hat{V}_{P0,M}[z_M(h)]/\hat{V}_{P0,T}[z_T(h)]$, $\hat{V}_{P0}$ is the average vertical velocity of the overburden, and the effective NMO velocities and η values are computed from equations (B.5) and (B.6).

When the migration model is close to the true model, the migrated depth is weakly dependent on offset (for a moderate offset range), and the effective quantities for the actual depth $z_M(h)$ can be replaced with those for $z_M(0)$. Then equation (B.7) can be rewritten as

$$\begin{aligned}z^2_M(h) &\approx \gamma^2 z_T^2 + h^2\,\hat{V}^2_{P0,M}\left\{\frac{1}{v^2_{{\rm nmo},T}(z_T)}-\frac{1}{v^2_{{\rm nmo},M}[z_M(0)]}\right\}\\ &+ \frac{2h^4}{h^2+z_T^2}\left\{\hat{\eta}_M[z_M(0)]\frac{v^2_{{\rm nmo},T}(z_T)}{v^2_{{\rm nmo},M}[z_M(0)]}-\hat{\eta}_T(z_T)\frac{v^2_{{\rm nmo},M}[z_M(0)]}{v^2_{{\rm nmo},T}(z_T)}\right\}.\end{aligned} \tag{B.8}$$

Note, however, that equation (B.8) does not involve the approximation for the effective quantities if the image gather is obtained after migration using a homogeneous VTI medium with the vertical velocity equal to $\hat{V}_{P0}[z(0)]$, NMO velocity equal to $v_{{\rm nmo},M}[z(0)]$, and η equal to $\hat{\eta}[z(0)]$.

Appendix C

Algorithm for velocity update

Following the approach suggested by Liu (1997), we design the velocity-updating algorithm to minimize the variance in the migrated depths of events in image gathers. To simplify a generally nonlinear inverse (minimization) problem, we perform the velocity analysis iteratively, with a set of linear equations being solved at each iteration. Below we discuss the velocity update performed at a single (l^{th}) step of the iterative process.

Suppose that prestack migration after the $(l-1)^{\text{th}}$ iteration of the velocity analysis resulted in the migrated depths $z_0(x_j, h_k)$ (x_j is the surface coordinate of the j^{th} image gather, and h_k is the half-offset). Then the migrated depths $z(x_j, h_k)$ after the l^{th} iteration can be represented as a linear perturbation of $z_0(x_j, h_k)$:

$$z(x_j, h_k) = z_0(x_j, h_k) + \Sigma_{i=1}^{N} \frac{\partial z_0(x_j, h_k)}{\partial \lambda_i} \Delta\lambda_i \,, \tag{C.1}$$

where $\partial z_0(x_j, h_k)/\partial\lambda_i$ are the derivatives of the migrated depths with respect to the medium parameters λ_i ($i = 1, 2, 3, \ldots N$), and $\Delta\lambda_i = \lambda_i' - \lambda_i$ are the desired parameter updates. The goal of the updating procedure is to estimate $\Delta\lambda_i$ and, therefore, find the parameters λ_i' to be used for the migration after the l^{th} iteration.

The variance V of the migrated depths for a single reflection event at all offsets and image gathers is

$$V = \Sigma_{j=1}^{P} \Sigma_{k=1}^{M} [z(x_j, h_k) - \hat{z}(x_j)]^2 \,, \tag{C.2}$$

where $\hat{z}(x_j) = (1/M)\, \Sigma_{k=1}^{M} z(x_j, h_k)$ is the average migrated depth of the event at surface coordinate x_j, P is the number of image gathers used in the velocity update, and M is the number of offsets in each image gather. The minimization at each iteration step is accomplished by searching for the parameter updates that satisfy the condition $\partial V/\partial(\Delta\lambda_r) = 0$ ($r = 1, 2, 3, \ldots N$). Subsituting equation (C.1) in equation (C.2), differentiating the variance with respect to the parameter updates, and setting $\partial V/\partial(\Delta\lambda_r) = 0$ yields

$$\begin{aligned} -\Sigma_{j=1}^{P}\Sigma_{k=1}^{M}\Sigma_{i=1}^{N}(g_{jk,i} - \hat{g}_{j,i})(g_{jk,r} - \hat{g}_{j,r})\Delta\lambda_i \\ = \Sigma_{j=1}^{P}\Sigma_{k=1}^{M}[z_0(x_j, h_k) - \hat{z}_0(x_j)](g_{jk,r} - \hat{g}_{j,r}) \,, \end{aligned} \tag{C.3}$$

where $g_{jk,r} \equiv \partial z_0(x_j, h_k)/\partial\lambda_r$, $g_{jk,i} \equiv \partial z_0(x_j, h_k)/\partial\lambda_i$, and $\hat{g}_{j,i} \equiv (1/M)\Sigma_{k=1}^{M} g_{jk,i}$; all derivatives are evaluated for the medium parameters λ_i.

Equation (C.3) can be rewritten in matrix form as

$$\boldsymbol{A}^{\boldsymbol{T}}\boldsymbol{A}\,\Delta\boldsymbol{\lambda} = \boldsymbol{A}^{\boldsymbol{T}}\boldsymbol{b}, \tag{C.4}$$

where $\boldsymbol{A}$ is a matrix with $M \cdot P$ rows and N columns whose elements are $g_{jk,r} - \hat{g}_{j,r}$, and $\boldsymbol{b}$ is a vector with $M \cdot P$ elements defined as $z_0(x_j, h_k) - \hat{z}_0(x_j)$. $\boldsymbol{A}^{\boldsymbol{T}}\boldsymbol{A}$ is a square $N \times N$ matrix, and the vector $\boldsymbol{A}^{\boldsymbol{T}}\boldsymbol{b}$ has N elements, so the problem has been reduced to a system of N linear equations with N unknowns $\Delta\boldsymbol{\lambda}$. We solve the system (C.4) using a linear conjugate gradient scheme to obtain $\Delta\boldsymbol{\lambda}$ and the updated parameters $\boldsymbol{\lambda}' = \Delta\boldsymbol{\lambda} + \boldsymbol{\lambda}$.

The derivatives of the depths $z(x_j, h_k)$ with respect to the medium parameters λ_i (and, therefore, the matrix $\boldsymbol{A}$) can be determined from the imaging equations (e.g., Liu, 1997):

$$\tau_s(y, h, x, z, \vec{\lambda}) + \tau_r(y, h, x, z, \vec{\lambda}) = t(y, h)\,, \tag{C.5}$$

$$\frac{\partial\tau_s(y, h, x, z, \vec{\lambda})}{\partial y} + \frac{\partial\tau_r(y, h, x, z, \vec{\lambda})}{\partial y} = \frac{\partial t(y, h)}{\partial y}\,. \tag{C.6}$$

Here y is the common-midpoint location at the surface, h is the half-offset, τ_s is the traveltime from the source location x_s ($x_s = y + h$) to the diffractor location (x, z) that was obtained after prestack depth migration with the medium parameters λ_i, τ_r is the traveltime from the receiver location x_r ($x_r = y - h$) to the point (x, z), and $t(y, h)$ is the observed reflection traveltime. Note that y, x, and z depend on the medium parameters λ_i, while h is an independent variable. Because x is fixed at the surface location where a particular image gather is analyzed, however, the derivative of x with respect to λ_i is set to zero.

Differentiating equation (C.5) with respect to λ_i gives

$$\left[\frac{\partial\tau_s}{\partial y} + \frac{\partial\tau_r}{\partial y}\right]\frac{dy}{d\lambda_i} + \left[\frac{\partial\tau_s}{\partial z} + \frac{\partial\tau_r}{\partial z}\right]\frac{dz}{d\lambda_i} + \left[\frac{\partial\tau_s}{\partial\lambda_i} + \frac{\partial\tau_r}{\partial\lambda_i}\right] = \frac{\partial t}{\partial y}\frac{dy}{d\lambda_i}\,. \tag{C.7}$$

Taking equation (C.6) into account simplifies equation (C.7) to

$$\left[\frac{\partial\tau_s}{\partial z} + \frac{\partial\tau_r}{\partial z}\right]\frac{dz}{d\lambda_i} = -\frac{\partial\tau_s}{\partial\lambda_i} - \frac{\partial\tau_r}{\partial\lambda_i}\,, \tag{C.8}$$

or

$$\frac{dz}{d\lambda_i} = -\left[\frac{\partial\tau_s}{\partial\lambda_i} + \frac{\partial\tau_r}{\partial\lambda_i}\right]\frac{1}{q_s + q_r}\,, \tag{C.9}$$

where $q_s = \partial\tau_s/\partial z$ and $q_r = \partial\tau_r/\partial z$ are the vertical slownesses evaluated at the diffractor for the specular rays connecting the diffractor with the source and the receiver, respectively.

To find the derivatives $dz/d\lambda_i$, we perform ray tracing using the prestack-migrated image after the $(l-1)^{\text{th}}$ iteration. First, the dip of the reflector needed to define the specular reflected rays is estimated by manual picking on the image. Then, for a given diffraction point on the reflector and a fixed source-receiver offset, the specular ray is traced through two models, one of which is defined by the parameters λ_i and the other by parameters slightly deviating from λ_i (i.e., λ_i are slightly perturbed). The corresponding perturbation

of the traveltime between the source and the diffractor is divided by the perturbation in λ_i to obtain $\partial\tau_s/\partial\lambda_i$, while the same quantity for the traveltime leg between the diffractor and the receiver gives $\partial\tau_r/\partial\lambda_i$. The slownesses q_r and q_s at the diffraction point are part of the output of the ray-tracing algorithm (Červený, 1972).